Mid crustal granulite facies metamorphism in the Reynolds Range, central Australia: physical conditions, duration and potential mechanisms

Elizabeth McBride

Supervisors: David Kelsey and Martin Hand

Honours student, Centre for Tectonics Resources and Exploration

Geology and Geophysics, School of Earth and Environmental Sciences,

The University of Adelaide, Adelaide, SA 5005, Australia

Table of Contents

Mid crustal granulite facies metamorphism in the Reynolds Range, central Australia: physical conditions, duration and potential mechanisms

Elizabeth McBride

Supervisors: David Kelsey and Martin Hand

Centre for Tectonics Resources and Exploration

Department of Geology and Geophysics

School of Earth and Environmental Sciences

The University of Adelaide, Adelaide, SA 5005, Australia

elizabeth.mcbride@student.adelaide.edu.au

ABSTRACT

The transient advection of heat due to magma ascent is often the governing paradigm for low-pressure, high-temperature (LPHT) metamorphism. However, the origins of metamorphism (~750 – 800 °C and 4 – 5 kbars) in the Reynolds Range region of the central Arunta Province, Arunta Inlier, central Australia, remain contentious for two reasons: (1) The causative mechanism for high geothermal gradient metamorphism is not well understood; and (2) elevated temperatures appear to be sustained for a prolonged period, ~30 Myr. In situ LA-ICPMS monazite U-Pb geochronology coupled with metamorphic phase equilibria modelling provide evidence for regional-scale high-temperature metamorphism in the Arunta Inlier during the early Mesoproterozoic (ca. 1590 Ma). Metapelitic granulites from the eastern Reynolds Range contain garnet + cordierite + biotite + plagioclase + K-feldpsar + quartz + ilmenite bearing assemblages that formed at around 840 °C and 7 kbars, with the occurrence of fine grained

sillimanite at 650 °C and 3 kbars on a clockwise pressure-temperature evolution. In the Mount Boothby north region metapelitic granulites with biotite + K-feldspar + ilmenite + quartz + cordierite + garnet bearing assemblages formed at around 830 °C and 5 kbars, with the occurrence of fine-medium grained andalusite at 630 °C and 3 kbars on a clockwise pressure-temperature evolution. In situ U-Pb geochronology from monazite hosted within garnet in this region yield an age of 1573 ± 11 Ma, with monazite in retrograde biotite recording ages of 1543 ± 10 Ma, suggesting the minimum duration of granulite-facies metamorphism in this region in the order of 30 M.y. This study estimates the cooling rate to be ~4 °C Myr^{-1} based on the differences in peak temperature modelled in P-T pseudosections (~830 °C) with temperatures recorded in the garnet cores obtained from theromobarometry (~700 °C), and the difference in ages obtained from monazites in different textural locations (~30 M.y). The average heat production (recalculated at 1580 Ma) of granitic gneisses, metasediments are 11.04 and 5.71 μWm^{-3}, suggesting the burial of an enriched U- and Th- layer may provide a mechanism for long-lived, high geothermal gradient metamorphism rather than emplacement of magmatism at this time.

Keywords: granulite-facies; in situ monazite geochronology; P-T pseudosection; slow cooling; diffusion modelling.

1. INTRODUCTION

Thermal regimes necessary to generate low-pressure, high-temperature (LPHT; i.e. high geothermal gradient) metamorphism are significantly different from normal continental thermal conditions (Sandiford & Powell 1991). The advection of heat, in the form of magmas, is generally considered as the governing paradigm for LPHT metamorphism (De Yoreo *et al*. 1991) and as a result, metamorphism governed by advective heat transfer should be characterised by transient high temperatures and dramatic isobaric variations in grade (Sandiford *et al*. 1991). This model remains problematic in several LPHT terranes (Barton & Hanson 1989), particularly where the age of magmatism is significantly different (>120 Ma older) to the age of LPHT metamorphism (e.g. Mount Isa Inlier and central Arunta Province; Sandiford & Hand 1998).

The thermal evolution of Proterozoic-aged metamorphism in the Reynolds Range in the Arunta Province, central Australia, remains contentious, for the main reason that the causative mechanism for apparently long-lived high geothermal gradient metamorphism in the region is not well understood (Buick *et al*. 1998). Existing thermobarometric data (Clarke & Powell 1991; Buick *et al*. 1998; Vry *et al*. 1996) indicates that the Reynolds Range rocks experienced high-temperature (750-800 °C), high geothermal gradient (P ~ 4-5 kbar) metamorphic conditions and U-Pb zircon and monazite geochronology suggests that these thermal and physical conditions lasted for a period of time longer than approximately 30-40 M.y (Williams *et al*. 1996; Vry *et al*. 1996; Rubatto *et al*. 2001). The age of metamorphism does not appear to correspond to the age of magmatism, suggesting the existence of an unusual thermal system during the Proterozoic (Hand *et al*. 1992; Williams *et al*. 1996). However, granitic rocks in the Reynolds-Anmatjira Range region are enriched in heat producing elements (Sandiford

& Hand 1998). The Reynolds Range appears to be anomalous in that the duration of metamorphism is longer-lived than 1600 Ma metamorphism experienced by other Australian Proterozoic terranes. The age of metamorphism show this corresponds to the age of significant tectonism documented throughout Proterozoic Australia. Proterozoic terranes experienced a continental scale high-temperature thermal event during *ca*.1600 – 1570 Ma, with compressional deformation possibly caused by the collision of the Gawler Craton and the North Australian Craton, reworking much of the Arunta during this time (Betts & Giles 2006; Wade *et al*. 2006).

Studies integrating detailed in situ geochronology with modern metamorphic analysis coupled with diffusion modelling have not been applied to the rocks of the Reynolds Range region, and this has lead to an incomplete understanding of the *P-T-t* evolution of the Reynolds Range. This study is the first of its kind to use such an integrated approach to constrain the *P-T-t* evolution of the Reynolds Range. The outcome is that tighter constraints on the *P-T-t* evolution allow for a better platform with which to then investigate the drivers for low-pressure high-temperature (LPHT) metamorphism that does not obviously involve magmatism, thus assisting in the understanding of the long-standing problem of the duration, conditions and mechanisms of metamorphism in this thermally intriguing terrain.

2. GEOLOGICAL SETTING AND PREVIOUS WORK

Several authors (Karlstrom *et al*. 2001; Betts *et al*. 2002; Giles *et al*. 2002; Betts & Giles 2006; Wade *et al*. 2006) suggest a plate margin evolved along the southern margin of the North Australian Craton (*ca*. 1800 – 1600 Ma) due to protracted history of arc-related magmatism, accretionary tectonism, and episodic orogenesis, associated with a

south-dipping subduction system (Payne *et al*. 2009; Selway *et al*. 2009). It has been interpreted that during *ca*.1790 – 1770 Ma the West Australian Craton collided with the North Australian Craton, followed by amalgamation of the North Australian Craton (Wade *et al*. 2006) with the Archaean Gawler Craton (*ca*. 1740 – 1690 Ma), and accretion of several small terranes along the southern Arunta Inlier and western Gawler Craton (*ca*. 1690 – 1640 Ma; Betts & Giles 2006). The Arunta Inlier occupies an area of around 200 000 km^2, making it one of the largest exposed Proterozoic terranes in Australia (Hand & Buick 2001), that forms an E-W trending metamorphic complex surrounded by Neoproterozoic to mid-Palaeozoic intracratonic basins which once formed part of the Centralian Superbasin that covered much of Proterozoic Australia (Wade *et al*. 2006).

The Reynolds-Anmatjira Range (Figure 1) is located in the Aileron Province of the north Australian Craton approximately 150 km northwest of Alice Springs. Two main sedimentary rock groups outcrop: the Lander Rock Beds (deposited 1840-1806 Ma: Vry *et al*. 1996; Hand & Buick 2001) consisting of dominantly pelitic and psammitic metasediments and the Reynolds Range Group (deposited 1812-1785 Ma: Sun *et al.* 1995; Vry *et al*. 1996; Hand & Buick 2001) consisting of metamorphosed pelites, quartzites, marbles and marls. Earliest metamorphism only affected the basement Lander Rock Beds prior to and during granite emplacement at *ca*.1820 – 1810 Ma (Collins & Vernon 1991; Collins & Williams 1995; Cartwright *et al.* 1999; Rubatto *et al*. 2001; Rubatto *et al*. 2006). A second generation of granite emplacement, affecting both the Lander Rock Beds and the Reynolds Range Group, occurred *ca*.1780 Ma resulting in minor deformation and localised amphibolite facies contact metamorphism (Collins & Williams 1995; Buick et al. 1997; Buick et al. 1999; Hand & Buick 2001).

These granites are significantly enriched in heat producing elements with a mean heat production rate at *ca*. 1600 Ma of ~8 μWm^{-3} (Sandiford & Hand 1998), and an average heat production rate at *ca*. 1580 Ma of 4 – 12 μWm^{-3} from granitic gneisses and metasediments in this study (Section 5. 6). A major event at 1590 – 1570 Ma, known locally as the Chewings Orogeny, was part of a long-lived continental-scale event (Buick *et al*. 1998; Vry *et al*. 1996; Hand & Buick 2001; Rubatto *et al*. 2006) affecting both the Lander Rock Beds and Reynolds Range Group, involving low to medium pressures (4 to 5.5 kbar) and increased in grade from greenschist facies to granulite facies (400 - 800 °C) eastwards along the length of the range, with no obvious association with magmatism (Hand & Buick 2001). The mid- Palaeozoic Alice Springs Orogeny (400 – 300 Ma), produced discrete ('retrograde') shear zones from greenschist to mid-amphibolite facies grade and resulted in differential exhumation of the terrain (Dirks *et al*. 1991; Buick *et al*. 1998; Cartwright & Buick 1999; Hand & Buick 2001).

The duration of Chewings-aged metamorphism in the Reynolds Range has been advocated to be long on the basis of appreciable age differences between U-Pb zircon (oldest metamorphic age 1594 ± 6 Ma) and U-Pb monazite ages (Table 1, Figure 2; *ca*. 1575 Ma: Williams *et al*. 1996; Rubatto *et al*. 2001; Rubatto *et al*. 2006). Slow cooling has been advocated on the basis of this difference between zircon and monazite ages (Williams *et al*. 1996; Rubatto *et al*. 2001; Rubatto *et al*. 2006), as well as on the basis of a large spread in U-Pb rutile ages and Pb-Pb garnet ages (1576 ± 6 Ma to 1544 ± 8 Ma; Buick *et al*. 1999). The spread in rutile and garnet ages have been used to suggest a (slow) cooling rate of 3 $°CMa^{-1}$ from the peak conditions of around 800 °C. Although several studies (Williams *et al*. 1996; Rubatto *et al*. 2001) have been undertaken in the Reynolds Range, geochronology obtained from zircons and monazites were not

performed in situ, therefore the petrographic context of the existing geochronology remains unknown and age difference may reflect different chemical controls on the growth of the accessory minerals rather than variations in *P-T* (Kelsey *et al*. 2008). Monazite and zircon ages obtained by Rubatto *et al* (2006) were acquired from the same rock however this data was never linked to the *P-T* evolution of the range.

3. METAMORPHIC PETROLOGY

3.1 General overview

Samples used in this study encompass a range of locations widely distributed throughout the eastern Reynolds Range to allow for tight constraints to be placed on the spatial variation in *P-T-t* conditions.

3.2 Petrological groups

Ten samples were chosen from various locations based on their mineralogy and textures. The metapelites used in this study have limited evidence of mineral reaction; therefore the interpretation of peak and post-peak assemblages is based on grain size and spatial distribution (Kelsey *et al*. 2007). High-temperature metamorphic assemblages from metapelites in the Reynolds Range are useful for metamorphic analysis due to their sensitivity to temperature and pressure changes, and commonly have abundant monazite (Dirks *et al*. 1991; Kelsey *et al*. 2007). Key petrological relationships are shown in Figure 3 (a-l). Sample locations are shown in Figure 4.

3.2.1 GAS PIPELINE LOCALITY

Sample RR03

This assemblage (grid reference 53K 322372 7497549) comprises coarse-grained, porphyroblastic garnet (≤ 5mm long), biotite, quartz, plagioclase, K-feldspar, cordierite, ilmenite, magnetite and fine-grained sillimanite. The majority of garnet grains are free from inclusions, although a number have inclusions of biotite and minor rounded quartz. Coexisting ilmenite and magnetite commonly occur within fine-grained biotite and is rarely seen in direct contact with garnet. Cordierite contains occasional inclusions of oriented prismatic sillimanite. Fibrous sillimanite is common along garnet grain boundaries in direct contact with cordierite.

Sample RR04B

This assemblage (grid reference 53K 322372 7497549) comprises coarse-grained orthopyroxene (≤ 4 cm long), coarse-grained porphyroblastic garnet (≤ 1 cm diameter), biotite, quartz, plagioclase, cordierite and magnetite comprise the assemblage. This sample is domainal with extremely coarse orthopyroxene porphyroblasts with garnet and plagioclase in one domain, and biotite, magnetite ± garnet ± cordierite in the other domain. Magnetite is often in contact with biotite but can be found as inclusions within orthopyroxene, separated by a corona of quartz. Orthopyroxene and plagioclase are in direct contact and are separated by fine-grained biotite with dispersed magnetite grains within the fine-grained material. Garnet is occasionally in direct contact with orthopyroxene and plagioclase.

Sample RR051C

The assemblage (grid reference 53K 322372 7497549) comprises biotite, quartz, cordierite and ilmenite. Biotite is medium to fine grained and forms a weak fabric. Aggregates of coarse-grained quartz and cordierite are surrounded by biotite. Coarse-grained magnetite is isolated from quartz and cordierite by biotite.

3.2.2 MOUNT BOOTHBY NORTH

Sample 09-2

In sample Boothby 09-2 (grid reference 53K 325078 7505909), elongate garnet (≤ 3 mm), biotite, cordierite, K-feldspar, plagioclase, sillimanite, quartz, fine-medium grained andalusite and ilmenite comprise the assemblage. Garnet has inclusions of coarse-grained oriented sillimanite with fibrolite common on grain boundaries in contact with biotite and cordierite. Coarse-grained sillimanite occurs only as inclusions within garnet. K-feldspar and elongate, oriented biotite are interspersed with ilmenite and medium to coarse aggregates of cordierite. Fine-grained plagioclase only occurs with K-feldspar and cordierite. Fine-medium grained andalusite is only found within fine-medium grained biotite and is separated from garnet by cordierite.

Sample Boothby 09-2A

In sample Boothby 09-2A (grid reference 53K 325078 7505909), poikiloblastic, elongate, garnet (≤ 2 cm long), cordierite, sillimanite, biotite, quartz, ilmenite, fine-medium grained andalusite, fine-grained sillimanite (fibrolite) and magnetite comprise the assemblage. Inclusions of magnetite within ilmenite are rare. Aligned coarse-grained sillimanite inclusions are restricted to garnet and cordierite and do not penetrate

adjacent grains. Fine-grained sillimanite occurs at grain boundaries of cordierite and occasionally on garnet grain boundaries. An occasional intergrowth between biotite and quartz can be seen when in contact with garnet. Rare fine-medium grained andalusite is only found in direct contact with quartz and fine-medium grained biotite.

Sample Boothby 09-1

In sample Boothby 09-1 (grid reference 53K 325078 7505909), poikiloblastic garnet (≤ 1 cm diameter), cordierite, biotite, quartz and ilmenite comprise the assemblage. Biotite grains within garnet grains have the same orientation as biotite grains forming a fabric on the edges of garnet. Garnet grains vary in size and are rich in inclusions of elongate biotite and rounded quartz with varying orientation to the fabric. Biotite commonly forms a moderate fabric around garnet. Cordierite is in local contact with fine-grained biotite. Ilmenite is commonly found within the biotite fabric.

3.2.3 MOUNT BOOTHBY EAST

Sample Boothby 09-4D

In sample Boothby 09-4D (grid reference 53K 325645 7502082), poikiloblastic garnet (≤ 1.5 cm long), sillimanite, cordierite, K-feldspar, biotite, ilmenite and quartz comprise the assemblage. Cordierite contains inclusions of oriented, prismatic sillimanite. Garnets are rich with inclusions of rounded biotite and quartz, with coarse-grained sillimanite of varying orientations. A strong fabric defined by sillimanite, biotite, cordierite and K-feldspar is separated from garnet by coarse-grained quartz interspersed with medium-grained cordierite.

3.2.4 PEAKED HILL

Sample PH-05

In sample PH-05 (grid reference 53K 324861 7513810), poikiloblastic, elongate garnet (≤ 2 cm), cordierite, biotite, quartz, ilmenite, K-feldspar, sillimanite and plagioclase comprise the assemblage. Strongly aligned aggregates of prismatic and fibrous sillimanite, biotite, fine-grained K-feldspar, ilmenite, quartz and plagioclase wrap around poikiloblastic garnet. Garnet grains occasionally have plagioclase coronas and are rich with inclusions of oriented prismatic sillimanite with minor elongate biotite and rounded quartz. K-feldspar is commonly in direct contact with cordierite and aggregates of biotite and rarely in contact with garnet. Cordierite generally has inclusions of prismatic sillimanite with fibrous sillimanite common on grain boundaries. Rare spinel is in direct contact with ilmenite, and ilmenite within biotite is rare.

3.2.5 REYNOLDS RANGE

Sample RR2007-07

In sample RR2007-07 (grid reference 53K 302543 7515071), poikiloblastic garnet (≤ 1.5 cm), biotite, cordierite, perthitic K-feldspar, sillimanite, ilmenite and quartz comprise the assemblage. Cordierite and poikiloblastic K-feldspar with inclusions of fine-grained, elongate biotite and rounded quartz define a weak fabric. Garnet has inclusions of elongate biotite and rounded quartz. Cordierite has sillimanite inclusions generally oriented in the same direction that never penetrate the adjoining minerals.

4. ANALYTICAL METHODS

4.1 Mineral Chemistry

Electron Probe Micro-Analysis (EPMA) was done in order to determine mineral chemistry for the purposes of constraining the thermobarometric evolution and diffusion cooling histories in the southeastern Reynolds Range. Mineral compositions were obtained using a Cameca SX51 Electron Microprobe at the University of Adelaide. Quantitative analyses were performed using a beam current of 20 nA and an accelerating voltage of 15kV. Complete analyses of minerals are shown in Appendix 1. Garnet profiles from all samples are provided in Appendix 2. X_{Fe}* ($Fe^{2+}/(Fe^{2+}+Mg)$) and X_{Fe} ($Fe^{2+}/(Fe^{2+}+Mg+Ca+Mn)$) was calculated for use in pressure-temperature pseudosections and X_{Mg} ($Mg/(Mg+Fe^{2+})$) was calculated for use in garnet-diffusion modelling.

4.2 Quantified metamorphic analysis

4.2.1. PRESSURE-TEMPERATURE PSEUDOSECTIONS

Pressure-temperature (*P-T*) pseudosections were calculated using bulk compositions obtained from whole rock chemistry by solution ICP-MS, from Amdel Laboratories, Adelaide, on samples Boothby 09-2, Boothby 09-2A, Boothby 09-4D, PH-05, RR2007-07 and RR03. *P-T* pseudosections for all these samples were calculated using the phase equilibria modelling program THERMOCALC v3.33 (June 2009, update of Powell and Holland 1988) using the internally consistent data set of Holland & Powell (1998; dataset tcds55 November 2003 update), for the geologically realistic model chemical system NCKFMASHTO (Na_2O-CaO-K_2O-FeO-MgO-Al_2O_3-SiO_2-H_2O-TiO_2-Fe_2O_3). The modelling for this system uses the *a-x* relationships of White *et al*. (2007) for

biotite, garnet and silicate melt, Holland and Powell (1998) for cordierite, Holland and Powell (2003) for K-feldspar and plagioclase, White *et al*. (2002) for orthopyroxene and magnetite, Coggon and Holland (2002) for muscovite, and White *et al*. (2000) for ilmenite solid-solution.

4.2.2. THERMOBAROMETRY

Thermobarometry was performed to determine the temperature preserved by garnet grains. *P-T* estimates were done using EPMA compositional analyses described in Section 5.1. Pressure and temperature estimates presented in this study were obtained through calculations on sets of independent reactions between mineral end members using selected core analyses of garnet with biotite, by incorporating results from *A-X* (Powell *et al*. 1998; Holland & Powell 2003), into THERMOCALC v3.21 (mode 3). Temperatures obtained from mineral pair thermobarometry were used to compare the differences between peak temperatures calculated from pseudosections to the temperature preserved by mineral grains. This will help in distinguishing whether a garnet has been chemically reset and aid in the interpretation of the duration required to reset garnet chemistry. Representative output files from *A-X* are provided in Appendix 3, and output files from THERMOCALC mode 3 are provided in Appendix 4.

4.3 In situ LA-ICP MS monazite geochronology

Samples were selected for in situ monazite U-Pb geochronological analysis primarily based on petrological relationships of monazite to major silicate minerals observed in thin section. Preparation for in situ geochronology involved back-scattered imaging was done using a Philips XL30 SEM with a beam current of 20 kV and a spot size of 4 µm,

to characterise and document the textural location of monazite in thin section. In situ U-Pb monazite dating was undertaken by laser ablation- inductively coupled plasma mass spectrometry (LA-ICPMS) at the University of Adelaide following the method outlined in Payne *et al*. (2008). U-Pb isotopic analyses were acquired using a New Wave Nd Yag 213 UV in a helium atmosphere attached to an Agilent 7500cs ICPMS, with a spot size of 12 µm, laser intensity of 75% and repetition rate of 5 Hz. The total acquisition time for each analysis was 90 seconds and involved 30 seconds of background measurement, 10 seconds with the shutter closed to allow beam and crystal stabilisation, and 50 seconds of sample analysis. Analyses measured isotopes ^{204}Pb, ^{206}Pb, ^{207}Pb and ^{238}U for 10, 15, 30 and 15 ms respectively. Common-Pb was not corrected in age calculations. However, monitoring of the ^{204}Pb isotope peak allowed for analyses to be removed if appreciable amounts of common-Pb were observed throughout analysis.

Monazite age calculations were determined using the program 'Glitter', which was developed at Macquarie University, Sydney (Jackson *et al*. 2004). U-Pb fractionation was corrected using the external monazite standard 44069 (TIMS normalisation data: ^{206}Pb/^{238}U = 426 ± 3 Ma: Aleinikoff *et al*. 2006), with accuracy monitored by repeat analysis of internal monazite standard Madel monazite standard (TIMS normalisation data: ^{207}Pb/^{206}Pb age = 490.7 Ma; ^{206}Pb/^{238}U age = 514.8 Ma; ^{207}Pb/^{235}U age = 510.4 Ma: Payne *et al*. 2008). Prior to unknown analyses, corrected age accuracy was established by regular analyses of an in-house monazite standard (94-222/ Bruna NW, *ca*. 450 Ma: Payne *et al*. 2008). Throughout the duration of this study the reported normalised average ages for Madel are ^{207}Pb/^{206}Pb age = 481 ± 20 Ma; ^{206}Pb/^{238}U age = 496 ± 25 Ma; ^{207}Pb/^{235}U age = 493 ± 32 Ma, and the reported normalised average ages for 44069 are ^{207}Pb/^{206}Pb age = 424.4 ± 9.2 Ma; ^{206}Pb/^{238}U age = 420.9 ± 4.9 Ma;

$^{207}Pb/^{235}U$ age = 423.8 ± 2.9 Ma. Conventional concordia and weighted average plots were generated using Isoplot v4.11 (Ludwig 2003). All quoted ages are $^{207}Pb/^{206}Pb$ ages as the data comprises ages older than *ca*. 1100 Ma. All errors quoted in Tables and shown on the concordia diagrams are at the 1σ level. All monazite analyses are given in Table 2.

4.4 Temperature-time modelling

Temperature-time models were constructed using the diffusion modelling code of Robl *et al*. (2007) based on the diffusion rates of Fe-Mg between garnet and biotite. This modelling code calculates the diffusion equation using a series of input parameters for the Fe-Mg diffusion within garnet, enabling the user to match a measured diffusion-related compositional profile to a cooling rate and/or explore compositional profiles that would result from a specified heating/cooling history. The extent of Fe-Mg re-equilibration is both temperature and rate of cooling dependent (Hauzenberger *et al*. 2005; Robl *et al*. 2007).The application of the diffusion modelling code of Robl *et al*. (2007) comes with a number of assumptions: (1) all garnet crystals being modelled are spherical and completely surrounded by a biotite reservoir, and thus there is chemical equilibrium between the two mineral phases, (2) only the binary exchange of Fe and Mg is considered, (3) the garnet crystal has no zoning and zoning occurred only during retrogression/cooling, and (4) there is infinitely fast diffusion within the biotite reservoir and as a consequence there is no biotite chemical zoning (Dodson 1986; Hauzenberger *et al*. 2005; Robl *et al*. 2007). Each assumption for use in the diffusion modelling code was deemed to be reasonable in relation to this study's samples. The Fe-Mg diffusional constants of Ganguly *et al.* (1998) were used to model the diffusion between garnet and

biotite. Samples were selected based on garnet being in direct contact with coarse and/or abundant biotite and the measured chemical zonation profile. Garnet profiles with considerable fluctuations of Mg at the outermost rim coupled with relatively flat cores were favoured, notably the radial section from the garnet core to the outermost rim in contact with biotite. EPMA compositional data integrated with diffusive properties of 2 samples were chosen to model the thermal and cooling regime. Sample RR2007-07 from the western area of the east Reynolds Range (Figure 4) and sample PH-05 from the northeastern area of the east Reynolds Range contain garnet porphyroblasts with biotite, exhibiting minimal retrograde textures.

Calculated peak temperatures from pseudosections were used as starting temperatures (of cooling). Varying cooling rates were experimented with to enable cooling profiles to be developed that correlate to the garnet profile analysed. Five linear cooling models with relatively slow cooling rates of 1, 3, 5, 10 and 20°C/Ma were applied to each of the samples in order to constrain cooling rates of each rock.

4.5 Heat production

Heat production data was collected to assess the potential role of heat production as a mechanism for sustaining long-lived metamorphism in the central Arunta Province. Data was collected over a limited area but from rock types that are representative of the broader Reynolds-Anmatjira region to enable the results to be considered in a broader context.

Heat production was measured with a Gamma Ray Spectrometer (GRS). Gamma Ray Spectrometers measure the intensity and energy of gamma radiation, enabling the source of the radiation to be determined. Gamma rays emitted from the radiogenic

isotopes from the decay series K^{40}, U^{238}, U^{235} and Th^{232} are of sufficient energy and intensity to be measured by a GRS. During radiogenic decay, ^{238}U and ^{232}Th do not emit gamma rays however the gamma ray emissions from daughter products are measurable (Grasty & Minty 1995).

Uranium (ppm), Thorium (ppm) and Potassium (%) concentrations of a rock were collected by placing the GRS on a relatively fresh, flat outcrop surface. The total acquisition time for each analysis was 180 seconds. Heat production was calculated to determine the heat production rate at *ca*. 1580 Ma to correspond to analysed aged metamorphism. All GRS analyses can be found in Appendix 5, and the details of the analytical method can be found in Barker (2010).

5. RESULTS

5.1 Mineral Chemistry

5.1.1. GARNET

Garnet is almandine-rich, with variable proportions of pyrope and low to negligible proportions of grossular and spessartine. Representative analyses from all samples are provided in Table 3. X_{Fe}*(Fe^{2+}/(Fe^{2+}+Mg)) values in sample Boothby 09-1 range between 0.79–0.86, with a slight increase of X_{alm} and decrease of X_{pyr} at the rim of the grains (Figure 5a). In sample 09-2, X_{Fe}* values range between 0.82 and 0.85, and shows a minor decrease of X_{alm} and increase of X_{pyr} in the core and is otherwise a relatively flat profile (Figure 5b). In sample PH-05, X_{Fe}* values range between 0.75 and 0.81, with zonation profiles varying within the sample. Some garnets show an increase in X_{alm},

decrease in X_{pyr} and a slight decrease in X_{gr} from core to rim, whereas others show a decrease in X_{alm}, an increase in X_{pyr} and a slight decrease in X_{gr} with no change in X_{spss} in either grain (Figure 5c). In sample 09-4D, X_{Fe}* values vary from 0.82 to 0.84, and shows a slight increase of X_{pyr} and decrease of X_{alm} at the rim of the grain (Figure 5d). In sample RR03 the X_{Fe}* values range between 0.65 and 0.73, and show no systematic variation between the core and the rim (Figure 5e). In sample RR04B, X_{Fe}*values range between 0.65 and 0.71, with zoning evident as the core is relatively flat with an increase of X_{alm} and decrease of X_{pyr} at the rim (Figure 5f). In sample Boothby 09-2A, X_{Fe}* values range between 0.79 and 0.85 and shows no systematic variation between the core and the rim (Figure 5g), and sample RR2007-07 is 0.82 (Figure 5h), and shows a decrease in X_{alm} and increase in X_{pyr} at the rim of the grain.

5.1.2. BIOTITE

Biotite from all samples are magnesian, moderately TiO_2 rich (2.78 – 4.40), Al_2O_3 rich (14.91 – 19.32) and vary in composition between samples. Representative analysis of biotite from all samples is shown in Table 4. Two generations of biotite are present in sample PH-05, 'regular' biotite (bi_1) and apple green biotite (bi_2). Bi_1 has an X_{Mg} ($Mg/(Mg+Fe^{2+})$) of 0.56 – 0.65 with a TiO content of 3.7 to 4.4 wt%, and bi_2 has an X_{Mg} of 0.57 with a TiO_2 content of 0.01 and 0.04 wt % (Table 4). Although bi_2 has less TiO_2, it has slightly more Al_2O_3 and FeO than bi_1.

5.1.3. ORTHOPYROXENE

In sample RR04B, orthopyroxene (Table 5) has an X_{Fe}* ($Fe^{2+}/(Fe^{2+}+Mg)$) between 0.40 (rim) and 0.45 (core). The *y*(opx) (Si+Al-2) content ranges between 0.06 to 0.114.

5.1.4. CORDIERITE

Cordierite in sample PH-05 shows variable X_{Fe}*. Cordierite grains with sillimanite inclusions range in X_{Fe}* from 0.24 to 0.27 whereas cordierite grains without sillimanite inclusions range in X_{Fe}* from 0.19 to 0.22 (Table 5). Sample RR03 has similar X_{Fe}* values, ranging from 0.19 to 0.22 in cordierite grains with no sillimanite inclusions and X_{Fe}* from 0.23 to 0.25 in cordierite at grain boundaries with fibrous sillimanite. In sample RR2007-07, cordierite has higher X_{Fe}* values ranging from 0.35 to 0.47.

5.1.5. FELDSPARS

In samples Boothby 09-4D and Boothby 09-2, alkali feldspar is K-rich with the orthoclase content ranging from 0.77-0.91 and 0.85 – 0.87, respectively (Table 5). In sample RR04B, plagioclase is Na-rich with X_{Ab} (Na/(K+Ca+Na)) with values ranging from 0.64-0.66.

5.1.6. ILMENITE

In sample RR2007-07, ilmenite has an MnO content of 0.1 wt % (Table 5). In sample PH-05, ilmenite has an MnO content of 0.65 wt% and Fe_2O_3 of 0.86 wt %.

5.1.7. MAGNETITE

In sample RR03, magnetite has an Al_2O_3 content of 0.19 - 0.22 wt % which corresponds to X_{Al} (Al/(Al+Fe^{3+}+2Ti)) of 0.0058 to 0.0065. The TiO_2 content is 0.01 wt % (Table 5) and the Cr_2O_3 content is 0.32 wt %.

5.1.8. SPINEL

In sample PH-05, spinel is hercynitic with an X_{Fe} of 0.78. Spinel has low ZnO contents of 0.02 wt %, which corresponds to X_{Zn} (Zn/(Zn+Fe^{2+}+Mg+Mn)) of 0.19, and Cr_2O_3 content is 0.61 wt % (Table 5). Spinel has Fe_2O_3 content of 0.62 wt % and TiO_2 content of 0.03 wt %.

5.2 Pressure-Temperature pseudosections

The calculated peak conditions vary from 860 ± 30 °C and 6 – 7 kbars in the western side of the eastern Reynolds Range to 830 ± 20 °C in the northeast (Table 6). A general trend in all samples show that garnet increases in X_{Ca} (Ca/(Ca+Mn+Mg+Fe)) and X_{Fe*}, cordierite increases in X_{Fe*}, and K-feldspar shows an increase in X_{Na} (Na/(K+Ca+Na)) to lower temperatures and pressures. Lower temperatures and pressures also show a decrease in the proportion of X_{Ca} (Ca/(K+Ca+Na)) in plagioclase *(*Figure 6a-f*).* Modal abundances of garnet decrease down pressure, whilst the abundance of cordierite, sillimanite, plagioclase and K-feldspar increase (Figure 7a-f).

5.2.1. GAS PIPELINE LOCALITY

In sample RR03 (Figures 3a, 3b, 4), the mineral assemblage interpreted to define the peak assemblage (garnet + cordierite + plagioclase + K-feldspar + biotite + ilmenite + liquid + quartz) defines *P-T* conditions of *ca*. 840 °C and 6.5 – 7 kbars in the *P-T* pseudosection (Figures 6a, 7a, 8). Fine-grained retrograde magnetite and fibrolite occurs to lower temperatures and pressures than the peak assemblage and is calculated to occur at *ca*. 660 °C and 3 – 3.2 kbars.

5.2.2. MOUNT BOOTHBY NORTH

In sample Boothby 09-2A (Figures 3g, 3h, 4), the mineral assemblage interpreted to define peak assemblage (garnet + cordierite + K-feldspar + biotite + quartz + ilmenite) define the *P-T* conditions of *ca.* 830 °C and 5- 6 kbars in the *P-T* pseudosection (Figure 6b, 7b, 9). Fine-grained retrograde andalusite and fibrolite occurs at lower temperatures and pressures to the peak assemblage and is calculated to occur at *ca.* 630 °C and 3 – 3.6 kbars.

In sample Boothby 09-2 (Figures 3i, 4), the mineral assemblage interpreted to define the peak assemblage (garnet + cordierite + K-feldspar + biotite + quartz + ilmenite) defines *P-T* conditions of *ca.* 830 °C and 5 – 6 kbars in the *P-T* pseudosection (Figures 6c, 7c, 10). Fine-grained retrograde andalusite, fibrolite and an increase in plagioclase occurs at lower temperatures and pressures to the peak assemblage and is calculated to occur at *ca.* 650 °C and 2.5 – 3 kbars.

5.2.3. MOUNT BOOTHBY EAST

In sample Boothby 09-4D (Figures 3k, 4), the mineral assemblage interpreted to define the peak assemblage (garnet + cordierite +sillimanite + K-feldspar + quartz + ilmenite) define *P-T* conditions of *ca.*850 °C and 5.6 – 6.4 kbars in the *P-T* pseudosection (Figures 6d, 7d, 11). Fine-grained retrograde sillimanite and biotite occurs at lower pressure and temperatures to the peak assemblage and is calculated to occur at *ca.* 680 °C and 3.6 – 4.1 kbars.

5.2.4. PEAKED HILL

In sample PH-05 (Figures 3l, 4), the mineral assemblage interpreted to define the peak assemblage (garnet + cordierite + biotite + sillimanite + quartz + ilmenite + K-feldspar + plagioclase) defines *P-T* conditions of *ca*. 820 °C and 6-7 kbars in the *P-T* pseudosection (Figures 6e, 7e, 12). The peak conditions straddle the biotite out line owing to the difficulty in interpreting the timing of growth of biotite. Fine-grained retrograde sillimanite is calculated to occur at *ca*. 750 °C and 4-5 kbars.

5.2.5. REYNOLDS RANGE

In sample RR2007-07 (Figures 3e, 4), the mineral assemblage interpreted to define the peak assemblage (garnet + cordierite + sillimanite + K-feldspar +quartz ilmenite ± biotite) defines *P-T* conditions of *ca.*860 °C and 6-7 kbars in the *P-T* pseudosection (Figures 6f, 7f, 13). Difficulty in interpreting the timing of growth of biotite results in peak conditions straddling the biotite out line. Fine-grained sillimanite is calculated to occur at *ca*. 730 °C and 3.5 – 4.5 kbars.

5.3 Thermobarometry

A summary of temperatures for each sample is shown in Table 7. Temperatures obtained from end-member calculations show that garnet cores record temperatures lower than peak *T* modelled in *P-T* pseudosections. Temperatures vary from 649 °C at ~6 kbars in sample PH-05 to 806 °C at ~7 kbars in sample RR2007-07. The garnet grain from sample RR2007-07 is large in size (~5 mm in diameter) and records higher temperatures in conventional thermobarometry in comparison to garnet grains in other samples. This is due to diffusion as a consequence of retrograde metamorphism. Diffusion is grain size dependent therefore this would explain why the smaller garnet

grains in other samples (RR03, Boothby 09-1, Boothby 09-2A) do not record the modelled peak *T*, whilst the larger garnet grains do.

5.4 LA-ICP MS monazite geochronology

Sample RR04B

Twenty two analyses were conducted on 8 monazite grains that are texturally hosted within biotite or orthopyroxene (Figure 14). The monazite grains analysed are rounded, with occasional elongate and angular grains, and are up to 200 µm in length. Compositional variation was not observed with BSE imaging (Figure 14e). Two distinct age populations are present in this sample with monazite grains analysed within orthopyroxene preserving older ages than those analysed within biotite. The older group has a weighted average $^{207}Pb/^{206}Pb$ age of 1573 ± 11 Ma (*n*=16, MSWD 0.065; Figure 14a), and originates from monazite grains within orthopyroxene. The younger group has a weighted average $^{207}Pb/^{206}Pb$ age of 1549 ± 21 Ma (*n*=4, MSWD 0.19; Figure 14c), and originates from monazite grains within biotite.

Sample RR501C

Twenty four analyses were conducted on eleven monazite grains that are texturally hosted within cordierite (matrix) and interpreted retrograde biotite (Figure 15f). Monazite grains within cordierite and biotite are up to 150 µm in length, with most generally around 100 µm. Most grains are unzoned under BSE imaging (Figure 15e). However, some grains within biotite displayed faint compositional zoning with slightly darker cores (Figure 15g), but when analysed show no distinct variation in age between either domain. Two distinct age populations are present in this sample with monazite grains analysed within the matrix preserving older ages than those analysed within

retrograde biotite. The older group has a weighted average $^{207}Pb/^{206}Pb$ age of 1563 ± 23 Ma (*n*=4, MSWD 0.057; Figure 15a), and originates from monazite grains within matrix cordierite. The younger group has a weighted average $^{207}Pb/^{206}Pb$ age of 1543 ± 10 Ma (*n*=18, MSWD 0.116; Figure 15c), and originates from monazite grains within biotite.

Sample Boothby 09-2A

Eleven analyses were conducted on 7 monazite grains texturally within garnet. Monazite grains are approximately 20 to 50 µm in length, and less commonly up to 100 µm. Compositional variation is not observed with BSE imaging (Figure 16c). The weighted average $^{207}Pb/^{206}Pb$ age of monazite in this sample is 1573 ± 12 Ma (*n*=11, MSWD 0.112; Figure 16b).

Sample Boothby 09-1

Seventeen analyses were conducted on ten monazite grains texturally in contact with garnet and biotite. Monazite grains are approximately 50 µm in size, and less commonly up to 100 µm. Compositional variation is not observed with BSE imaging (Figure 17e). Two distinct age populations are present in this sample with monazite grains analysed within garnet preserving older ages than those analysed within retrograde biotite. The older group has a weighted average $^{207}Pb/^{206}Pb$ age of 1563 ± 28 Ma (*n*=2, MSWD 0.15; Figure 16c), and originates from monazite grains within garnet. The younger group has a weighted average $^{207}Pb/^{206}Pb$ age of 1544 ± 11 Ma (*n*=14, MSWD 0.17; Figure 16a), and originates from monazite grains within biotite.

5.5 Temperature-time modelling

A temperature-time profile for sample PH-05 was generated using the calculated temperature from *P-T* pseudosection as a starting temperature (830 °C; Figure 6e). An X_{Mg} value of 0.48 for biotite and a radius of 232.4 μm for garnet produced a cooling profile that indicates the rock cooled from 830 °C through to 680 °C, at a rate of between 3 and 8°C/Ma (Figure 18b). This suggests a duration of between 20 and 50 M.y. A temperature-time profile for sample RR2007-07 was generated using the starting temperature of ~780 °C (Figure 18c). An X_{Mg} value of 0.43 for biotite and a radius of 1191.2 µm for garnet produced a cooling profile that indicates the rock cooled from 780 °C through to 650 °C, suggesting the duration of metamorphism was between 38 and 120 M.y (Figure 18d).

5.6 Heat production

The average heat production (recalculated at 1580 Ma) on the basis of the above geochronological results of 364 analyses of granitic gneisses, metasediments and inter-layered felsic and mafic gneisses are 11.04, 5.71 and 5.76 μWm^{-3} respectively (Table 8). The minimum and maximum heat production values (*c*. 1580 Ma) vary between lithologies, with granitic gneisses recording the highest heat production values ranging between 1.45 and 45.37 μWm^{-3}.

6. DISCUSSION AND CONCLUSION

Previous studies have resulted in an incomplete understanding of the *P-T-t* evolution of the Reynolds Range because those studies have not integrated geochronology with *P-T* information, therefore the integration of detailed in situ geochronology with modern

metamorphic analysis coupled with diffusion modelling allows for a relatively complete *P-T-t* evolution of such a problematic thermal terrane to be deduced.

6.1 P-T paths

Metamorphic *P-T-t* paths provide insight into the structural and thermal evolution of an area (Spear 1992; Vernon 1996) and the use of analysed mineral zoning and interpreted changes in mineral abundance as a function of mineral reaction provide excellent opportunities for more accurate definition of *P-T* paths in granulite facies terranes. Despite these advantages *P-T* paths for the prograde part of granulite facies rocks are difficult to interpret due to two reasons: (1) largely due to the erasing of the prograde mineralogical history and, (2) the effect of melt loss on modifying the overall bulk composition of the rocks (Harley 1989; Kelsey 2008). In granulite facies metamorphism, melt loss is an important process at it controls the composition and proportion of residual melts in the granulite restite (White & Powell 2002; Kelsey *et al*. 2008). The rocks used in this study are residual. The *P-T* path of the rocks' evolution as depicted on each psuedosection is only a broad path as a pseudosection is a result that reflects the average bulk composition of all compositional domains in a rock (Spear 1992; Vernon 1996; Kelsey *et al*. 2007). Additionally, reaction microstructures do not uniquely define a *P-T* path (Vernon 1996; Kelsey *et al.* 2003).

The *P-T* path of each sample was determined using the combination of petrographic observations, grain size and spatial distribution, trends in mineral chemistry (from core to rim) and the trends in inferred mineral proportions as a consequence of retrograde reactions (Vernon 1996; Brown 2002; Kelsey *et al.* 2008). The presence of fine-grained sillimanite, fine-grained andalusite, fine-grained magnetite and biotite moving down

pressure and temperature, were interpreted as being part of the retrograde assemblage and therefore occur at lower pressures and temperatures than the peak assemblage. The coupled textural and modelled relationships suggest this region underwent a decompression-cooling, clockwise style retrograde evolution from peak conditions of *ca*. 830 - 860 °C and 5.5 - 7.5 kbars to *ca*. 630 – 730 °C and 2.7 - 3.8 kbars. The results found in this study differ considerably to studies by Clarke *et al.* (1991) and Collins & Vernon (1991) who suggest an anticlockwise *P-T* path. However the proposed *P-T* in these studies is not geochronologically constrained, and has been shown to be the result of temporally unrelated metamorphic events (Hand *et al*. 1992). Bohlen (1991) suggests the anticlockwise-isobaric cooling *P-T-t* path in granulites is indicative of a compressive environment with intrusions of large volumes of igneous material within the crust, based on the thermal models of Wells (1980). Magmatism in this terrane metamorphism pre-dates metamorphism, therefore the results found by Clarke *et al.* (1991) and Collins & Vernon (1991) are not applicable. In this study evidence for only one metamorphic event has been found, and therefore the *P-T* paths in figures 6a-f is that of a single metamorphic cycle. The integration of this information with geochronological evidence, strengthen the interpretation of the *P-T-t* path by determining if the ages obtained represent one or two metamorphic events.

6.2 Duration of metamorphism in Reynolds Range

Monazite is frequently used in U-Pb geochronology of metamorphic rocks as it grows as a metamorphic mineral over a broad stability range, has greater resistance to radiation damage, and commonly yield concordant ages in the U-Pb system without evidence of Pb loss that is common seen in zircon (Catlos *et al*. 2002; Cherniak *et al*. 2004; Cherniak & Pyle 2008).

The ages obtained from in situ monazite analysis from the gas pipeline locality suggest these rocks experienced granulites facies metamorphism over a duration of a minimum of ~30 Myr, from *ca*. 1573 – 1543 Ma. The older ages obtained in this study are similar to monazite ages obtained by Williams *et al*. (1996; 1576 ± 6 Ma). The older ages are typically obtained from monazite hosted by garnet, orthopyroxene, matrix cordierite, whereas the younger ages are typically from monazite hosted within biotite. Considering the comparatively high metamorphic grade reached in this region, it is possible that these U-Pb monazite ages could be interpreted as being closure temperature ages rather than growth ages (Cherniak & Pyle 2008; Gardés & Montel 2009; Spear & Pyle 2010). Some studies suggest monazite can reach temperatures in excess of 900 °C for a 100 µm grain and is still able to preserve growth ages for the duration of a typical metamorphic event (Rubatto *et al*. 2001; Catlos *et al*. 2002; Gardés & Montel 2009). Several studies (Kelsey *et al*. 2003; Cherniak *et al*. 2004; Cherniak & Pyle 2008) suggest that closure temperature is controlled by many factors and that there is no single closure temperature for any given mineral as it is grain size and cooling rate dependent and Pb diffusion in monazite is sluggish enough to preserve old growth ages.

Peak temperatures of metamorphism in the gas pipeline locality reached *ca*. 840 °C, with monazite grains in garnet/orthopyroxene recording older ages than monazite grains in the matrix, suggesting that the monazite ages obtained in this study are growth ages rather than closure temperature ages (Catlos *et al*. 2002; Cutts *et al*. 2010). The difference in ages of monazite in garnet/orthopyroxene and in retrograde biotite, suggest the minimum duration of the metamorphic event in the gas pipeline region is 29 ± 16.2 Ma. In samples from the north of Mount Boothby in situ monazite ages of 1573 ± 12 Ma and 1544 ± 11 Ma were obtained. Peak temperatures of metamorphism in Mount

Boothby North reached *ca*. 830 °C, with monazite grains in garnet recording older ages than monazite grains in interpreted retrograde biotite. As discussed, these differences in ages could reflect a metamorphic event of prolonged duration, as opposed to closure temperature ages.

Fe-Mg thermobarometry performed on garnet cores show that temperatures of many garnet grains are lower than peak metamorphic conditions calculated from pseudosections, probably reflecting chemical resetting of the garnet grains during retrograde metamorphism. The relatively smooth shape of the garnet compositional profile confirms this. This may also explain why the calculated compositional contours on the pseudosection do not match the measured EMPA compositions (Hauzenberger *et al*. 2005). These results are consistent with Harley (1989) that discuss garnet being used as a geothermometer in granulites, as it only records the lower-*T* (retrograde) part of the thermal history due to resetting of the grain as *T* decreases.

Mineral grains can record the tectono-metamorphic and exhumation history of a metamorphic rock through chemically zoned profiles as a consequence of retrograde diffusion and is restricted to minerals that exhibit solid solution behaviour (Harley 1989; Florence & Spear 1995; Ganguly 2002; Hauzenberger *et al*. 2005; Robl *et al*. 2007; Vielzeuf *et al.* 2007). In the study of *P-T-t* paths in metamorphic rocks, garnet is the single most important mineral (Ganguly 2002; Storm & Spear 2005) as it is stable over a wide range of *P-T* conditions and partakes in cation exchange and discontinuous reactions with coexisting minerals. The integration of results using diffusional modelling software of Robl *et al*. (2007) is used to infer aspects of the exhumation history of granulites. However the diffusional zonation pattern in garnet is not a unique function of cooling rates or at the temperature interval at which cooling occurred, it is

also a function of grain size (Fernando *et al*. 2003; Hauzenberger *et al*. 2005; Robl *et al*. 2007; Caddick *et al*. 2010).

Cooling rates, estimated using measured garnet zoning profiles, coupled with monazite geochronology that spans at least 30 Ma can provide an explanation for the large differences in growth ages found in monazite grains in different textural locations. The two together strengthen the argument for slow cooling at elevated temperatures. Duration of metamorphism in this study was determined by the age difference between monazites found in various textural locations and modelling of preserved garnet diffusional profiles in the diffusion modelling code (Robl *et al*. 2007) to further indicate that Reynolds Range is a slow cooling terrane.

Williams *et al.* (1996) inferred a slow cooling rate in the Reynolds Range due to a weighted mean age difference (18.4 ± 0.8 Ma) between zircon and monazite in a single sample. A cooling rate in the Reynolds Range was constrained at ~3 °C Myr^{-1} for 26 My, calculated from the age difference between zircons (1594 ± 6 Ma; Williams *et al*. 1996) and monazites (Williams *et al*. 1996; Buick *et al*. 1998). Kelsey *et al*. (2008) determined the cooling rate to be ~4 °C Myr^{-1} based on zircon crystallisation at peak temperatures of ~800 °C with initiation of monazite growth once temperatures have cooled through to ~720 °C , and the differences between zircon and monazite ages. This study attributes the cooling rate to be ~4 °C Myr^{-1} based on the differences in peak temperature modelled in P-T pseudosections (~830 °C) with temperatures recorded in the garnet cores obtained from theromobarometry (~700 °C), and the difference in ages obtained from monazites in different textural locations (~29 M.y). Thermal modelling of garnet grains in this study suggest the duration of metamorphism to be between 20

and 50 M.y, consistent with the notion that the Reynolds Range is a slowly cooled terrane (Williams *et al*. 1996; Buick *et al*. 1998; Kelsey *et al*. 2008).

6.3 Potential mechanism of metamorphism

The driving mechanism(s) for low-pressure high-temperature metamorphism have been the subject of many studies (e.g. Chamberlain & Sonder 1990; De Yoreo *et al*. 1991; Hand *et al*. 1995; Williams *et al*. 1996; Sandiford & Hand 1998; McLaren *et al*. 1999) and the complexity of the tectonic conditions during the Proterozoic make these conditions difficult to interpret using a simple model (McLaren *et al*. 1999). Transient advection of heat due to magma ascent is often advocated as the cause of low-pressure high-temperature metamorphism (De Yoreo *et al*. 1991; Williams *et al*. 1996; Sandiford & Hand 1998; McLaren *et al*. 1999). However, in a number of Australian Proterozoic terranes the heat cause remains contentious due to LPHT metamorphism post-dating major magmatism by as much as 120 M.y. (Sandiford & Hand 1998; McLaren *et al*. 1999) because crustal heat generation rates are normally considered too low to promote heating. Williams *et al*. (1996) argues that it is increasingly clear that LPHT metamorphism is not always transient. In the Reynolds Range, if metamorphism at 1600 Ma was caused by rapid thermal pulses, such as those associated with emplacement of voluminous magmatism, then the numerous geochronological studies conducted in the region would show widespread metamorphic ages of *c*. 1820 and *c*. 1780 Ma that correspond to the age of voluminous magmatism.

A notable feature of Australian Proterozoic terranes is the elevated modern-day heat flow *c*. 85 mWm^{-2} (Sandiford & Hand 1998; McLaren et al. 1999), with anomalously high heat producing rates of ~5 – 10 μWm^{-3} from granitic gneisses. Sandiford and Hand

(1998) indicate that conduction from crustal heat production, responsible for modern-day heat flows, is concentrated at mid crustal levels (15 – 20 km) and can result in the conditions required for LPHT metamorphism, with only minor burial (*c*. 5 km) required to generate LPHT metamorphism. Several studies (Chamberlain & Sonder 1990; Buick *et al*. 1998; Sandiford & Hand 1998) suggest the unusual thermal regime to be connected to burial of a high-heat producing layer rather than emplacement of magmatism at this time. Chamberlain & Sonder (1990) argue that burial of such an anomalously high-heat producing layer could result in LPHT metamorphism that culminates in upper amphibolite to lower granulite facies conditions by thermal relaxation during compressional orogenesis. However as a consequence of this, Sandiford & Hand (1998) suggest that the terrane would remain at elevated temperatures for prolonged periods and would cool only after some decompression. Several studies (Sandiford & Hand 1998; Williams *et al*. 1996; Cartwright *et al*. 1999) suggest these explain the several features of the LPHT metamorphism seen in the Reynolds Range, including the shape of the retrograde *P-T* path and the prolonged duration of elevated temperatures, minimum ~30 Ma, with little change in pressure. Buick *et al*. (1998) suggest that the lateral temperature gradients recorded by metamorphic grades exposed at approximately the same crustal level in the Reynolds Range could perhaps be due to the burial of a layer of U- and Th- enriched granites, reflecting variations in the concentration of high-heat producing elements throughout the terrane, however the lack of detailed heat production data at that time made it difficult to test this hypothesis.

Heat production data collected in this study suggests the potential causal mechanism for sustaining long-lived metamorphism in the Reynolds Range could be due to the burial

of U- and Th- enriched crust, as granitic gneisses and metapelites in this study record modern-day heat production values between 8.91 and 24.90 μWm^{-3}, and metasediments record modern-day heat production values between 4.47 and 27.30 μWm^{-3}. Total crustal heat production at the time of metamorphism *ca*. 1580 Ma, are considerably higher (granitic gneisses – 11.04 to 45.37 μWm^{-3}; metasediments – 5.71 to 31.54 μWm^{-3}) and represent a minimum due to the contribution from the upper 10 – 20 km that has been subsequently removed from the metamorphic pile due to erosion (England & Thompson 1984; Buick *et al*. 1998; Sandiford & Hand 1998), resulting in a decrease in heat production of about 20 % over the last 1580 Ma (Chamberlain & Sonder 1990; Sandiford & Hand 1998). Chamberlain and Sonder (1990) suggest that within a metamorphic pile, anomalous heat production associated with granitic gneisses and/or metasediments provide a primary control on metamorphic grade in high grade terranes and in central Australia, granitic gneisses make up more than 60 % of the terrane (Buick *et al*. 1998; Sandiford & Hand 1998). Given what is known about the local area and more regionally, the burial of an enriched U- and Th- layer coupled with the compressional orogenic event at the time of metamorphism may be the cause of metamorphism in the Reynolds-Anmatjira Range region.

Evidence presented in this study show that the Reynolds Range experience LPHT metamorphism, and subsequent retrogression during *c.* 1573 to 1543 Ma at peak conditions of 840 °C and 7 kbars, with the occurrence of fine grained sillimanite at 650 °C and 3 kbars on a clockwise pressure-temperature evolution, suggesting the minimum duration of granulite-facies metamorphism in this region in the order of 30 M.y, with a cooling rate of ~4 °C Myr^{-1}. The average heat production (recalculated at 1580 Ma) of granitic gneisses, metasediments are 11.04 and 5.71 μWm^{-3}, suggesting the burial of an

enriched U- and Th- layer may be connected to metamorphism rather than emplacement of magmatism.

This study has advanced that of earlier studies (Clarke & Powell 1991, Williams et al. 1996; Vry et al. 1996; Rubatto et al. 2001; Rubatto et al. 2006) by doing an integrated study of the P-T-t evolution of the Reynolds Range.

7. ACKNOWLEDGMENTS

I am most sincerely thankful for the assistance, encouragement, support and precious time, given to me by the following people. My deepest gratitude goes to both of my supervisors, David Kelsey and Martin Hand, University of Adelaide, whom have been both inspiring and supportive throughout this whole process. Justin Payne, University of Adelaide, for help with LA-ICPMS. Kathryn Cutts, PhD student from the University of Adelaide for helping with THERMOCALC. A special thank you to Angus Netting and Benjamin Wade, from Adelaide Microscopy, for their technical support and late night phone calls. Andrew Barker, Geology Honours student of 2010, for help with heat production data and GRS support. And most importantly, Imogen Taylor, for being the most patient and understanding child for the last four years. This wouldn't have been possible without her support. And of course a special mention to the Geology Honours students of 2010 for the late night support and delirious good times.

8. REFERENCES

ALEINIKOFF J., SCHENCK W., PLANK M., SROGI L., FANNING C., KAMO S. & BOSBYSHELL H. 2006. Deciphering igneous and metamorphic events in high-grade rocks of the Wilmington Complex, Delaware: Morphology, cathodoluminescence and backscattered electron zoning, and SHRIMP U-Pb geochronology of zircon and monazite. *Geological Society of America Bulletin* **118**, 39-64.

BARKER, A. R 2010. The thermal properties, temperature structure and thermal evolution of the Eastern Ghats, India. University of Adelaide, BSc (Hons), unpublished (thesis).

BARTON M. D. & HANSON R. B. 1989. Magmatism and the development of low-pressure metamorphic belts: Implications from the western United States and thermal modelling. *Geological Society of America Bulletin* **101**, 1052-1065.

BETTS P., GILES D., LISTER G. & FRICK L. R. 2002. Evolution of the Australian lithosphere. *Australian Journal of Earth Sciences* **49,** 661-695.

BETTS P. & GILES D. 2006. The 1800 Ma – 1100 Ma tectonic evolution of Australia. *Precambrian Research* **144**, 92-126.

BOHLEN S. R. 1991. On the formation of granulites. *Journal of Metamorphic Geology* **9**, 223-229.

BROWN. M. 2002. Retrograde processes in migmatites and granulites revisited. *Journal of Metamorphic Geology* **20**, 25-40.

BUICK I. S., CARTWRIGHT I. & HARLEY S.L. 1998. The retrograde *P-T-t* path for low-pressure granulites from the Reynolds Range, central Australia: petrological constraints and implications for low-P/high-T metamorphism. *Journal of Metamorphic Geology* **16**, 511-529.

BUICK I. S., CARTWRIGHT I. & WILLIAMS I. S. 1997. High-temperature retrogression of granulite-facies marbles from the Reynolds Range Group, central Australia: phase equilibria, isotopic resetting and time-integrated fluid fluxes. *Journal of Petrology* **37**, 1097-1124.

BUICK I. S. FREI R. & CARTWRIGHT I. 1999. The timing of high-temperature retrogression in the Reynolds Range, central Australia: constraints from garnet and epidote Pb-Pb dating. *Contributions to Mineralogy and Petrology* **135**, 244-254.

CADDICK M. J., KONOPÁSEK J. & THOMPSON A. B. 2010. Preservation of garnet growth zoning and the duration of prograde metamorphism. *Journal of Petrology* **51**, 2327-2347.

CATLOS E. J., GILLEY L. D. & HARRISON M. D. 2002. Interpretation of monazite ages obtained via in situ analysis. *Chemical Geology* **188**, 193-215.

CARTWRIGHT I. & BUICK I. S. 1999. The low of surface-derived fluids through the Alice Springs age middle-crustal ductile shear zones, Reynolds Range, central Australia. *Journal of Metamorphic Geology* **17**, 397-414.

CARTWRIGHT I., BUICK I. S., FOSTER D. A. & LAMBERT D. D. 1999. Alice Springs age shear zones from the southeastern Reynolds Range, central Australia. *Australian Journal of Earth Sciences* **46**, 355 -363.

CHAMBERLAIN C. P. & SONDER L. J. 1990. Heat-producing elements and the thermal and baric patterns of metamorphic belts. *Science* **250**, 763-769

CHERNIAK D. J. & PYLE J. M. 2008. Th diffusion in monazite. *Chemical Geology* **256**, 52-61.

CHERNIAK D. J., WATSON E. B., GROVE M., & HARRISON T. M. 2004. Pb diffusion in monazite: A combined RBS/SIMS study. *Geochemica et Cosmochimica Acta* **68**, 829-840.

CLARKE C. & POWELL R. 1991. Proterozoic granulite facies metamorphism in the southeastern Reynolds Range, central Australia: geological context, *P-T* path and overprinting relationships. *Journal of Metamorphic Geology* **9**, 267-281.

COGGON R. & HOLLAND T.J.B. 2002. Mixing properties on phengitic micas and revised garnet-phengite thermobarometers. *Journal of Metamorphic Geology* **20**, 683-696.

COLLINS W. J. & SHAW R. D. 1995. Geochronological constraints on orogenic events in the Arunta Inlier; a review. *Precambrian Research* **71**, 315-346.

COLLINS W. J. & VERNON R. H. 1991. Orogeny associated with anticlockwise *P-T-t* paths: Evidence from low-*P*, high-*T* metamorphic terranes in the Arunta Inlier, central Australia. *Geology* **19**, 835-838.

COLLINS W. J. & WILLIAMS I. S. 1995. SHRIMP ion probe dating of short lived Proterozoic tectonic cycles in the northern Arunta Inlier, central Australia. *Precambrian Research* **71**, 69-89.

CUTTS K. HAND M. & KELSEY D. E. 2010. Evidence for early Mesoproterozoic (*ca.* 1590 Ma) ultrahigh-temperature metamorphism in southern Australia. *Lithos* (in press

DE YOREO J. J., LUX D.R. & GUIDOTTI C. V. 1991. Thermal modelling in low-pressure/high-temperature metamorphic belts. *Tectonophysics* **188**, 209-238.

DIRKS. P. H. G. M., HAND M. & POWELL R. 1991. The P-T-deformation path for a mid-Proterozoic, low-pressure terrane: the Reynolds Range, central Australia. *Journal of Metamorphic Geology* **9**, 641-661.

DODSON M. H. 1986. Closure profiles in cooling systems. *Materials Science Forum* **7**, 145-154.

ENGLAND P. C. & THOMPSON A. B. 1984. Pressure-Temperature-Time Paths of Regional Metamorphism I. Heat Transfer during the evolution of regions of thickened continental crust. *Journal of Petrology* **25**, 894-928.

FLORENCE F. P . & SPEAR F. S. 1995. Intergranular diffusion kinetics of Fe and Mg during retrograde metamorphism of a pelitic gneiss from the Adirondack Mountains. *Earth and Planetary Science Letters* **134**, 329-340.

FERNANDO G. W. A. R., HAUZENBERGER C. A., BAUMGARTNER L. P. & HOFMEISTER W. 2003. Modeling of retrograde diffusion zoning in garnet:

evidence for slow cooling of granulites from the Highland Complex of Sri Lanka. *Mineralogy and Petrology* **78,** 53-71.

GANGULY J. 2002. Diffusion kinetics in minerals: Principles and applications to tectono-metamorphic processes. *EMU Notes in Mineralogy* **4**, 271-309.

GANGULY J., CHENG W. & CHAKRABORTY S. 1998. Cation diffusion in aluminosilicate garnets: experimental determination in pyrope-almandine diffusion couples. *Contributions to Mineralogy and Petrology* **131**, 171-180.

GARDÉS E. & MONTEL J. M. 2009. Opening and resetting temperatures in heating geochronological systems. *Contributions to Mineralogy and Petrology* **158**, 185-195.

GILES D., BETTS P. & LISTER G. 2002. Far-field continental backarc setting for the 1.80 – 1.67 Ga basins of northeastern Australia. *Geological Society of America* **30**, 823-826.

GRASTY R. L. & MINTY B. R. S. 1995. A guide to the technical specifications for airborne gamma ray surveys. *Australian Geological Survey* **1995/60**.

HAND M. & BUICK I.S. 2001. Tectonic evolution of the Reynolds-Anmatjira Ranges: a case study in terrain reworking from the Arunta Inlier, central Australia. From: Miller J. A., Holdsworth. R. E., Buick I. S. & Hand M (eds) Continental reactivation and reworking. *Geological Society, London*, Special Publications **184**, 237-260.

HAND M., DIRKS P. H. G. M., POWELL R. & BUICK I. S. 1992. How well established is isobaric cooling in the Proterozoic orogenic belts? An example from the Arunta Inlier, central Australia. *Geology* **20**, 649-652.

HAND M., FANNING M., & SANDIFORD M. 1995. Low-*P* high-*T* metamorphism and the role of heat producing granites in the northern Arunta Inlier. *Geological Society of Australia Abstract* **40**, 60-61.

HARLEY S. L. 1989. The origins of granulites: a metamorphic perspective. *Geological Magazine* **126**, 215-247.

HAUZENBERGER C. A., ROBL J. & STÜWE K. 2005. Garnet zoning in high pressure granulite-facies metapelites, Mozambique belt, SE-Kenya: constraints on the cooling history. *European Journal of Mineralogy* **17**, 43-55.

HOLLAND T. J. B. & POWELL R. 1998. An internally consistent thermodynamic data set for phases of petrological interest. *Journal of Metamorphic Geology* **16**, 309-343.

HOLLAND T. J. B. & POWELL R. 2003. Activity–composition relations for phases in petrological calculations: an asymmetric multicomponent formulation. *Contributions to Mineralogy and Petrology* **145**, 492-501.

JACKSON S. E., PEARSON N. J., GRIFFIN W. L. & BELOUSOVA E. A. 2004. The application of laser ablation-inductively coupled plasma-mass spectrometry to in-situ U/Pb zircon geochronology. *Chemical Geology* **211**, 47-69.

KARLSTROM K. E., AHÄLL K., HARLAN S. S., WILLIAMS. M. L., MCLELLAND J. & GEISSMAN J. W. 2001. Long-lived (1.8 – 1.0 Ga) convergent orogen in

southern Laurentia , its extension to Australia and Baltica, and implications for refining Rodinia. *Precambrian Research* **111**, 5 -30.

KELSEY D. E. 2008. On ultra-high temperature crustal metamorphism. *Gondwana Research* **13**, 1-29.

KELSEY D. E., CLARK C. & HAND M. 2008. Thermobarometric modelling of zircon and monazite growth in melt-bearing systems: examples using model metapelitic and metapsammitic granulites. *Journal of Metamorphic Geology* **26**, 199-212.

KELSEY D. E., HAND M., CLARK C. & WILSON C. J. L. 2007. On the application of in situ monazite chemical geochronology to constraining *P-T-t* histories in high-temperature (>850 °C) polymetamorphic granulites from Prydz Bay, East Antarctica. *Journal of the Geological Society, London* **164**, 667-683.

KELSEY D. E., WHITE R. W. & POWELL R. 2003. Orthopyroxene-sillimanite-quartz assemblages: distribution, petrology, quantitative P-T-X constraints and P-T paths. *Journal of Metamorphic Geology* **21** 439-453.

LUDWIG K. R. 2003. User's Manual for Isoplot 3.00, Berkeley Geochronological Centre, Special Publication No.4, 71.

MCLAREN S., HAND M. & SANDIFORD M. 1999. High radiogenic heat-producing granites and metamorphism – An example from the western Mount Isa inlier, Australia. *Geology* **27**, 679-682.

PAYNE J. L., HAND M., BAROVICH K.M. & WADE B.P. 2008. Temporal constraints on the timing of high-grade metamorphism in the northern Gawler

Craton; implications for assembly of the Australian Proterozoic. *Australian Journal of Earth Sciences* **55**, 623-640.

PAYNE J. L., HAND M., BAROVICH K. M., REID A., & EVANS D. A. A. 2009. Correlations and reconstruction models for the 2500-1500 Ma evolution of the Mawson Continent. From: REDDY S. M., MAZUMDER R., EVANS D. A . D. & COLLINS A. S. (eds) Palaeoproterozoic Supercontinents and Global Evolution. *Geological Society, London, Special Publications* **323**, 319-355.

POWELL, R., HOLLAND, T., 1988. An internally consistent thermodynamic dataset with uncertainties and correlations: 3. Application methods, worked examples and a computer program. Journal of Metamorphic Geology 6, 173-204.

POWELL R., HOLLAND T. J. B. & WORLEY B. 1998. Calculating phase diagrams involving solid solutions via non-linear equations, with examples using THERMOCALC. *Journal of Metamorphic Geology* **16**, 577-588.

ROBL J., HERGARTEN S., STÜWE K., HAUZENBERGER C. 2007. THERMAL HISTORY: A new software to interpret diffusive zoning profiles in garnet. *Computers and Geoscience* **33**, 760-772.

RUBATTO D., HERMANN J. & BUICK I. S. 2006. Temperature and Bulk Composition Control of Growth of Monazite and Zircon During Low-Pressure Anatexis (Mount Stafford, Central Australia). *Journal of Petrology* **47**, 1973-1996.

RUBATTO D., WILLIAMS I.S. & BUICK I.S. 2001. Zircon and monazite response to prograde metamorphism in the Reynolds Range, central Australia. *Contributions to Mineralogy and Petrology* **140**, 458-468.

SANDIFORD M. & HAND M. 1998. Australian Proterozoic high-temperature, low-pressure metamorphism in the conductive limit. *In*: TRELOAR P. J. & O'BRIEN P. J (eds) What Drives Metamorphism and Metamorphic Reactions? *Geological Society, London, Special Publications* **138**, 109-120.

SANDIFORD M. & POWELL R. 1991. Some remarks on high temperature-low pressure metamorphism in convergent orogens. *Journal of Metamorphic Geology* **9**, 330-340.

SANDIFORD M., MARTIN N., ZHOU S. & FRASER G. 1991. Mechanical consequences of granite emplacement during high-T, low-P metamorphism and the origin of the "anticlockwise" *PT* paths. *Earth and Planetary Science Letters* **107**, 164-172.

SELWAY K, HAND M., HEINSON G. & PAYNE J. L. 2009. Magnetotelluric constraints on subduction polarity: Reversing reconstruction models for Proterozoic Australia. *Geology* **37**, 299-802.

SPEAR F.S. 1992. Thermobarometry and *P-T-t* paths from granulite facies rocks; an introduction. *Precambrian Research* **55**, 201-207.

SPEAR F. S. & PYLE M. P. 2010. Theoretical modeling of monazite growth in a low-Ca metapelite. *Chemical Geology* **273,** 111-119.

STORM L.C. & SPEAR F.S. 2005. Pressure, temperature and cooling rates of granulite facies migmatitic pelites from the southern Adirondack Highlands, New York. *Journal of Metamorphic Geology* **23**, 107-130.

SUN. S., WARREN R. G. & SHAW R. D. 1995. Nd isotope study of granites from the Arunta Inlier, central Australia; constraints on geological models and limitation of the method. *In*: Collins W. J. & Shaw R. D (Editors), Time limits on Tectonic Events and Crustal Evolution Using Geochronology; Some Australian Examples. *Precambrian Research* **71**, 301-314.

VERNON R.H. 1996. Problems with inferring *P-T-t* paths in low-*P* granulite facies rocks. *Journal of Metamorphic Geology* **14**, 143-153.

VIELZEUF D., BARONET A., PERCHIK A. L., LAPORTE D. & BAKER M. B. 2007. Calcium diffusivity in alumino-silicate garnets: an experimental and ATEM study. *Contributions to Mineralogy and Petrology* **154**, 153-179.

VRY J., COMPSTON W. & CARTWRIGHT I. 1996. SHRIMP II dating of zircons and monazites: reassessing the timing of high-grade metamorphism and fluid flow in the Reynolds Range, northern Arunta Block, Australia. *Journal of Metamorphic Geology* **14**, 335-350.

WADE B. P., BAROVICH K. M., HAND M., SCRIMGEOUR I. R. & CLOSE D. F. 2006. Evidence for Early Mesoproterozoic Arc Magmatism in the Musgrave Block, Central Australia; Implications for Proterozoic Crustal Growth and Tectonic Reconstructions of Australia. *Journal of Geology* **114**, 43-63.

WELLS P. R. A. 1980. Thermal models for magmatic accretion and subsequent metamorphism of continental crust. *Earth and Planetary Science Letters* **46**, 253-265.

WHITE R. W. & POWELL R. 2002. Melt loss and the preservation of granulite facies assemblages. *Journal of Metamorphic Geology* **20**, 621-632.

WHITE R. W., POWELL R., HOLLAND T. J. B. & WORLEY. 2000. The effect of TiO2 and Fe2O3 on metapelitic assemblages at greenschist and amphibolite facies conditions: mineral equilibria calculations in the system K2O–FeO–MgO–Al2O3–SiO2–H2O–TiO2–Fe2O3. *Journal of Metamorphic Geology* **18**, 497-511.

WHITE R.W., POWELL R. & CLARKE G.L. 2002. The interpretation of reaction textures in Fe-rich metapelitic granulites of the Musgrave Block, central Australia: constraints from mineral equilibria calculations in the system K2O-FeO-MgO-Al2O3-SiO2-H2O-TiO2-Fe2O3. *Journal of Metamorphic Geology* **20**, 41-55.

WHITE R.W., POWELL R. & HOLLAND T.J.B. 2007. Progress relating to calculation of partial melting equilibria for metapelites. *Journal of Metamorphic Geology* **25**, 511-527.

WILLIAMS I. S., BUICK I. S. & CARTWRIGHT I. 1996. An extended episode of early Mesoproterozoic metamorphic fluid flow in the Reynolds Range, central Australia. Journal of Metamorphic Geology 14, 29-47.

9. FIGURE CAPTIONS

Figure 1 A geological map of the Reynolds Range, central Australia, showing the distribution of major lithologies and shear structures. The range consists of two main rock groups: Reynolds Range Group (deposited 1812-1785 Ma) consisting of pelitic, quartzitic, and carbonatic metasediments, and the Lander Rock Beds (deposited 1840-1806 Ma) consisting of dominantly pelitic and psammitic metasediments, with voluminous magmatism occurring at about 1820 -1780 Ma). Map adapted from Hand & Buick 2001. Data sources: (1) Hand & Buick 2001; (2) Vry *et al*. 1996; (3) Williams *et al*. 1996; (4) Collins & Williams 1995; (5) Hand *et al*. 1995; (6) Sun *et al*. 1995.

Figure 2 Histogram of existing geochronological data in the Reynolds Range relevant to this study, indicating a spread of ages around 1600 Ma.

Figure 3 Photomicrographs of the analysed samples showing the microscopic mineral relationships. (a) Fine-grained sillimanite growing on the edges of garnet due to the breakdown of cordierite and biotite. (b) Fine-grained sillimanite on the boundaries where biotite and cordierite are in direct contact. (c) Breakdown of biotite in direct contact with garnet. (d) Breakdown of orthopyroxene in direct contact with biotite. (e) Fine-grained sillimanite growing on grain boundaries of cordierite. (f) Coarse-grained inclusions of sillimanite in garnet with fine-grained sillimanite growing due to the breakdown of biotite and cordierite. (g) Breakdown of biotite in direct contact with garnet and cordierite. (h) Coarse grained sillimanite inclusions in cordierite do not penetrate adjacent garnet. The breakdown of biotite is common on garnet grain boundaries. (i) Fine-grained sillimanite is common on cordierite grain boundaries. (j) Biotite inclusions in garnet have the same orientation as the biotite fabric that wraps

around the garnet grain. (k) Fine-grained sillimanite is common on boundaries of cordierite and biotite. (l) Coarse-grained sillimanite overgrowing biotite. Abbreviations in this and following figures: and, andalusite; bi, biotite; cd, cordierite; g, garnet; H2O, water; ilm, ilmenite; ksp, K-feldspar; liq, liquid; mt, magnetite; opx, orthopyroxene; pl, plagioclase; qtz, quartz; sill, sillimanite; sp, spinel.

Figure 4 Geological map of the Reynolds Range, central Australia, showing the distribution of samples used within this study.

Figure 5 (a) A slight increase of almandine and decrease of pyrope at the rim of the grains. (b) A minor decrease of almandine and increase of pyrope in the core and is otherwise a relatively flat profile. (c) An increase in almandine and a decrease in pyrope and a slight decrease in grossular from core to rim. (d) A slight increase of pyrope and decrease of almandine at the rim of the grain. (e) This profile shows no systematic variation between the core and the rim. (f) Zoning evident as the core is relatively flat with an increase of almandine and decrease of pyrope at the rim. (g) This profile shows no systematic variation between the core and the rim. (h) Shows a decrease in almandine and increase in pyrope at the rim of the grain.

Figure 6 Mineral chemistry proportions are given in selected fields in the following figures and represented by: X_{Fe} garnet – large spaced, dashed white line; X_{Ca} (Ca/(Ca+Fe+Mn+Mg) garnet – solid white line; X_{Fe} cordierite – small spaced, dashed black line; X_{Na} (Na/(K+Ca+Na) K-feldspar – solid black line; X_{Ca} (Ca/(K+Ca+Na) plagioclase – large spaced, dashed black line in pseudosections (a) to (f). The bold solid line indicates the interpreted peak conditions. The bold dashed line indicates where the fine-grained sillimanite commenced growth. Assemblage variance, v, is indicated in the field. The numbered list of mineral assemblages refers to the

numbered fields in the diagram. The white arrow indicates the interpreted P-T path for the sample. The *P-T* path is conveyed as wide rather than narrow to convey uncertainty.

Figure 7 Modal proportions of garnet, cordierite, sillimanite, K-feldpsar and plagioclase are given in selected fields in the following figures and represented by: garnet (Gt) – large spaced, dashed white line; cordierite (cd) – small spaced, dashed black line; K-feldspar (ksp) – solid black line; plagioclase (pl) – solid white line, and sillimanite (sill) - large spaced black line, in pseudosections (a) to (f). The bold solid line indicates the interpreted peak conditions. The bold dashed line indicates where the fine-grained sillimanite commenced growth. Assemblage variance, v, is indicated in the field. The numbered list of mineral assemblages refers to the numbered fields in the diagram. The white arrow indicates the interpreted *P-T* path for the sample. The *P-T* path is conveyed as wide rather than narrow to convey uncertainty.

Figure 8 Calculated *P-T* pseudosection for sample RR03. The bold solid line indicates the interpreted peak conditions. The bold dashed line indicates where the fine-grained sillimanite commenced growth. Assemblage variance, v, is indicated in the field. The numbered list of mineral assemblages refers to the numbered fields in the diagram. The white arrow indicates the interpreted P-T path for the sample. The *P-T* path is conveyed as wide rather than narrow to convey uncertainty.

Figure 9 Calculated *P-T* pseudosection for sample Boothby 09-2A. The bold solid line indicates the interpreted peak conditions. The bold dashed line indicates where the fine-grained sillimanite commenced growth. Assemblage variance, v, is indicated in the field. The numbered list of mineral assemblages refers to the numbered fields in the diagram. The white arrow indicates the interpreted P-T path for the sample. The *P-T* path is conveyed as wide rather than narrow to convey uncertainty.

Figure 10 Calculated *P-T* pseudosection for sample Boothby 09-2. The bold solid line indicates the interpreted peak conditions. The bold dashed line indicates where the fine-grained

sillimanite commenced growth. Assemblage variance, v, is indicated in the field. The numbered list of mineral assemblages refers to the numbered fields in the diagram. The white arrow indicates the interpreted P-T path for the sample. The *P-T* path is conveyed as wide rather than narrow to convey uncertainty.

Figure 11 Calculated *P-T* pseudosection for sample Boothby 09-4D. The bold solid line indicates the interpreted peak conditions. The bold dashed line indicates where the fine-grained sillimanite commenced growth. Assemblage variance, v, is indicated in the field. The numbered list of mineral assemblages refers to the numbered fields in the diagram. The white arrow indicates the interpreted P-T path for the sample. The *P-T* path is conveyed as wide rather than narrow to convey uncertainty.

Figure 12 Calculated *P-T* pseudosection for sample PH-05. The bold solid line indicates the interpreted peak conditions. The bold dashed line indicates where the fine-grained sillimanite commenced growth. Assemblage variance, v, is indicated in the field. The numbered list of mineral assemblages refers to the numbered fields in the diagram. The white arrow indicates the interpreted P-T path for the sample. The *P-T* path is conveyed as wide rather than narrow to convey uncertainty.

Figure 13 Calculated *P-T* pseudosection for sample RR2007-07. The bold solid line indicates the interpreted peak conditions. Assemblage variance, v, is indicated in the field. The numbered list of mineral assemblages refers to the numbered fields in the diagram. The white arrow indicates the interpreted P-T path for the sample. The *P-T* path is conveyed as wide rather than narrow to convey uncertainty.

Figure 14 In situ U-Pb monazite geochronology of sample RR04B. (a) Weighted average of 16 monazite analyses in orthopyroxene yield an age of 1573 ± 11 Ma. (b) Concordia plot of 16 monazite analyses within orthopyroxene. (c) Weighted average of

4 monazite analyses in retrogressed biotite yield an age of 1549 ± 21 Ma. (d) Concordia plot of 4 monazite analyses within retrogressed biotite. (e) BSE image of monazite within orthopyroxene. (f) BSE image on monazite within orthopyroxene. (g) BSE image showing textural location of monazite within retrogressed biotite.

Figure 15 In situ U-Pb monazite geochronology of sample RR051C. (a) Weighted average of 18 monazite analyses within biotite yield an age of 1543 ± 10 Ma. (b) Concordia plot of 18 monazite analyses within biotite. (c) Weighted average of 4 monazite analyses in the matrix yield an age of 1563 ± 23 Ma. (d) Concordia plot of 4 monazite analyses within the matrix. (e) BSE image of monazite within biotite. (f) BSE image showing the textural location of monazite within biotite. (g) BSE image of monazite within the matrix.

Figure 16 In situ U-Pb monazite geochronology of sample Boothby 09-2A. (a) Concordia plot of 11 monazite analyses within garnet. (b) Weighted average of 11 monazite analyses within garnet yield an age of 1573 ± 12 Ma. (c) to (f) BSE image of monazite within garnet.

Figure 17 In situ U-Pb monazite geochronology of sample Boothby 09-1. (a) Weighted average of 14 monazite analyses within biotite yield an age of 1544 ± 10 Ma. (b) Concordia plot of 14 monazite analyses within biotite. (c) Weighted average of 2 monazite analyses in the garnet yield an age of 1563 ± 28 Ma. (d) Concordia plot of 4 monazite analyses within the matrix. (e) BSE image of monazite within biotite. (f) BSE

image showing the textural location of monazite within biotite. (g) BSE image of monazite within the matrix.

Figure 18 Plot illustrating using different cooling regimes used to model measured garnet zoning profiles using diffusion modelling code of Robl *et al*. (2007). (a) Garnet profile of sample PH-05 modelled using X_{Mg} of 0.49, radius of 232.4 μm. Green curve: linear cooling with initial temperature of 830 °C and cooling rate of 1 °C/Ma. Red curve: linear cooling with initial temperature of 830 °C and cooling rate of 3 °C/Ma. Orange curve: linear cooling with initial temperature of 830 °C and cooling rate of 10 °C/Ma. Purple curve: linear cooling with initial temperature of 830 °C and cooling rate of 15 °C/Ma. Blue curve: linear cooling with initial temperature of 830 °C and cooling rate of 20 °C/Ma. Black dots: zoning profile measured using EPMA analyses. (b) Cooling rates determined using the same parameters as outlined in (a). Green curve: linear cooling with initial temperature of 830 °C and cooling rate of 1 °C/Ma. Red curve: linear cooling with initial temperature of 830 °C and cooling rate of 3 °C/Ma. Orange curve: linear cooling with initial temperature of 830 °C and cooling rate of 10 °C/Ma. Purple curve: linear cooling with initial temperature of 830 °C and cooling rate of 15 °C/Ma. Blue curve: linear cooling with initial temperature of 830 °C and cooling rate of 20 °C/Ma. (c) Garnet profile of sample RR2007-07 modelled using X_{Mg} of 0.42, radius of 1191.2 μm. Green curve: linear cooling with initial temperature of 800 °C and cooling rate of 1 °C/Ma. Red curve: linear cooling with initial temperature of 800 °C and cooling rate of 3 °C/Ma. Orange curve: linear cooling with initial temperature of 800 °C and cooling rate of 10 °C/Ma. Purple curve: linear cooling with initial temperature of 800 °C and cooling rate of 15 °C/Ma. Blue curve: linear cooling with

initial temperature of 800 °C and cooling rate of 20 °C/Ma. Black dots: zoning profile measured using EPMA analyses. (d) Cooling rates determined using the same parameters as outlined in (c) Green curve: linear cooling with initial temperature of 800 °C and cooling rate of 1 °C/Ma. Red curve: linear cooling with initial temperature of 800 °C and cooling rate of 3 °C/Ma. Orange curve: linear cooling with initial temperature of 800 °C and cooling rate of 10 °C/Ma. Purple curve: linear cooling with initial temperature of 800 °C and cooling rate of 15 °C/Ma. Blue curve: linear cooling with initial temperature of 800 °C and cooling rate of 20 °C/Ma.

10. TABLES

Table 1 Summary of existing geochronological data in the Reynolds Range relevant to this study

Age (Ma)	Method	Reference
1490	Rb-Sr muscovite	Collins & Shaw 1995
1820 1780-1770	U-Pb ionprobe analysis	Collins & Williams 1995
1566 - 1583	SHRIMP U-Pb zircon	Vry *et al*. 1996
1594 ± 6 1576 ± 6	SHRIMP U-Pb zircon SHRIMP U-Pb monazite	Williams *et al*. 1996
1544-1574	Pb stepwise leaching	Buick *et al*. 1999
1562 - 1587 1557 -1585	SHRIMP U-Pb zircon SHRIMP U-Pb monazite	Rubatto *et al*. 2001

Table 2 In situ U-Pb LA-ICPMS monazite data

		Ratios									Apparent Ages					
Analysis	*a* ^{204}Pbcps	^{207}Pb/^{206}Pb	1σ	^{207}Pb/^{235}U	1σ	^{206}Pb/^{238}U	1σ	*ρ*	*b* concordance	*Text. Loc.*	^{207}Pb/^{206}Pb	1σ	^{207}Pb/^{235}U	1σ	^{206}Pb/^{238}U	1σ
Sample RR04B																
spot 1	22	0.09733	0.00104	3.78554	0.05869	0.28179	0.00434	0.9934085	99	orthopyroxene	1573.6	19.82	1589.7	12.45	1600.4	21.8
spot 2	0	0.0972	0.00104	3.89054	0.06151	0.2898	0.00454	0.9908813	98	orthopyroxene	1571	19.95	1611.7	12.77	1640.5	22.67
spot 3	1	0.09553	0.00096	3.51749	0.0553	0.26639	0.00422	0.9924251	101	biotite	1538.5	18.84	1531.2	12.43	1522.5	21.47
spot 4	18	0.09754	0.00103	3.89605	0.06342	0.28872	0.00467	0.9936611	99	orthopyroxene	1577.7	19.61	1612.9	13.15	1635.1	23.36
spot 5	25	0.09774	0.00104	4.03529	0.06723	0.29818	0.00491	0.9883588	98	orthopyroxene	1581.4	19.87	1641.3	13.56	1682.3	24.4
spot 6	14	0.09758	0.00106	4.09374	0.06989	0.30271	0.00509	0.9849093	97	biotite	1578.3	20.2	1653.1	13.93	1704.8	25.16
spot 7	14	0.09705	0.00104	4.28735	0.07432	0.31844	0.00544	0.9854952	95	orthopyroxene	1568.1	20.01	1690.9	14.27	1782.1	26.61
spot 8	10	0.09675	0.00106	4.31093	0.07664	0.32081	0.00559	0.9801203	95	orthopyroxene	1562.4	20.38	1695.5	14.65	1793.7	27.3
spot 9	17	0.09738	0.00104	4.42578	0.07954	0.32685	0.0058	0.9873787	94	orthopyroxene	1574.6	19.77	1717.2	14.89	1823.1	28.16
spot 10	0	0.09762	0.00105	4.47376	0.08225	0.32918	0.00595	0.9831512	94	orthopyroxene	1579.1	19.9	1726.1	15.26	1834.4	28.88
spot 11	0	0.09716	0.00112	3.5325	0.05387	0.26231	0.00383	0.9574567	102	orthopyroxene	1570.2	21.39	1534.5	12.07	1501.6	19.54
spot 12	0	0.09615	0.00111	3.52193	0.05412	0.26462	0.00387	0.9517245	101	biotite	1550.7	21.59	1532.2	12.15	1513.4	19.75
spot 13	15	0.09656	0.00107	3.4964	0.05293	0.26194	0.00383	0.9658644	102	biotite	1558.8	20.73	1526.4	11.95	1499.7	19.57
spot 14	0	0.09714	0.00111	3.62202	0.05569	0.2701	0.00397	0.9559596	101	orthopyroxene	1569.9	21.19	1554.4	12.23	1541.3	20.17
spot 15	11	0.0978	0.00172	4.0054	0.0755	0.29744	0.00444	0.7919222	97	orthopyroxene	1582.5	32.63	1635.3	15.32	1678.6	22.08
spot 16	0	0.09787	0.00299	4.06665	0.1434	0.35351	0.0066	0.6205922	91	orthopyroxene	1584	56.14	1779	25.25	1951.3	31.43
spot 17	0	0.09725	0.00198	4.56079	0.08526	0.30291	0.00467	0.7342915	97	orthopyroxene	1572	37.64	1646.5	17.11	1705.7	23.09
spot18	4	0.09733	0.00204	3.76684	0.0809	0.2806	0.00433	0.7185035	99	orthopyroxene	1573.5	38.79	1585.7	17.23	1594.4	21.78
spot19	12	0.09684	0.00166	2.91844	0.05288	0.21836	0.00315	0.7961535	109	orthopyroxene	1564.1	31.87	1386.7	13.7	1273.2	16.68
spot 20	27	0.09625	0.00143	2.98915	0.04843	0.22488	0.00311	0.8535772	107	orthopyroxene	1552.7	27.68	1404.9	12.33	1307.6	16.38
spot 21*	18	0.10253	0.00168	3.74582	0.06485	0.26424	0.00368	0.8044262	105	orthopyroxene	1670.3	29.94	1581.2	13.88	1511.5	18.78
spot 22*	11	0.10894	0.0024	4.61438	0.10164	0.30615	0.00476	0.7058646	102	orthopyroxene	1781.7	39.63	1751.9	18.38	1721.7	23.5

Table 2 In situ U-Pb LA-ICPMS monazite data

		Ratios									Apparent Ages					
Analysis	*a* ^{204}Pbcps	^{207}Pb/^{206}Pb	1σ	^{207}Pb/^{235}U	1σ	^{206}Pb/^{238}U	1σ	*ρ*	*b* concordance	*Text. Loc.*	^{207}Pb/^{206}Pb	1σ	^{207}Pb/^{235}U	1σ	^{206}Pb/^{238}U	1σ
Sample RR051C																
spot 1	0	0.09566	0.00137	3.42369	0.06528	0.25956	0.00456	0.9213855	101	biotite	1541.1	26.6	1487.6	23.31	1509.8	14.98
spot 2	0	0.09602	0.00104	3.58353	0.06131	0.27069	0.00464	0.998101	100	biotite	1548.1	20.25	1544.3	23.55	1545.9	13.58
spot 3	9	0.09522	0.00104	3.52337	0.06064	0.2684	0.00462	0.9998653	100	biotite	1532.4	20.35	1532.7	23.49	1532.5	13.61
spot 4	5	0.09521	0.00104	3.44293	0.05945	0.26231	0.00453	0.9998626	101	biotite	1532.2	20.39	1501.6	23.12	1514.3	13.59
spot 5	0	0.09603	0.00108	3.53611	0.06187	0.2671	0.00463	0.9907242	101	biotite	1548.4	20.97	1526.1	23.56	1535.3	13.85
spot 6	12	0.09585	0.001	3.45146	0.05896	0.26122	0.00451	0.9894287	101	biotite	1544.7	19.4	1496.1	23.06	1516.2	13.45
spot 7	31	0.09579	0.00107	3.54016	0.06202	0.26811	0.00466	0.9921196	100	biotite	1543.6	20.77	1531.2	23.7	1536.2	13.87
spot 8	1	0.09609	0.00105	3.49055	0.06089	0.26351	0.00458	0.99636	101	matrix	1549.6	20.34	1507.8	23.39	1525.1	13.77
spot 9	17	0.09634	0.00135	3.50964	0.06812	0.26427	0.00474	0.9240988	101	matrix	1554.5	26.02	1511.6	24.19	1529.4	15.34
spot 10	2	0.09675	0.00111	3.57721	0.06426	0.26822	0.00473	0.9816885	101	matrix	1562.4	21.29	1531.7	24.05	1544.5	14.25
spot 12	19	0.09698	0.00128	3.64558	0.06943	0.2727	0.00489	0.9415496	100	matrix	1566.8	24.48	1554.5	24.79	1559.5	15.18
spot 13	0	0.09619	0.00155	3.33842	0.06994	0.25175	0.00464	0.8797593	103	biotite	1551.6	29.99	1447.5	23.88	1490.1	16.37
spot 14	10	0.09703	0.00122	3.56568	0.06693	0.26657	0.00478	0.9552965	101	biotite	1567.7	23.32	1523.4	24.33	1541.9	14.88
spot 15	15	0.09609	0.00122	3.45772	0.06528	0.26102	0.00469	0.951719	102	biotite	1549.4	23.58	1495.1	23.99	1517.6	14.87
spot 16	0	0.09611	0.00114	3.57375	0.05565	0.26904	0.00403	0.9619382	101	biotite	1549.9	22.11	1535.9	20.48	1543.7	12.35
spot 17	0	0.0951	0.00121	3.53544	0.05713	0.26899	0.00407	0.9363485	100	biotite	1530.1	23.78	1535.7	20.66	1535.2	12.79
spot 18	20	0.09558	0.00103	4.07281	0.06067	0.30833	0.00457	0.9949943	95	biotite	1539.5	20.18	1732.5	22.54	1648.9	12.14
spot 19	0	0.09578	0.0011	3.4669	0.05318	0.26189	0.00391	0.9733092	101	biotite	1543.5	21.47	1499.5	19.98	1519.7	12.09
spot 20	0	0.09538	0.00113	3.5963	0.05609	0.27282	0.00409	0.9612084	100	biotite	1535.6	22.22	1555.1	20.72	1548.7	12.39
spot 21	0	0.09528	0.00118	3.61248	0.05763	0.27434	0.00414	0.9459497	99	biotite	1533.6	23.21	1562.8	20.92	1552.3	12.69
spot 22	0	0.09616	0.00123	3.31943	0.05371	0.24977	0.00378	0.9353193	103	biotite	1550.9	23.8	1437.3	19.49	1485.6	12.63
spot 23	12	0.09626	0.00111	3.44797	0.05287	0.25916	0.00387	0.9738614	102	biotite	1552.9	21.43	1485.5	19.81	1515.4	12.07
spot 24*	6	0.09391	0.00098	3.69901	0.05413	0.285	0.00421	0.9906387	97	biotite	1506.3	19.49	1616.5	21.12	1571.2	11.7

Table 2 In situ U-Pb LA-ICMPS monazite data

Analysis	*a* ^{204}Pbcps	Ratios ^{207}Pb/^{206}Pb	1σ	^{207}Pb/^{235}U	1σ	^{206}Pb/^{238}U	1σ	ρ	*b* concordance	*Text. Loc.*	Apparent Ages ^{207}Pb/^{206}Pb	1σ	^{207}Pb/^{235}U	1σ	^{206}Pb/^{238}U	1σ
Sample Boothby 09-2A																
spot 1	9	0.09773	0.00101	3.5953	0.05322	0.26674	0.004	0.9871153	102	garnet	1581.3	19.27	1548.5	11.76	1524.2	20.34
spot 2	0	0.09673	0.00113	5.39655	0.08459	0.40453	0.00615	0.9698879	86	garnet	1561.9	21.79	1884.3	13.43	2189.9	28.24
spot 3	0	0.09739	0.00101	3.75322	0.05562	0.27941	0.00419	0.9882228	100	garnet	1574.7	19.25	1582.8	11.88	1588.4	21.13
spot 4	0	0.09767	0.00107	4.649	0.07064	0.34508	0.00521	0.9936348	92	garnet	1580.2	20.3	1758.1	12.7	1911.1	24.99
spot 5	0	0.09667	0.00095	3.68354	0.05362	0.27624	0.00414	0.9712872	100	garnet	1560.9	18.36	1567.8	11.62	1572.4	20.89
spot 6	0	0.09734	0.00106	3.70026	0.05612	0.27557	0.00417	0.997743	100	garnet	1573.8	20.16	1571.4	12.12	1569	21.06
spot 7	0	0.09761	0.00105	3.60302	0.05455	0.26758	0.00405	0.9997083	101	garnet	1578.9	20.02	1550.2	12.03	1528.5	20.59
spot 8	11	0.09725	0.00104	3.6617	0.05525	0.27294	0.00413	0.9971642	100	garnet	1572	19.84	1563.1	12.03	1555.7	20.91
spot 9	0	0.09737	0.00103	3.62645	0.05457	0.26997	0.00408	0.9956979	101	garnet	1574.3	19.66	1555.4	11.98	1540.6	20.73
spot 10	7	0.09739	0.00098	3.81416	0.05649	0.28379	0.0043	0.9774652	99	garnet	1574.7	18.63	1595.7	11.91	1610.4	21.58
spot 11	1	0.0974	0.00112	4.08049	0.06409	0.30355	0.00466	0.9774121	97	garnet	1575	21.3	1650.4	12.81	1708.9	23.06
Sample Boothby 09-1																
spot 1	7	0.09604	0.00097	3.68195	0.05617	0.27804	0.0043	0.9864279	99	biotite	1548.5	18.95	1567.5	12.18	1581.5	21.69
spot 2	7	0.09606	0.00099	3.77116	0.05766	0.28473	0.0044	0.989419	98	biotite	1548.9	19.18	1586.6	12.27	1615.1	22.08
spot 3	19	0.09634	0.00111	4.03065	0.0645	0.30343	0.00473	0.9741324	96	biotite	1554.4	21.46	1640.4	13.02	1708.3	23.42
spot 5	11	0.09602	0.00097	3.94542	0.0583	0.29799	0.00451	0.9763386	97	biotite	1548.2	18.95	1623.1	11.97	1681.4	22.39
spot 6	11	0.0958	0.00102	3.63316	0.05461	0.27505	0.00417	0.9914327	99	biotite	1543.8	19.85	1556.8	11.97	1566.4	21.09
spot 7	0	0.09567	0.00098	3.63402	0.05355	0.27547	0.00416	0.9757828	99	biotite	1541.3	19.06	1557	11.73	1568.5	21
spot 8	3	0.09594	0.00104	3.48642	0.04812	0.26391	0.00363	0.9965632	101	biotite	1546.6	20.14	1524.1	10.89	1509.8	18.49
spot 9	0	0.09468	0.00101	3.60844	0.04966	0.27676	0.00381	0.9996905	99	biotite	1521.8	19.97	1551.4	10.94	1575	19.22
spot 10	0	0.09548	0.00096	3.43995	0.04605	0.26162	0.00358	0.9782851	101	biotite	1537.6	18.76	1513.6	10.53	1498.1	18.31
spot 11	0	0.09589	0.00107	3.56583	0.05048	0.27004	0.00375	0.9809445	100	biotite	1545.6	20.76	1542	11.23	1541	19.05
spot 12	15	0.09645	0.0011	3.17815	0.04589	0.23924	0.00335	0.9697669	105	garnet	1556.6	21.29	1451.9	11.15	1382.7	17.44
spot 13	0	0.09576	0.00098	3.48482	0.04778	0.26421	0.00367	0.9870723	101	biotite	1543.1	19.17	1523.8	10.82	1511.3	18.69
spot 14	0	0.0963	0.00113	3.67948	0.05415	0.27739	0.00392	0.9602476	99	biotite	1553.6	21.81	1566.9	11.75	1578.2	19.79
spot 15	7	0.09701	0.00099	3.78533	0.05208	0.28325	0.00395	0.9865976	99	garnet	1567.5	18.99	1589.6	11.05	1607.7	19.83
spot 16	3	0.09625	0.001	3.56937	0.04982	0.26918	0.00377	0.9965833	100	biotite	1552.7	19.47	1542.7	11.07	1536.6	19.16
spot 17	1	0.0957	0.00103	3.54578	0.05031	0.26891	0.00379	0.9933212	100	biotite	1541.9	20.03	1537.5	11.24	1535.3	19.25

a - background subtracted

b - concordance = ^{206}Pb/^{238}U ÷ ^{207}Pb/^{206}Pb * 100

* - discounted from weighted average

Table 3 Representative microprobe analysis of garnet from all samples.

	PH-05 core	Boothby 09-1 core	Boothby 09-2A rim	Boothby 09-2 rim	RR03 core	RR04B rim	Boothby 09-4D rim	RR2007-07 rim
SiO2	36.28	35.94	37.35	36.07	36.34	37.10	37.70	35.98
TiO2	0.03	0.06	0.00	0.05	0.00	0.03	0.00	0.01
Al2O3	21.11	20.73	20.89	21.05	21.43	21.56	21.36	21.05
Cr2O3	0.00	0.00	0.03	0.06	0.04	0.01	0.00	0.02
FeO	34.08	34.87	34.29	36.94	32.10	30.21	35.51	36.40
MnO	0.66	0.70	0.71	0.46	0.43	0.45	0.46	0.32
MgO	5.58	4.73	4.72	3.83	7.13	8.47	3.82	4.00
ZnO	0.14	0.00	0.04	0.03	0.00	0.06	0.00	0.03
CaO	0.95	1.25	1.47	1.04	0.98	1.23	1.03	0.53
Na2O	0.03	0.01	0.00	0.02	0.03	0.03	0.03	0.04
K2O	0.00	0.00	0.00	0.02	0.01	0.00	0.02	0.01
Total	98.87	98.31	99.49	99.57	98.49	99.42	99.92	98.38
No. Oxygens	12.00	12.00	12.00	12.00	12.00	12.00	12.00	12.00
Si	2.93	2.94	3.00	1.20	2.92	2.93	3.01	2.95
Ti	0.00	0.00	0.00	0.00	0.00	0.00	0.00	0.00
Al	2.01	2.00	1.97	0.62	2.03	2.00	2.01	2.03
Cr	0.00	0.00	0.00	0.00	0.00	0.00	0.00	0.00
Fe2+	2.30	2.38	2.30	0.51	2.15	1.99	2.37	2.49
Mn	0.05	0.05	0.05	0.01	0.03	0.03	0.03	0.02
Mg	0.67	0.58	0.56	0.09	0.85	1.00	0.46	0.49
Zn	0.01	0.00	0.00	0.00	0.00	0.00	0.00	0.00
Ca	0.08	0.11	0.13	0.02	0.08	0.10	0.09	0.05
Na	0.00	0.00	0.00	0.00	0.01	0.00	0.00	0.01
K	0.00	0.00	0.00	0.00	0.00	0.00	0.00	0.00
Total Cations	8.06	8.06	8.02	2.46	8.07	8.07	7.98	8.04
Xalm	0.74	0.76	0.76	0.81	0.69	0.64	0.81	0.82
Xpy	0.22	0.18	0.19	0.15	0.27	0.32	0.15	0.16
Xgr	0.03	0.04	0.04	0.03	0.03	0.03	0.03	0.02
Xsps	0.01	0.02	0.02	0.01	0.01	0.01	0.01	0.01
XFe*	0.77	0.81	0.80	0.84	0.72	0.67	0.84	0.84

XFe* = $(Fe^{2+}/Fe^{2+}+Mg)$

Table 4. Representative microprobe analysis of biotite from all analysed samples

	Boothby 09-4D		Boothby 09-1		Boothby 09-2A		PH-05		RR03		Boothby 09-2	
							biotite 1	biotite 2				
SiO2	33.41	34.19	34.46	34.46	34.46	34.46	34.16	35.13	34.21	34.48	33.80	34.66
TiO2	3.97	2.78	3.14	3.18	3.14	3.18	3.80	0.05	3.68	4.14	4.00	4.40
Al2O3	16.65	17.44	16.04	16.04	16.04	16.04	16.40	19.32	15.63	15.71	14.91	15.88
Cr2O3	0.08	0.04	0.02	0.00	0.02	0.00	0.26	0.00	0.00	0.01	0.11	0.03
FeO	23.11	21.98	18.97	19.98	18.97	19.98	13.12	17.11	14.60	14.52	15.94	18.12
MnO	0.01	0.05	0.00	0.00	0.00	0.00	0.04	0.03	0.00	0.00	0.05	0.07
MgO	8.05	9.48	10.62	10.31	10.62	10.31	14.06	12.89	13.66	14.13	11.92	11.83
ZnO	0.17	0.00	0.08	0.00	0.08	0.00	0.00	0.00	0.00	0.07	0.08	0.00
CaO	0.00	0.00	0.00	0.03	0.00	0.03	0.01	0.00	0.00	0.00	0.01	0.00
Na2O	0.11	0.12	0.21	0.22	0.21	0.22	0.18	0.19	0.15	0.16	0.08	0.07
K2O	9.40	9.70	9.44	9.34	9.44	9.34	9.73	9.57	9.58	9.69	9.21	9.70
Total	94.96	95.81	92.98	93.56	92.98	93.56	91.76	94.29	91.59	92.95	90.13	94.77
Si	2.63	2.64	2.71	2.70	2.71	2.70	2.65	2.68	2.68	2.66	2.71	2.66
Ti	0.23	0.16	0.19	0.19	0.19	0.19	0.22	0.00	0.22	0.24	0.24	0.25
Al	1.54	1.59	1.49	1.48	1.49	1.48	1.50	1.74	1.44	1.43	1.41	1.44
Cr	0.00	0.00	0.00	0.00	0.00	0.00	0.02	0.00	0.00	0.00	0.01	0.00
Fe2+	1.52	1.42	1.25	1.31	1.25	1.31	0.85	1.09	0.96	0.94	1.07	1.16
Mn2+	0.00	0.00	0.00	0.00	0.00	0.00	0.00	0.00	0.00	0.00	0.00	0.00
Mg	0.94	1.09	1.24	1.20	1.24	1.20	1.63	1.46	1.59	1.62	1.42	1.36
Zn	0.01	0.00	0.00	0.00	0.00	0.00	0.00	0.00	0.00	0.00	0.00	0.00
Ca	0.00	0.00	0.00	0.00	0.00	0.00	0.00	0.00	0.00	0.00	0.00	0.00
Na	0.02	0.02	0.03	0.03	0.03	0.03	0.03	0.03	0.02	0.02	0.01	0.01
K	0.94	0.96	0.95	0.93	0.95	0.93	0.96	0.93	0.96	0.95	0.94	0.95
Total Cations	7.84	7.89	7.85	7.85	7.85	7.85	7.86	7.93	7.87	7.87	7.82	7.84
XMg (Mg/(Fe+Mg)	0.38	0.43	0.50	0.48	0.50	0.48	0.66	0.57	0.63	0.63	0.57	0.54

Table 5. Representative microprobe analysis of all mineral s

	RR04B	RR04B	RR04B	PH-05	PH-05	PH-05	Boothby 09-1	Boothby 09-4D	Boothby 09-2	RR03	RR2007-07	Boothby 09-2A	Boothby 09-2A
	opx rim	opx core	pl	sp	bi (apple green)	sill	bi	ksp	crd	crd	ilm	and	mt
SiO2	45.54	45.84	58.92	0.00	35.13	35.27	35.16	62.87	44.10	48.05	0.00	36.84	0.07
TiO2	0.20	0.16	0.02	0.03	0.05	0.01	3.18	0.04	0.00	0.00	51.76	0.02	0.11
Al2O3	7.15	7.19	24.97	56.82	19.32	61.38	16.27	18.02	31.40	32.78	0.00	58.84	0.38
Cr2O3	0.00	0.00	0.02	0.61	0.00	0.05	0.01	0.08	0.04	0.00	0.04	0.07	0.84
FeO	25.75	26.62	0.01	26.80	17.11	0.50	19.66	0.03	22.98	4.65	45.31	2.13	86.87
MnO	0.08	0.18	0.01	0.04	0.03	0.02	0.03	0.00	0.00	0.03	0.09	0.05	0.00
MgO	19.11	18.33	0.00	4.28	12.89	0.00	10.65	0.03	1.47	11.23	0.21	0.61	0.01
ZnO	0.05	0.09	0.00	9.45	0.00	0.00	0.11	0.06	0.03	0.07	0.00	0.03	0.00
CaO	0.11	0.14	7.25	0.02	0.00	0.00	0.05	0.05	0.01	0.04	0.01	0.05	0.03
Na2O	0.03	0.01	7.53	0.33	0.19	0.00	0.21	1.74	0.03	0.00	0.04	0.07	0.00
K2O	0.02	0.00	0.15	0.00	9.57	0.00	9.31	14.34	0.01	0.00	0.00	0.09	0.02
Total	98.19	98.74	98.88	98.40	94.29	97.26	94.64	97.27	100.07	96.85	97.45	98.81	88.40
Si	1.74	1.75	2.66	0.00	2.68	0.98	2.71	2.98	4.97	4.95	0.00	1.01	0.00
Ti	0.01	0.00	0.00	0.00	0.00	0.00	0.18	0.00	0.00	0.00	1.30	0.00	0.00
Al	0.32	0.32	1.33	1.93	1.74	2.01	1.48	1.01	3.97	3.98	0.00	1.90	0.02
Cr	0.00	0.00	0.00	0.01	0.00	0.00	0.00	0.00	0.00	0.00	0.00	0.00	0.03
Fe3+	0.18	0.16	-	0.07	-	0.00	-	-	-	-	-0.01	0.00	1.94
Fe2+	0.64	0.69	0.00	0.58	1.09	0.01	1.27	0.00	0.94	0.40	0.64	0.05	1.00
Mn	0.00	0.01	0.00	0.00	0.00	0.00	0.00	0.00	0.00	0.00	0.00	0.00	0.00
Mg	1.09	1.05	0.00	0.18	1.46	0.00	1.23	0.00	1.16	1.72	0.01	0.03	0.00
Zn	0.00	0.00	0.00	0.20	0.00	0.00	0.01	0.00	0.00	0.01	0.00	0.00	0.00
Ca	0.00	0.01	0.35	0.00	0.00	0.00	0.00	0.00	0.00	0.00	0.00	0.00	0.00
Na	0.00	0.00	0.66	0.02	0.03	0.00	0.03	0.16	0.01	0.00	0.00	0.00	0.00
K	0.00	0.00	0.01	0.00	0.93	0.00	0.92	0.87	0.00	0.00	0.00	0.00	0.00
Total	4.00	4.00	2.01	3.03	7.93	3.01	7.83	5.03	11.05	11.06	1.93	3.02	3.00
XFe*	0.43	0.45	0.93	0.78	0.43	0.98	0.51	0.37	0.39	0.19	0.99	0.66	1.00
XMg	0.57	0.55	0.07	0.22	0.57	0.02	0.49	0.63	0.61	0.81	0.01	0.34	0.00

XFe* = Fe/(Fe+Mg)
XMg = Mg/(Fe+Mg)

Table 6. Summary of *P-T* pseudosections subdivided into locations. Minerals = Peak *P-T* estimate in kbar and ˚C, and Retrograde *P-T* estimates in kbar and ˚C.

Label	Location	Peak Assemblage	Retrograde Assemblage	Peak (P kbar, T °C)	Retrograde (P kbar, T °C)
RR03	Gas Pipeline Locality	gt+cd+pl+ksp+bi+ilm+qtz	mt inclusions in ilm	7 ± 0.5, 840 ± 20	3 ± 0.5, 650 ± 10
Boothby 09-2	North of Mt. Boothby	gt+cd+ksp+bi+qtz+ilm	fine-grained and, increase in pl	5.5 ± 0.5, 830 ± 20	2.7 ± 0.4, 650 ±20
Boothby 09-2A	North of Mt. Boothby	gt+cd+ksp+qtz+ilm±bi	fine-grained and	5.5 ± 0.5, 830 ± 20	3.4 ± 0.2, 630 ± 20
Boothby 09-4D	East of Mt. Boothby	gt+cd+sill +qtz+ksp+ilm	fine-grained sill ± bi	5.8 ± 0.4, 850 ± 40	3.8 ± 0.3, 680 ± 30
PH-05	Peaked Hill	gt+cd+sill+qtz+ksp+pl+ilm±bi	fine-grained sillimanite ± bi	6 ± 0.5, 830 ± 20	3.5 ± 0.5, 700 ± 50
RR2007-07	N-W of Mt. Boothby	gt+bi+cd+sill+ksp+qtz+ilm	fine-grained sillimanite	6.5 ± 0.5, 860 ± 30	4 ± 0.5, 730 ± 30

Table 7 Pressure Temperature estimates calculated from end member reactions using THERMOCALC, mode 3.

Sample Boothby 09-1

P (kbars)	4.0	4.4	4.8	5.2	5.6	6.0	6.4	6.8	7.2	7.6	8.0
T (°C)	677	679	681	683	685	687	689	691	693	695	697

Sample Boothby 09-2

P (kbars)	5.0	5.4	5.8	6.2	6.6	7.0	7.4	7.8	8.2	8.6	9.0
T (°C)	735	737	739	741	743	745	748	750	752	754	756

Sample Boothby 09-2A

P (kbars)	5.0	5.4	5.8	6.2	6.6	7.0	7.4	7.8	8.2	8.6	9.0
T (°C)	655	657	659	661	663	665	667	669	671	673	675

Sample Boothby 09-4D

P (kbars)	5.0	5.4	5.8	6.2	6.6	7.0	7.4	7.8	8.2	8.6	9.0
T (°C)	792	794	796	799	801	803	805	808	810	812	815

Sample PH-05

P (kbars)	5.0	5.4	5.8	6.2	6.6	7.0	7.4	7.8	8.2	8.6	9.0
T (°C)	643	645	647	649	651	653	655	657	659	661	663

Sample RR03

P (kbars)	5.0	5.4	5.8	6.2	6.6	7.0	7.4	7.8	8.2	8.6	9.0
T (°C)	741	744	746	748	750	752	755	757	759	761	763

Sample RR04B

P (kbars)	4.0	4.5	5.0	5.5	6.0	6.5	7.0	7.5	8.0	8.5	9.0
T (°C)	666	672	677	683	688	694	700	705	711	717	722

Sample RR2007-07

P (kbars)	5.0	5.4	5.8	6.2	6.6	7.0	7.4	7.8	8.2	8.6	9.0
T (°C)	794	796	799	801	803	806	808	810	813	815	817

Table 8. Geochemistry and heat production, Reynolds Range

Lithology		K_%	Th_ppm	U_ppm	Q (μ Wm^{-3})	Q^* (μ Wm^{-3})
Interlayered Mafic and Felsic Gneiss (32)	Average	3.67	22.15	10.28	4.04	5.76
	Minimum	1.40	4.40	2.10	0.40	1.45
	Maximum	5.80	68.80	26.00	10.60	13.87
Granitic Rocks (155)	Average	4.27	65.73	15.89	8.91	11.04
	Minimum	1.10	5.00	2.30	0.40	1.45
	Maximum	6.10	152.60	43.90	24.90	45.37
Metasediments (177)	Average	2.70	34.58	7.78	4.47	5.71
	Minimum	0.06	2.40	1.67	0.90	0.99
	Maximum	5.60	272.80	31.60	27.30	31.54

Q = present heat production; Q^* = heat production at time of peak metamorphism (ca. 1580 Ma).

The number in parenthesis is the number analysed.

11. FIGURES

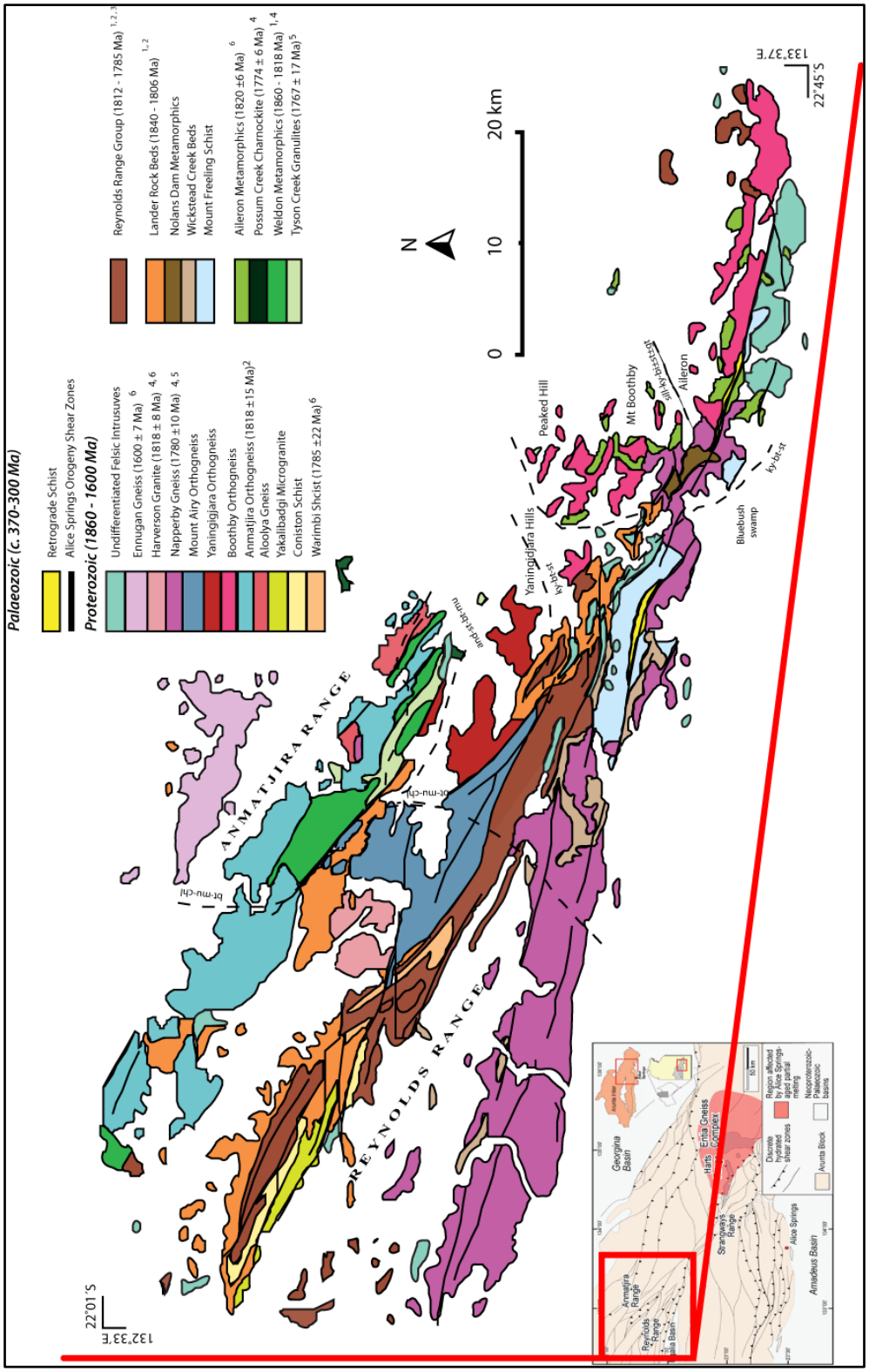

Figure 1

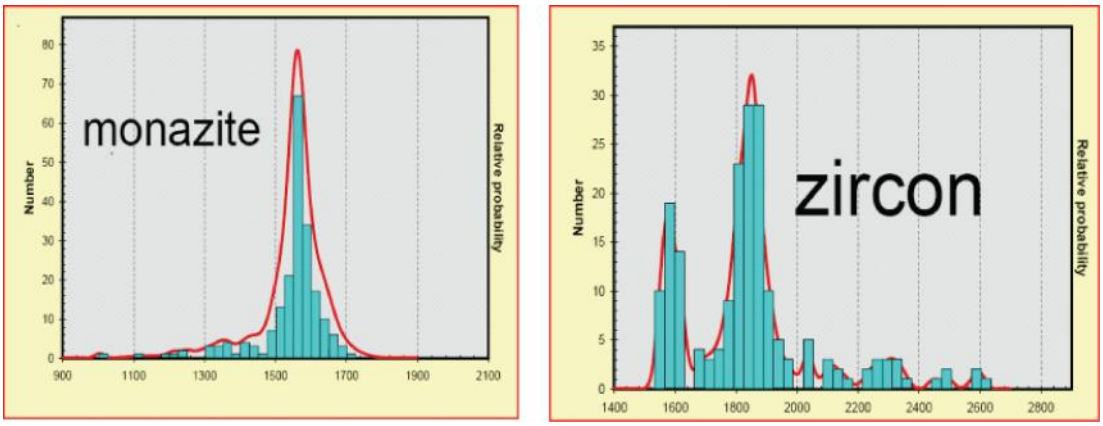
monazite
Number
Relative probability
0
10
20
30
40
50
60
70
80
900
1100
1300
1500
1700
1900
2100
zircon
Number
Relative probability
0
5
10
15
20
25
30
35
1400
1600
1800
2000
2200
2400
2600
2800

Figure 2

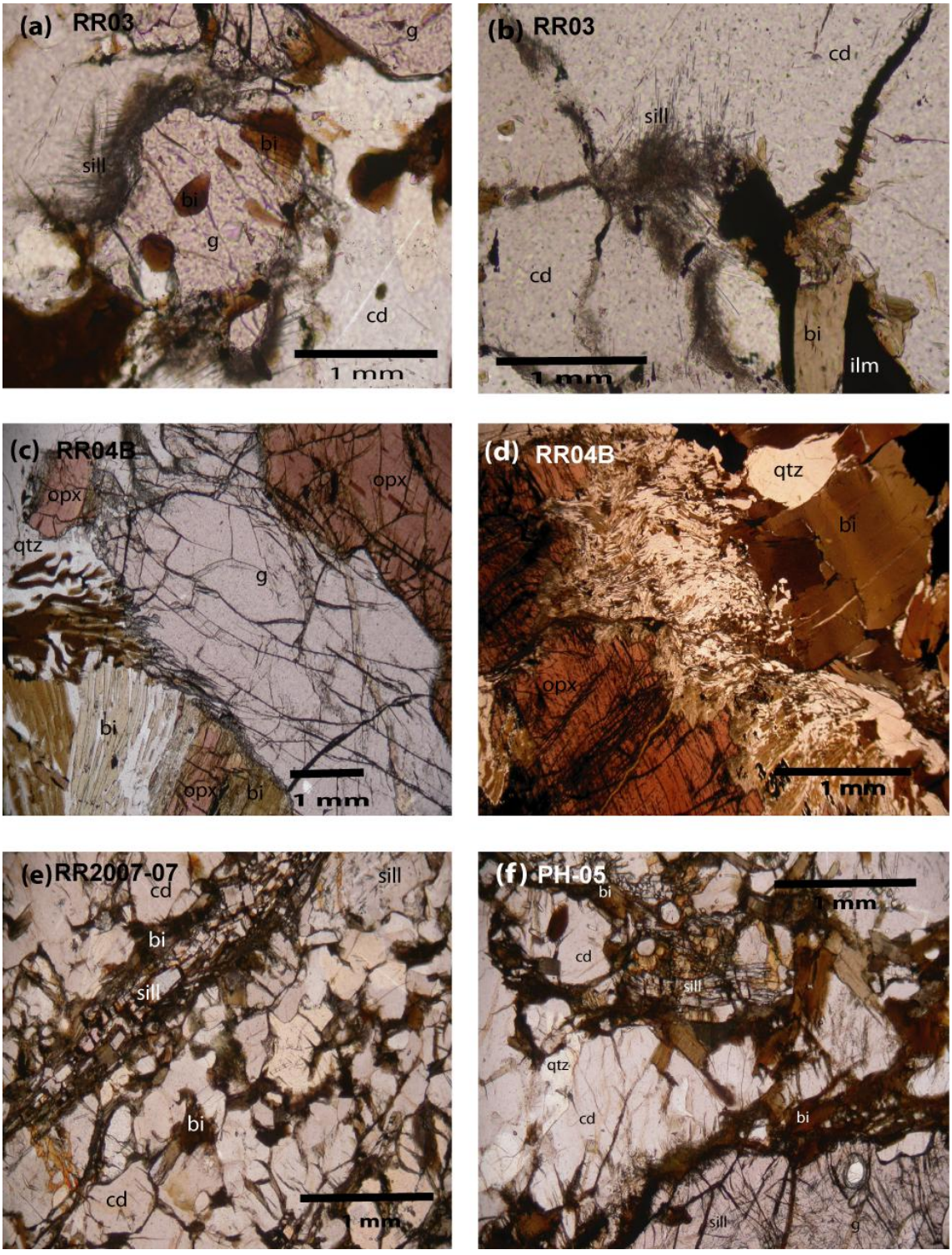
(a) RR03
g
sill
bi
bi
g
cd
1 mm
(b) RR03
cd
sill
cd
bi
ilm
1 mm
(c) RR04B
opx
opx
qtz
g
bi
opx
bi
1 mm
(d) RR04B
qtz
bi
opx
1 mm
(e) RR2007-07
sill
cd
bi
sill
bi
cd
mm
(f) PH-05
bi
1 mm
cd
sill
qtz
cd
bi
sill
g

Figure 3

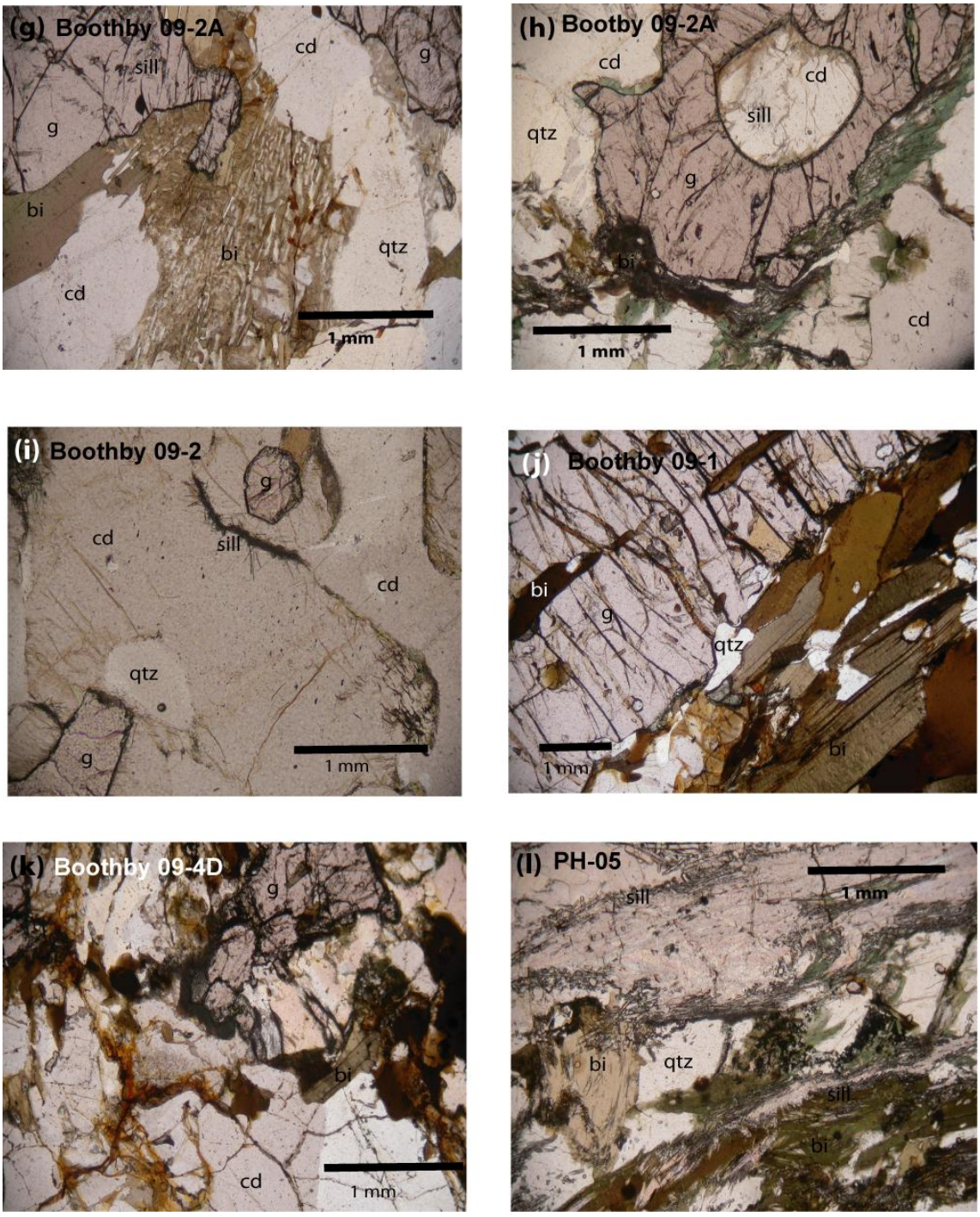

Figure 3 continued

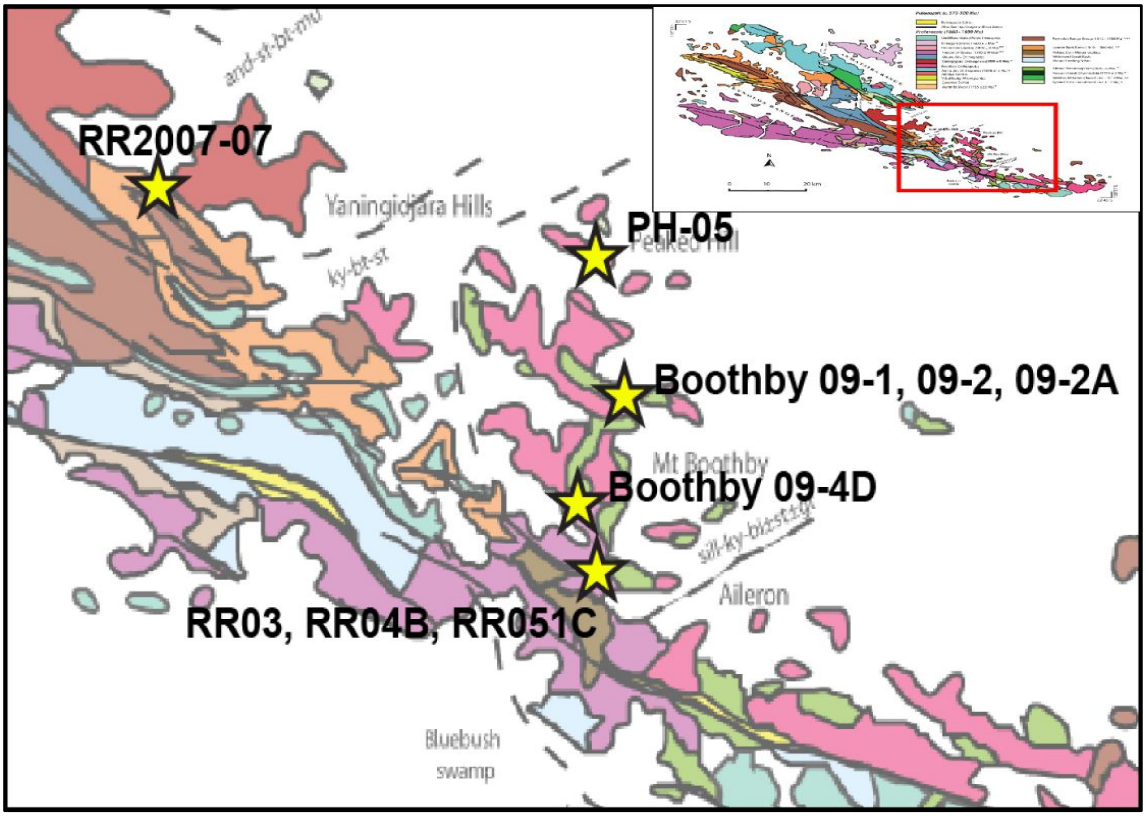
and-st-bt-mu
RR2007-07
Yaningidjara Hills
ky-bt-st
PH-05
Peaked Hill
Boothby 09-1, 09-2, 09-2A
Mt Boothby
Boothby 09-4D
sill-ky-blastite
Aileron
RR03, RR04B, RR051C
Bluebush
swamp

Figure 4

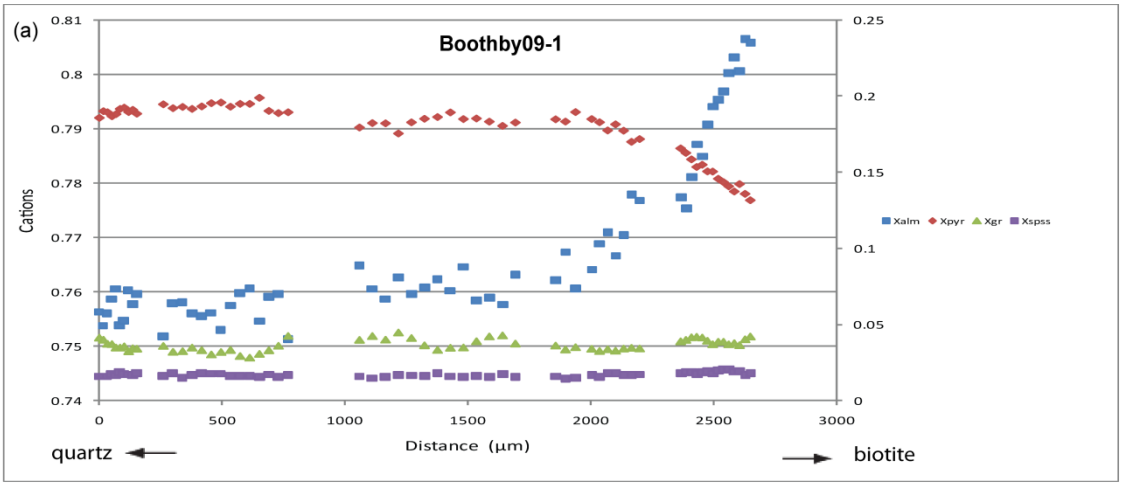
(a)
Boothby09-1
Cations
Distance (µm)
quartz
biotite
Xalm
Xpyr
Xgr
Xspss

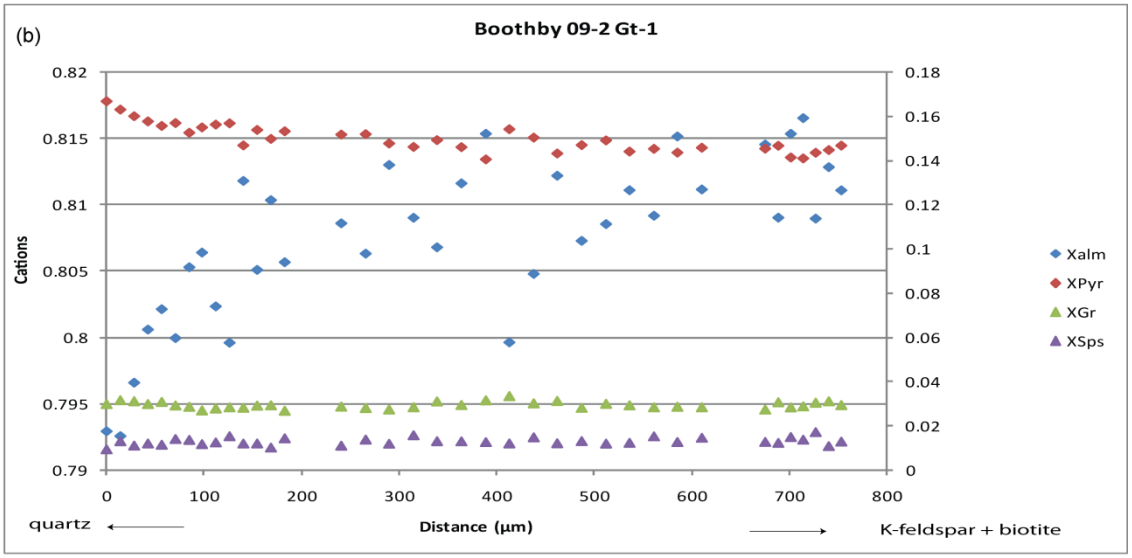
(b)
Boothby 09-2 Gt-1
Cations
Distance (µm)
quartz
K-feldspar + biotite
Xalm
XPyr
XGr
XSps

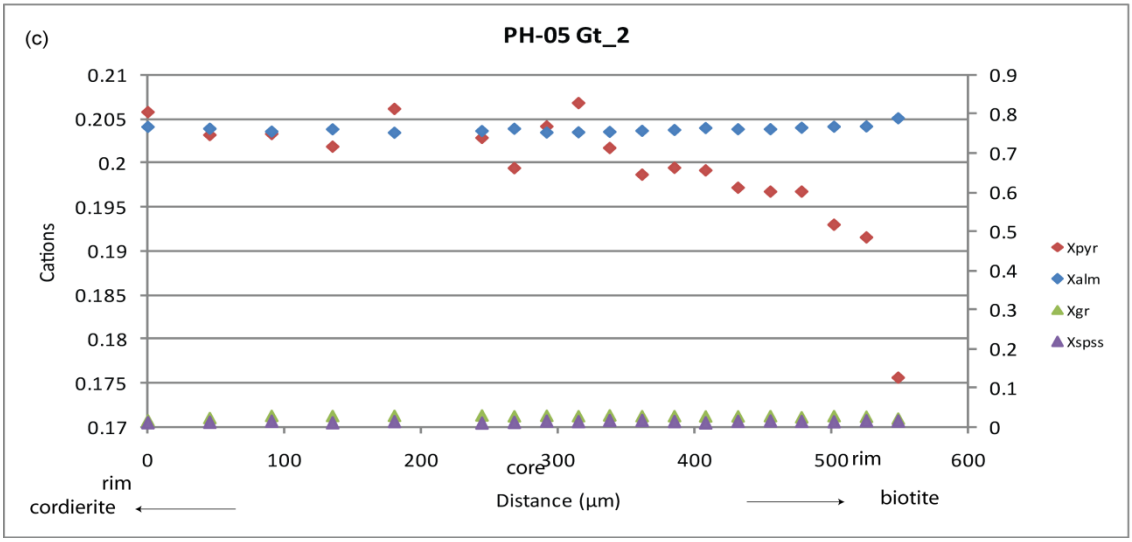
(c)
PH-05 Gt_2
Cations
Distance (µm)
rim
cordierite
core
rim
biotite
Xpyr
Xalm
Xgr
Xspss

Figure 5

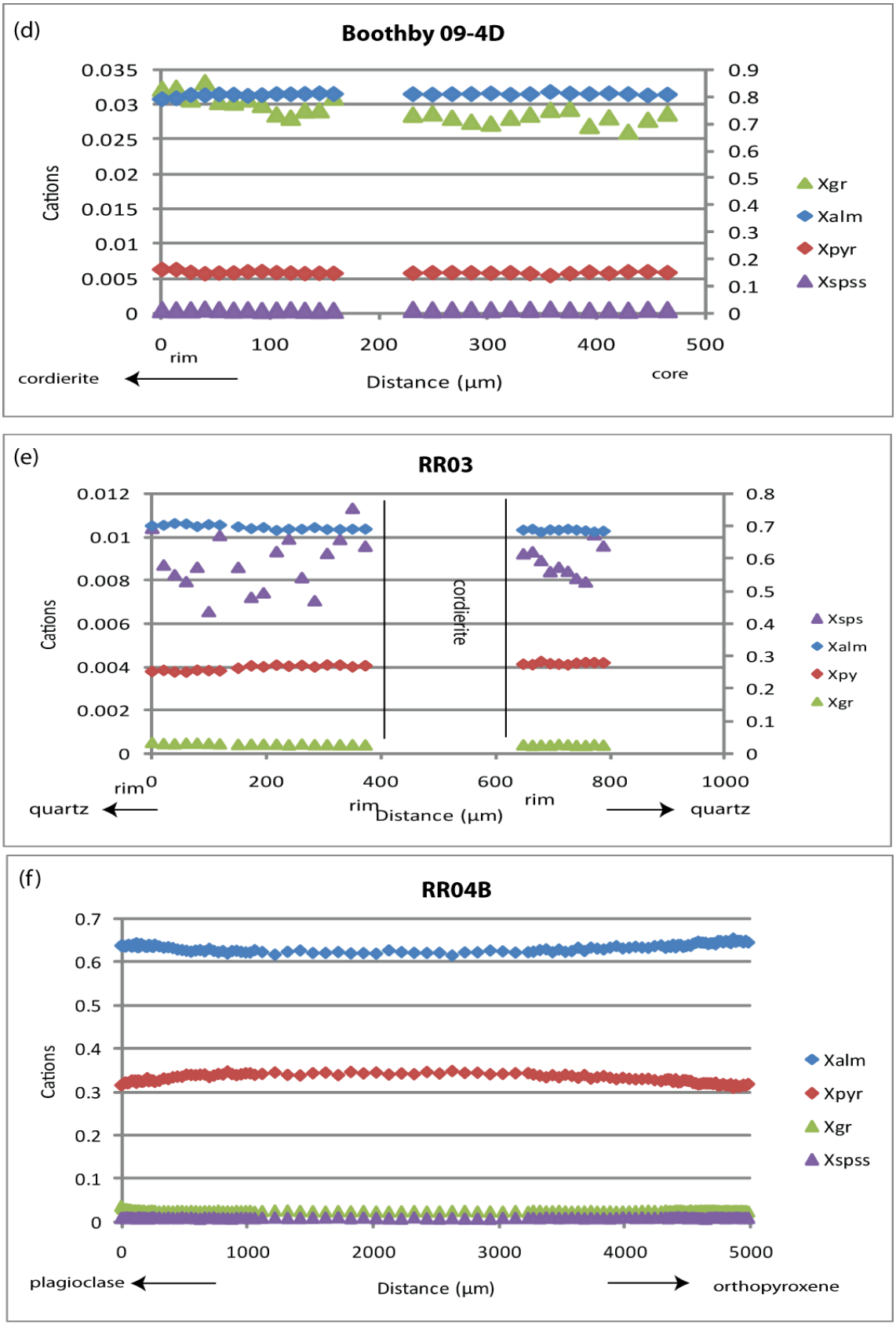

Figure 5 continued

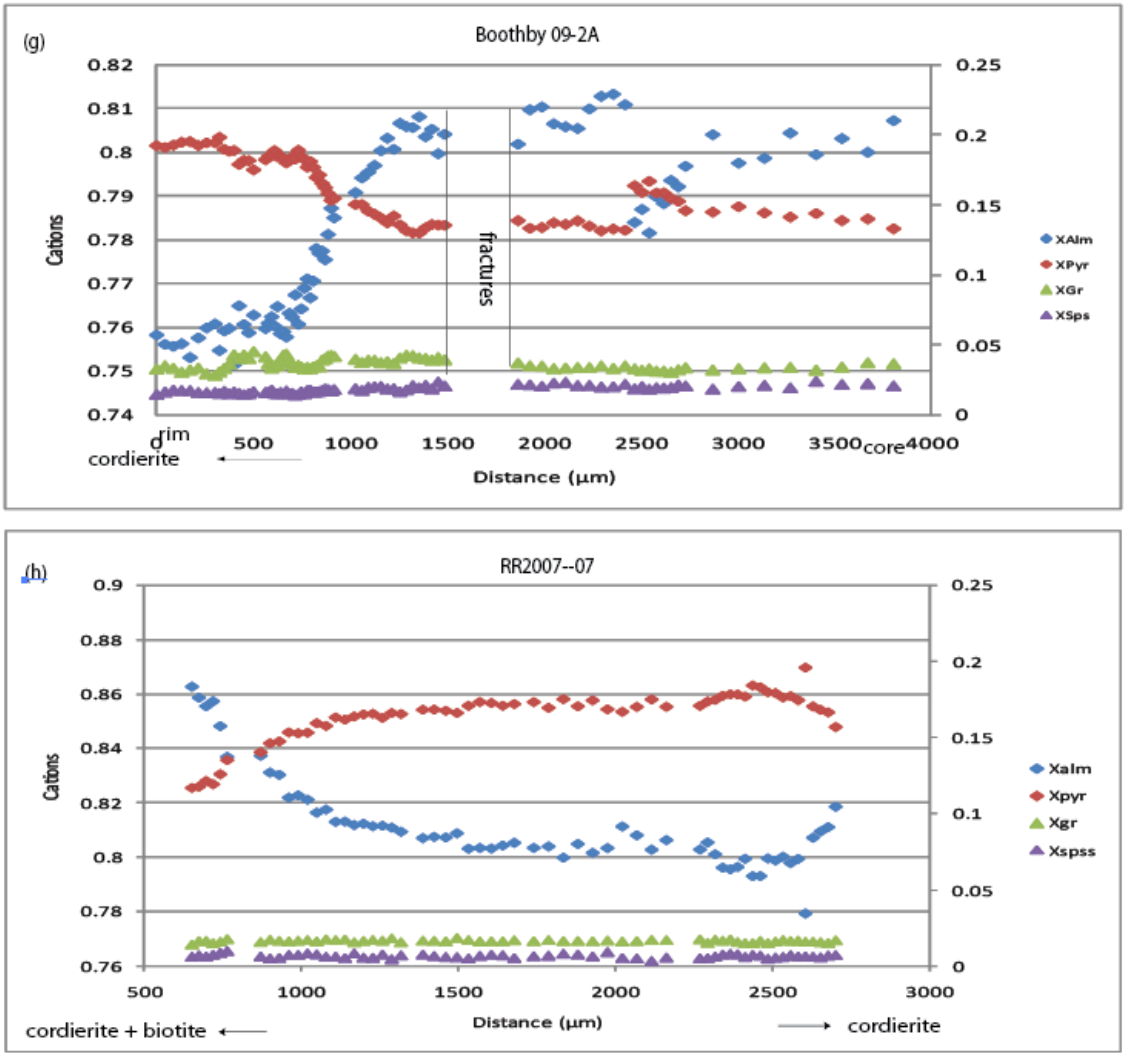

Figure 5 continued

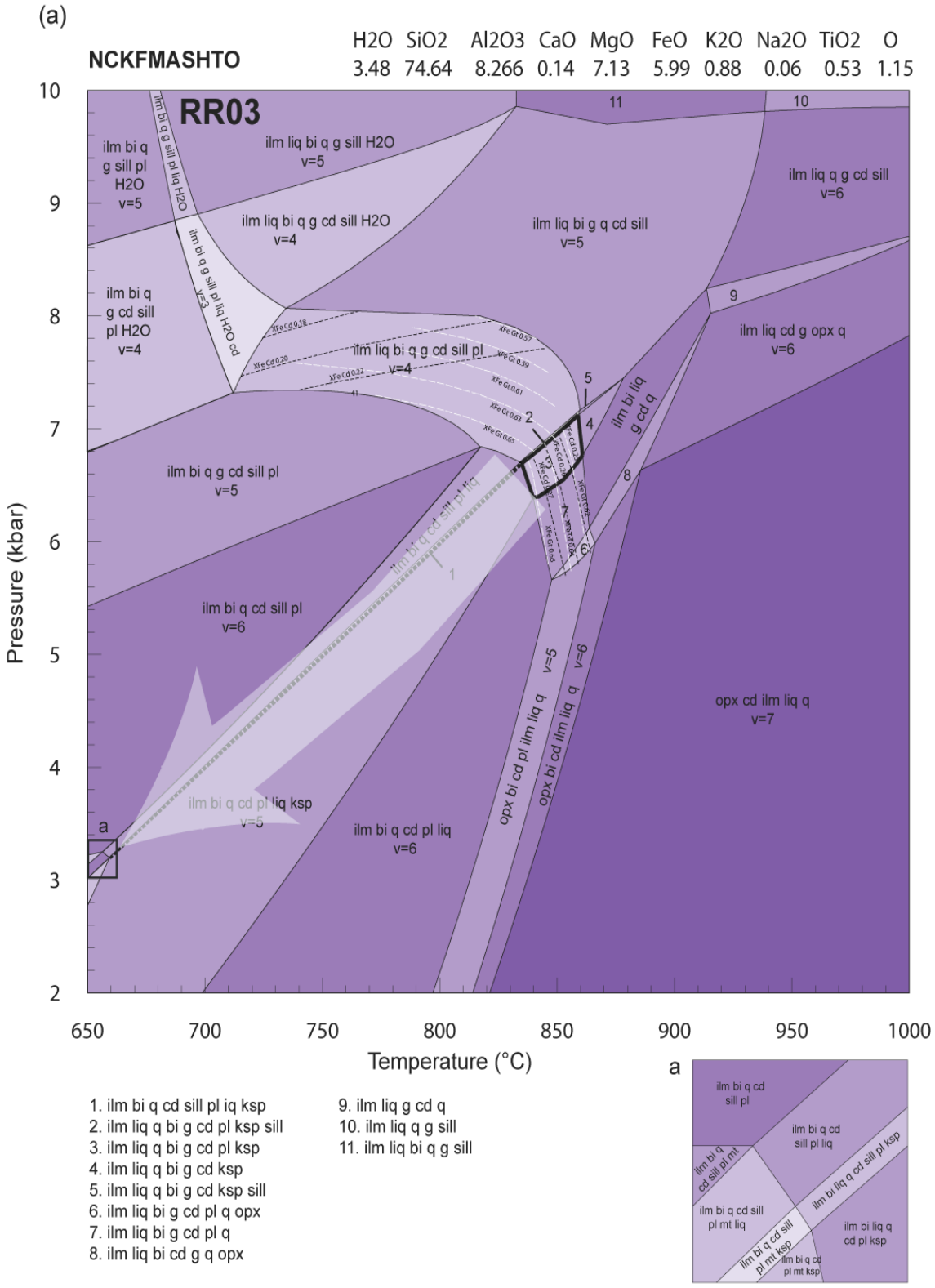
(a)
NCKFMASHTO
H2O SiO2 Al2O3 CaO MgO FeO K2O Na2O TiO2 O
3.48 74.64 8.266 0.14 7.13 5.99 0.88 0.06 0.53 1.15
RR03
ilm bi q g sill pl liq H2O
ilm liq bi q g sill H2O v=5
ilm bi q g sill pl liq H2O cd v=3
ilm bi q g sill pl H2O v=5
ilm liq bi q g cd sill H2O v=4
ilm liq bi g q cd sill v=5
ilm liq q g cd sill v=6
ilm bi q g cd sill pl H2O v=4
ilm liq bi q g cd sill pl v=4
ilm liq cd g opx q v=6
ilm bi liq g cd q
ilm bi q g cd sill pl v=5
ilm bi q cd sill pl v=6
ilm bi q cd sill pl liq
ilm bi q cd pl liq ksp v=5
ilm bi q cd pl liq v=6
opx bi cd pl ilm liq q v=5
opx bi cd ilm liq q v=6
opx cd ilm liq q v=7
Pressure (kbar)
Temperature (°C)
1. ilm bi q cd sill pl iq ksp
2. ilm liq q bi g cd pl ksp sill
3. ilm liq q bi g cd pl ksp
4. ilm liq q bi g cd ksp
5. ilm liq q bi g cd ksp sill
6. ilm liq bi g cd pl q opx
7. ilm liq bi g cd pl q
8. ilm liq bi cd g q opx
9. ilm liq g cd q
10. ilm liq q g sill
11. ilm liq bi q g sill
a
ilm bi q cd sill pl
ilm bi q cd sill pl liq
ilm bi q cd sill pl mt
ilm bi liq q cd sill pl ksp
ilm bi q cd sill pl mt liq
ilm bi liq q cd pl ksp
ilm bi q cd sill pl mt ksp
ilm bi q cd pl mt ksp

Figure 6

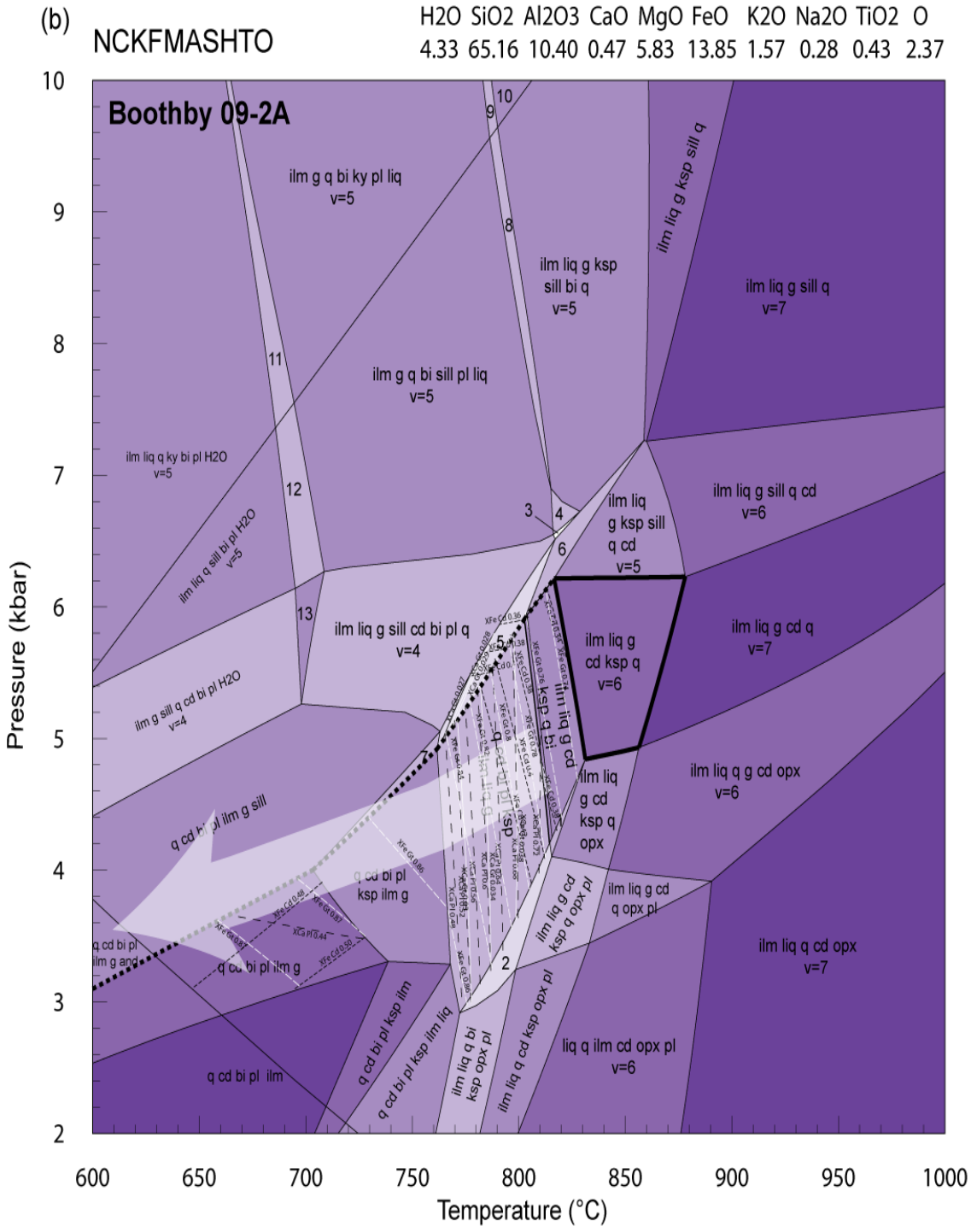

1. ilm liq g cd ksp q bi opx
2. ilm liq q cd bi ksp g opx pl
3. ilm liq g sill q cd bi
4. ilm liq g sill bi q
5. sill q cd bi pl ksp ilm liq q
6. ilm liq g ksp sill q cd bi
7. sill q cd bi pl ksp ilm g
8. ilm liq bi g pl sill q ksp
9. ilm liq bi g pl ky q ksp
10. ilm liq bi g ksp q ky
11. ilm q bi ky g pl liq H2O
12. ilm liq g sill q bi pl H2O
13. ilm liq g sill q cd bi pl H2O

Figure 6 continued

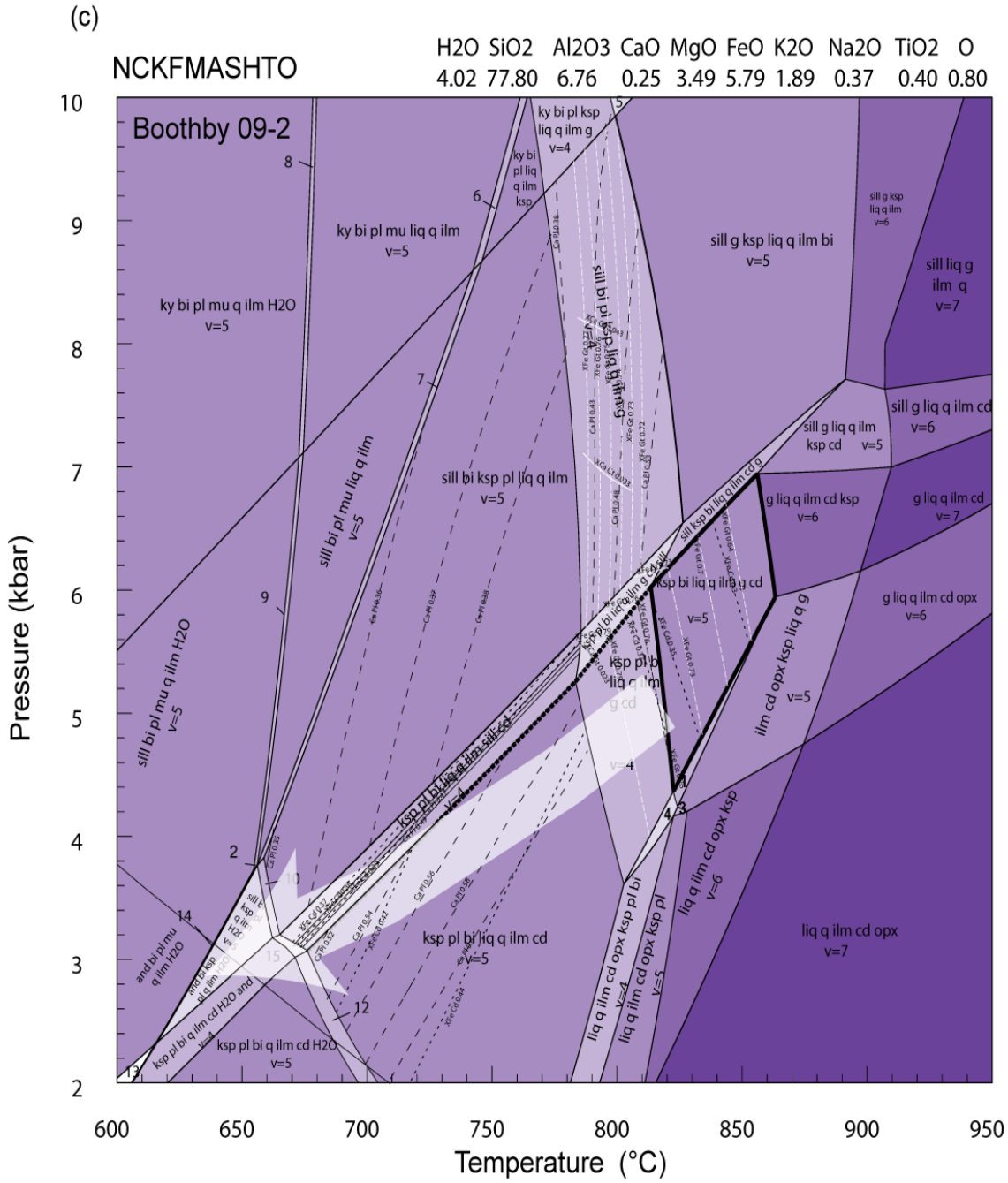

1. g liq q ilm cd opx ksp bi
2. sill bi pl mu liq q ilm ksp
3. liq q ilm cd ksp opx pl g
4. ksp pl bi liq q ilm g cd opx
5. sill bi pl ksp liq q ilm g
6. ky bi pl mu liq q ilm ksp
7. sill bi pl mu liq q ilm ksp
8. ky bi pl mu liq q ilm H2O
9. sill bi pl mu liq q ilm H2O
10. sill bi ksp pl liq q ilm H2O
11. sill bi ksp pl liq q ilm H2O cd
12. ksp pl bi liq q ilm cd H2O
13. and bi pl mu q ilm cd H2O
14. sill bi pl mu liq q ilm H2O
15. ksp pl bi q ilm cd H2O sill

Figure 6 continued

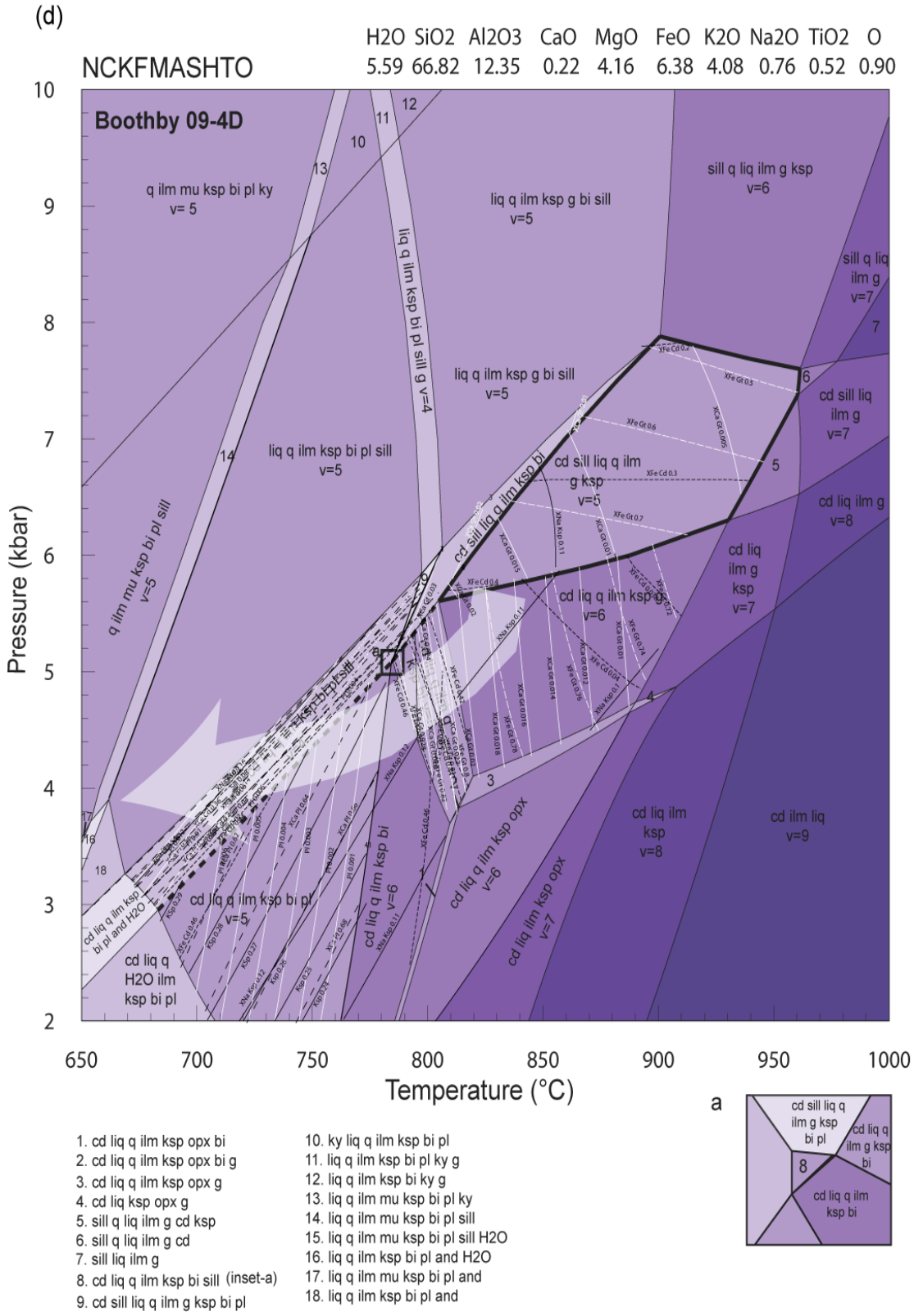

Figure 6 continued

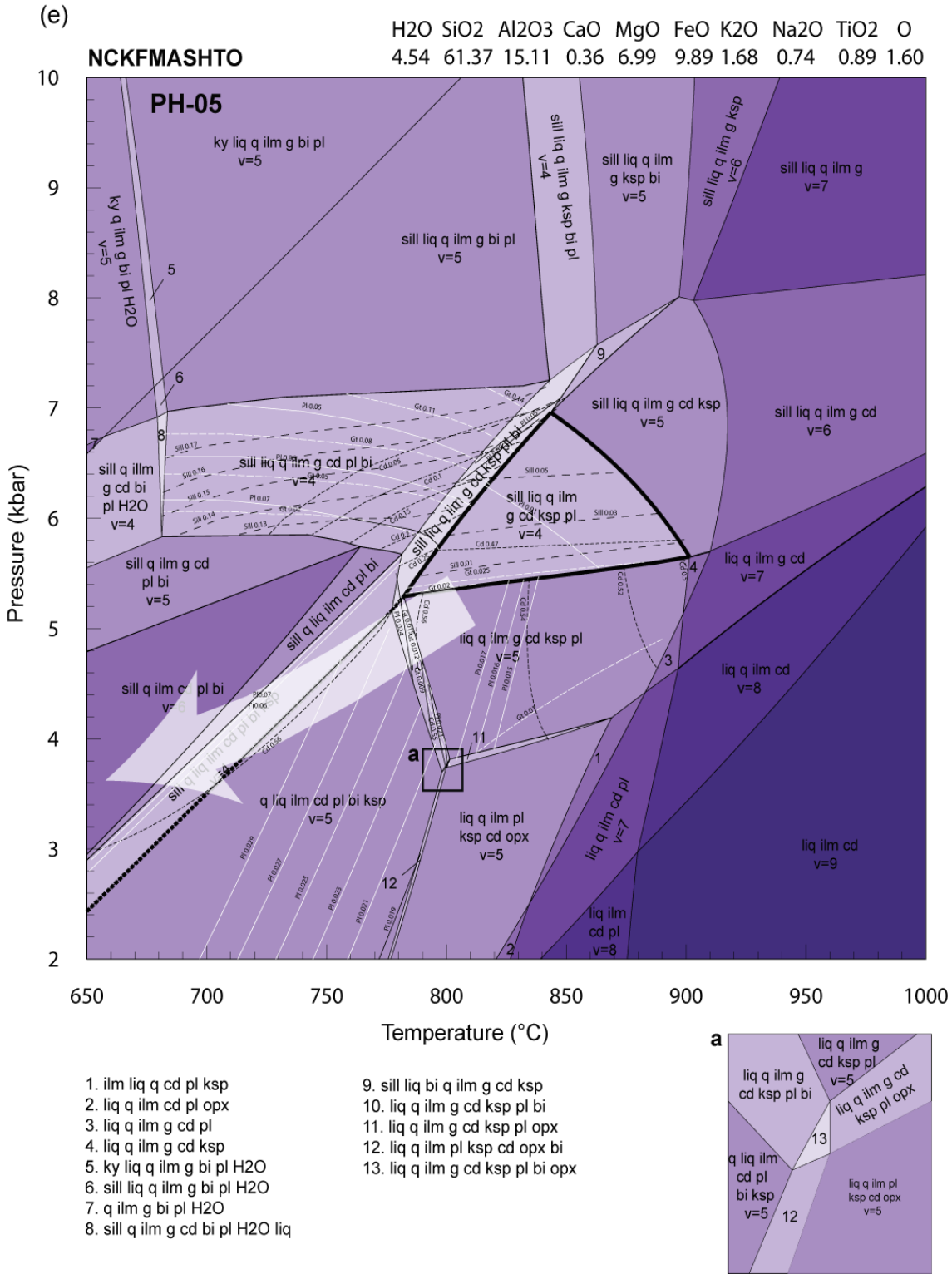

Figure 6 continued

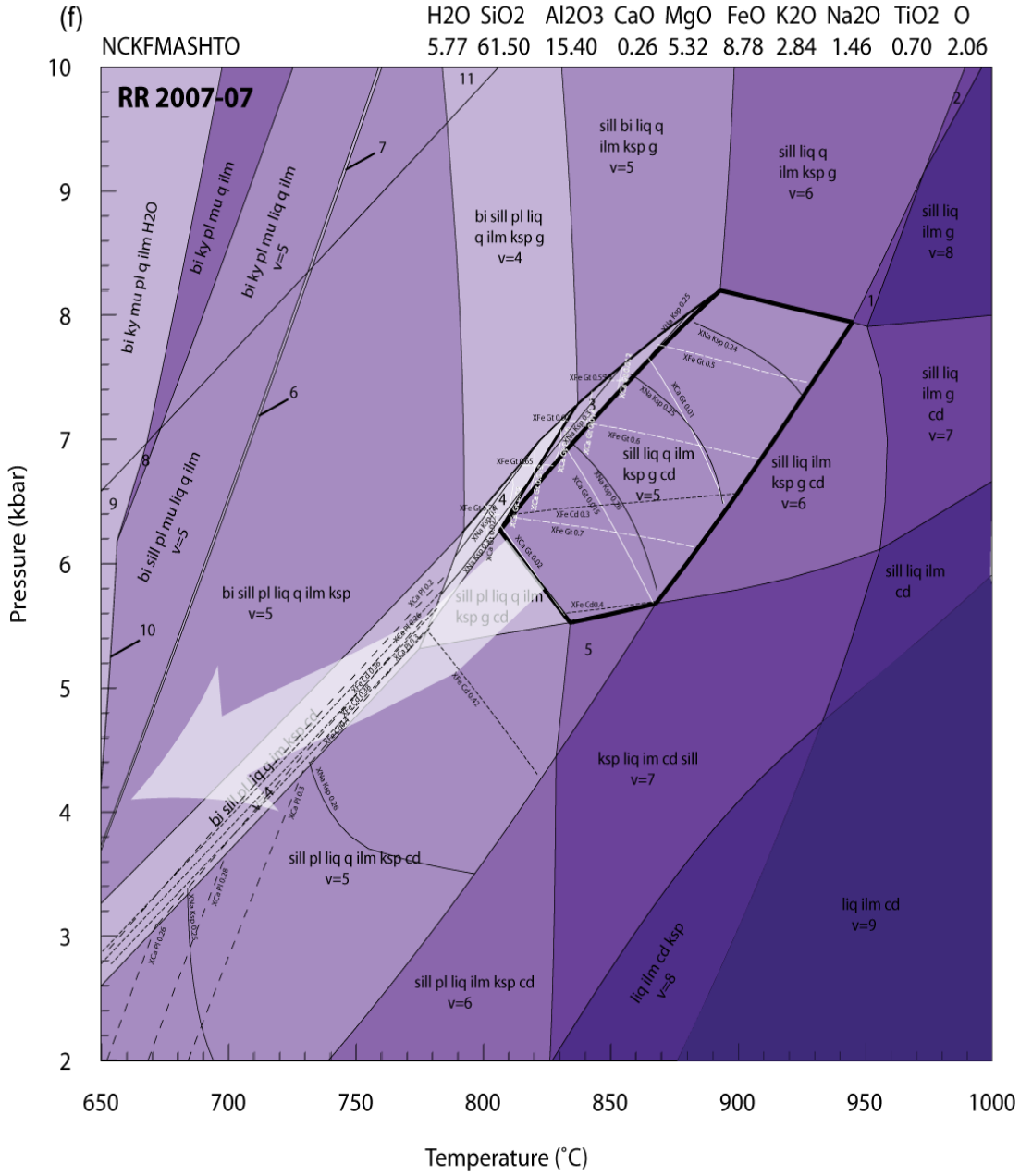

Figure 6 continued

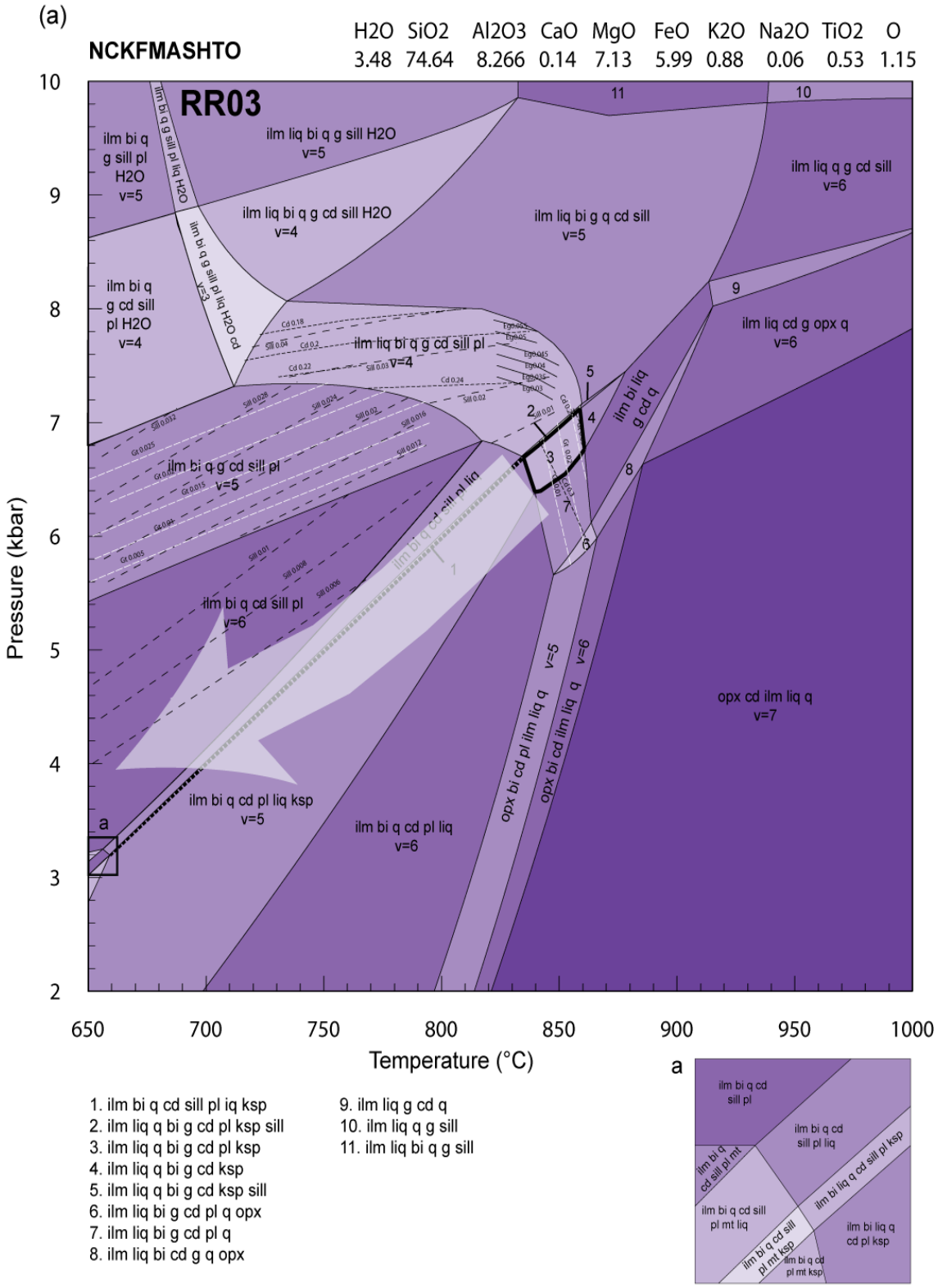
(a)
NCKFMASHTO
H2O SiO2 Al2O3 CaO MgO FeO K2O Na2O TiO2 O
3.48 74.64 8.266 0.14 7.13 5.99 0.88 0.06 0.53 1.15
RR03
ilm bi q g sill pl H2O v=5
ilm liq bi q g sill H2O v=5
ilm liq bi q g cd sill H2O v=4
ilm liq bi g q cd sill v=5
ilm liq q g cd sill v=6
ilm bi q g cd sill pl H2O v=4
ilm liq bi q g cd sill pl v=4
ilm liq cd g opx q v=6
ilm bi q g cd sill pl v=5
ilm bi q cd sill pl v=6
opx cd ilm liq q v=7
ilm bi q cd pl liq ksp v=5
ilm bi q cd pl liq v=6
opx bi cd pl ilm liq q v=5
opx bi cd ilm liq q v=6
Pressure (kbar)
Temperature (°C)
1. ilm bi q cd sill pl iq ksp
2. ilm liq q bi g cd pl ksp sill
3. ilm liq q bi g cd pl ksp
4. ilm liq q bi g cd ksp
5. ilm liq q bi g cd ksp sill
6. ilm liq bi g cd pl q opx
7. ilm liq bi g cd pl q
8. ilm liq bi cd g q opx
9. ilm liq g cd q
10. ilm liq q g sill
11. ilm liq bi q g sill
a
ilm bi q cd sill pl
ilm bi q cd sill pl liq
ilm bi q cd sill pl mt
ilm bi liq q cd sill pl ksp
ilm bi q cd sill pl mt liq
ilm bi liq q cd pl ksp
ilm bi q cd sill pl mt ksp

Figure 7

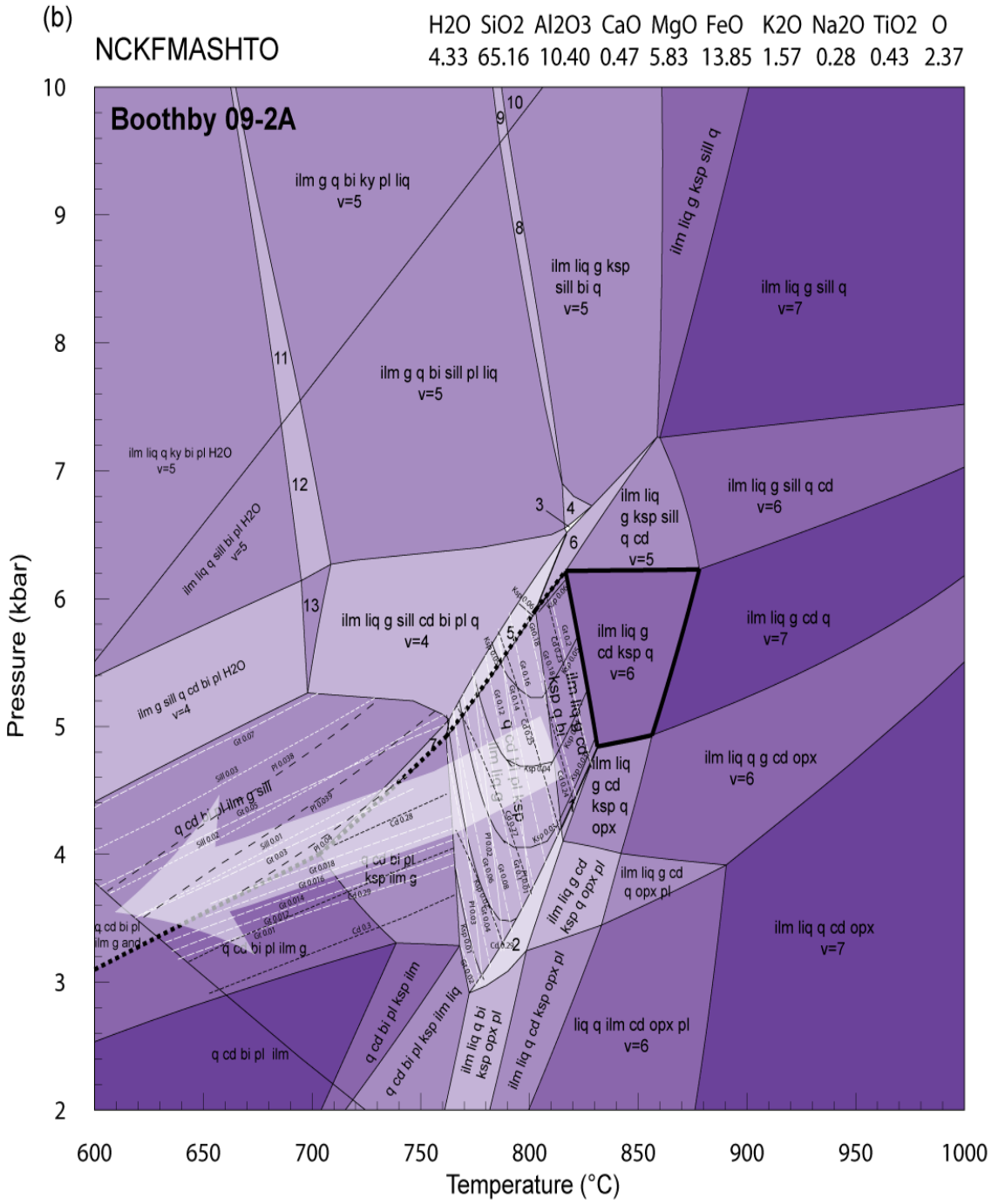

1. ilm liq g cd ksp q bi opx
2. ilm liq q cd bi ksp g opx pl
3. ilm liq g sill q cd bi
4. ilm liq g sill bi q
5. sill q cd bi pl ksp ilm liq q
6. ilm liq g ksp sill q cd bi
7. sill q cd bi pl ksp ilm g
8. ilm liq bi g pl sill q ksp
9. ilm liq bi g pl ky q ksp
10. ilm liq bi g ksp q ky
11. ilm q bi ky g pl liq H2O
12. ilm liq g sill q bi pl H2O
13. ilm liq g sill q cd bi pl H2O

Figure 7 continued

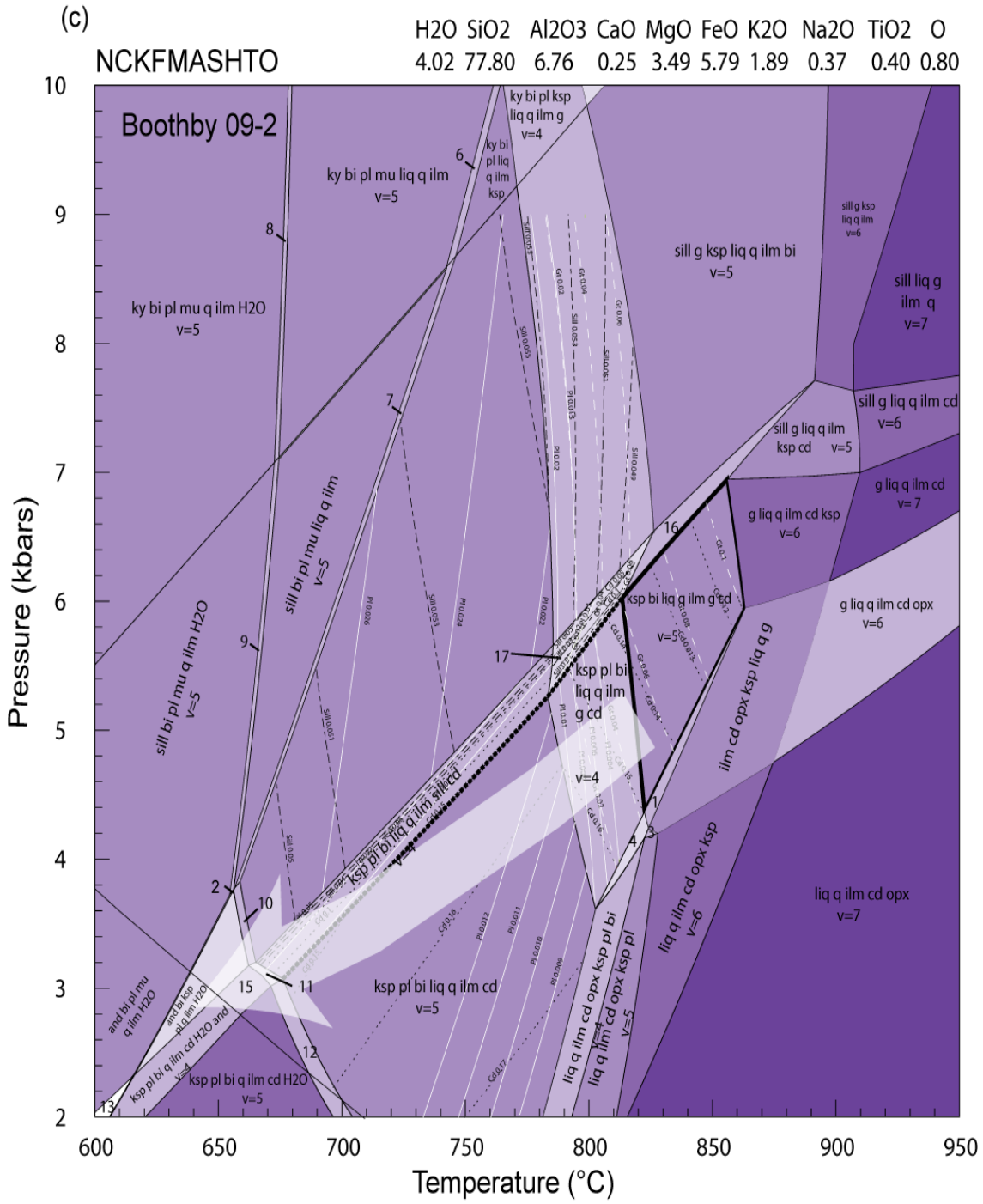

1. g liq q ilm cd opx ksp bi
2. sill bi pl mu liq q ilm ksp
3. liq q ilm cd ksp opx pl g
4. ksp pl bi liq q ilm g cd opx
5. sill bi pl ksp liq q ilm g
6. ky bi pl mu liq q ilm ksp
7. sill bi pl mu liq q ilm ksp
8. ky bi pl mu liq q ilm H2O
9. sill bi pl mu liq q ilm H2O
10. sill bi ksp pl liq q ilm H2O
11. sill bi ksp pl liq q ilm H2O cd
12. ksp pl bi liq q ilm cd H2O
13. and bi pl mu q ilm cd H2O
14. sill bi pl mu liq q ilm H2O
15. ksp pl bi q ilm cd H2O sill
16. sill ksp bi liq q ilm cd g
17. ksp pl bi liq q ilm g cd sill

Figure 7 continued

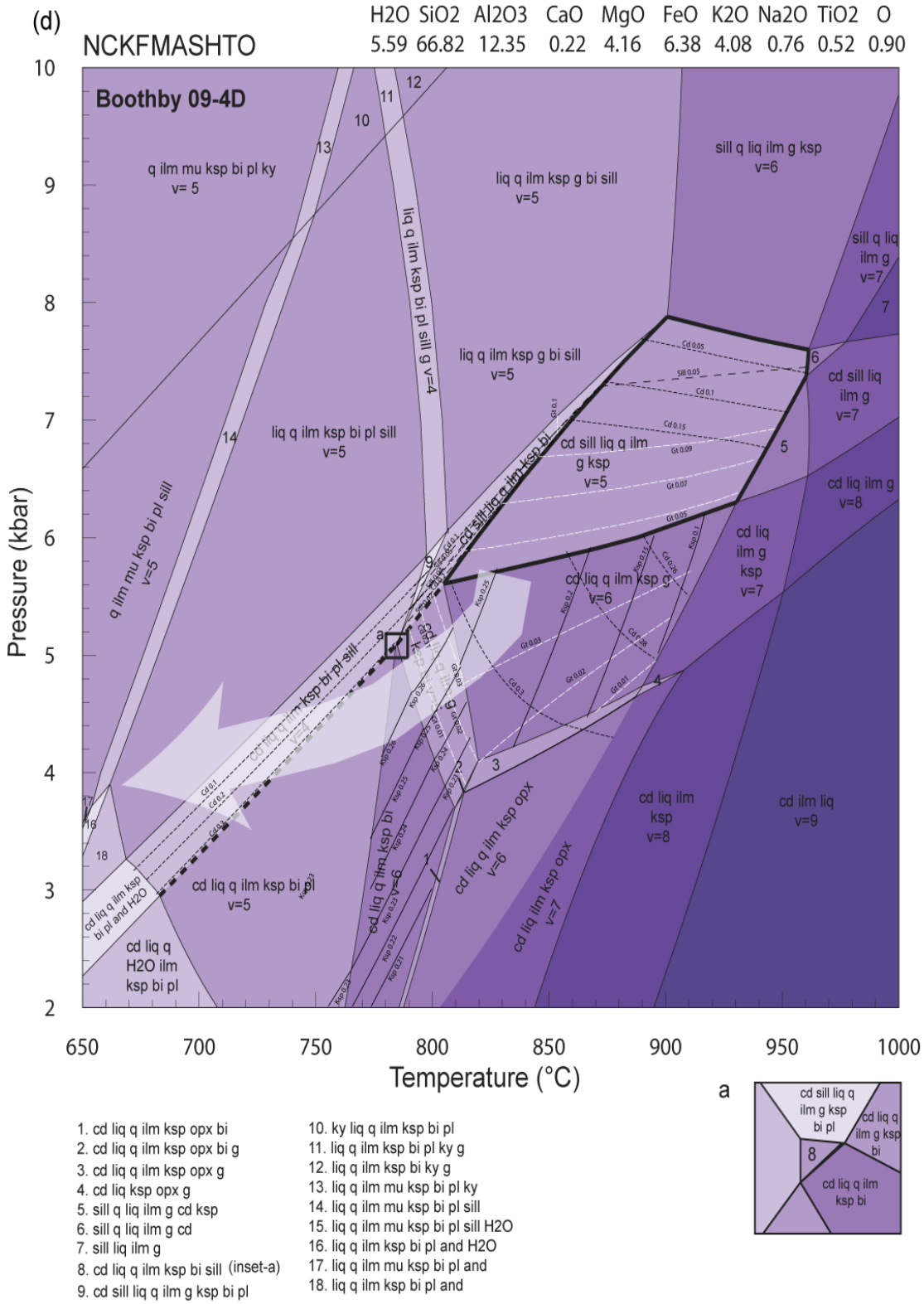

Figure 7 continued

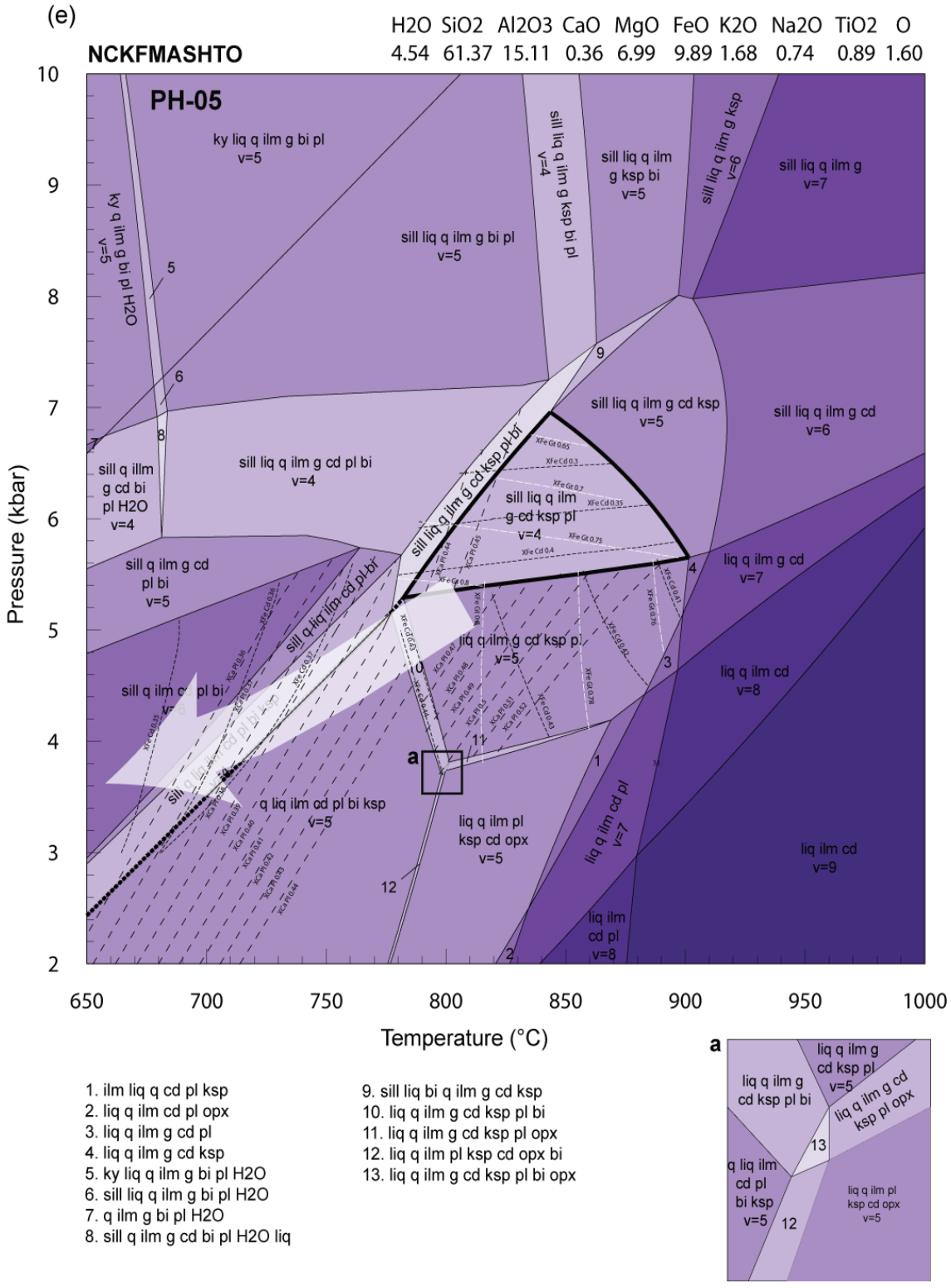

Figure 7 continued

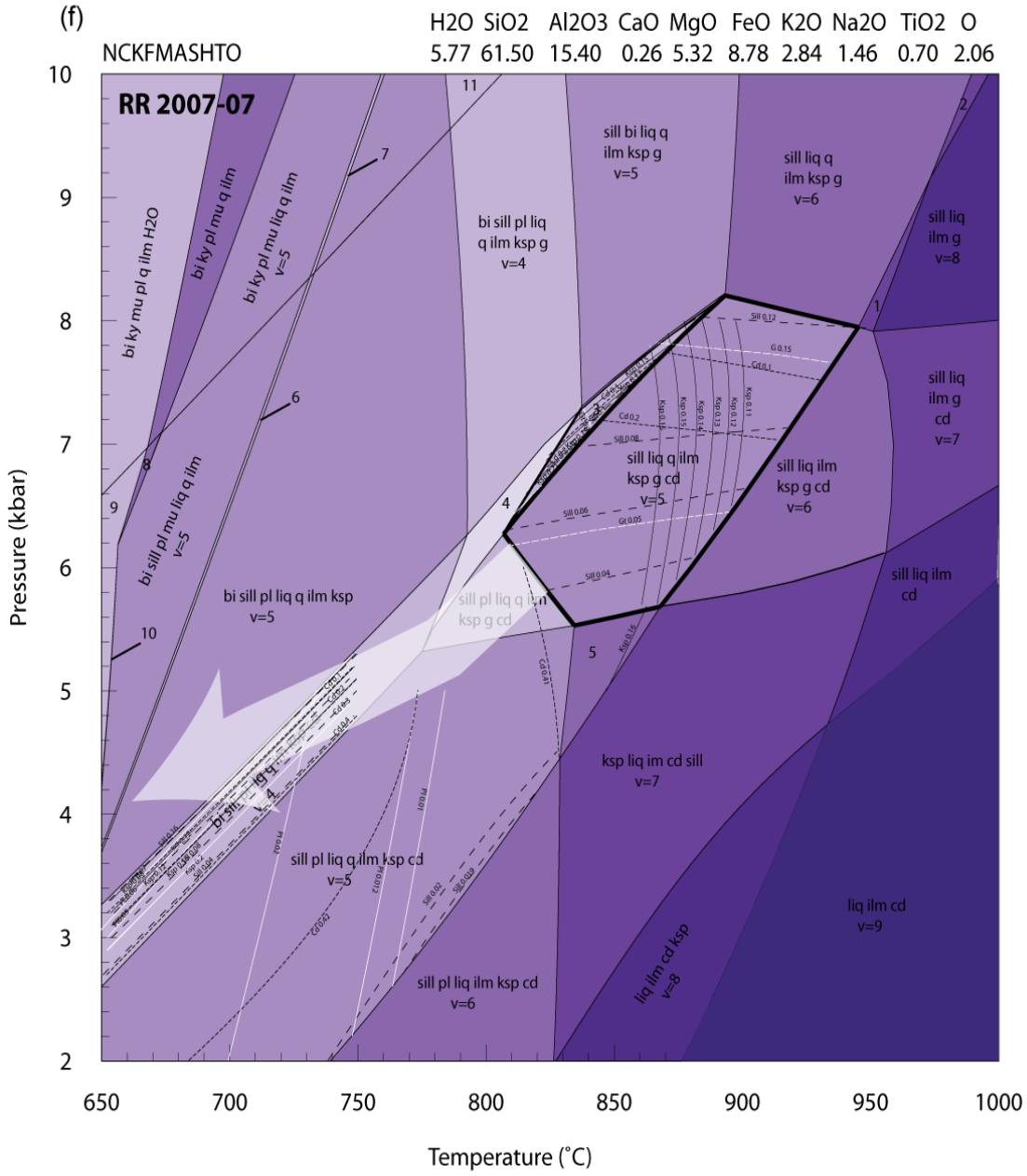

1. sill liq ilm ksp g
2. sill liq q ilm g
3. sill liq q ilm ksp g cd bi
4. bi sill pl liq q ilm ksp g cd
5. ksp liq q ilm cd sill
6. bi sill pl mu liq q ilm ksp
7. bi ky pl mu liq q ilm ksp
8. bi sill mu pl q ilm
9. bi sill mu pl q ilm H2O
10. sill bi pl mu H2O liq q ilm
11. bi ky pl liq q ilm g ksp

Figure 7 continued

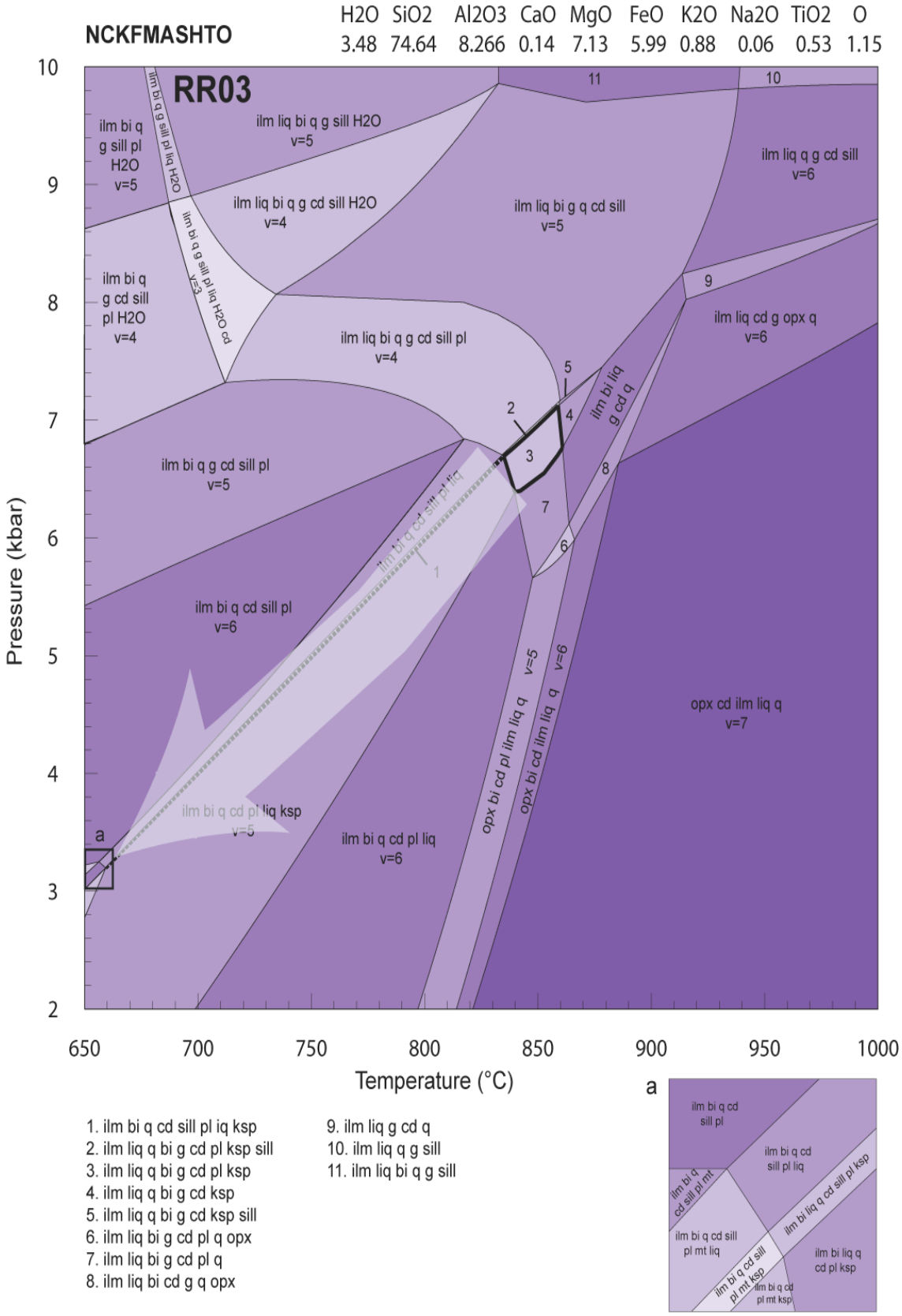
NCKFMASHTO
H2O SiO2 Al2O3 CaO MgO FeO K2O Na2O TiO2 O
3.48 74.64 8.266 0.14 7.13 5.99 0.88 0.06 0.53 1.15
RR03
ilm bi q g sill pl H2O v=5
ilm liq bi q g sill H2O v=5
ilm liq bi q g cd sill H2O v=4
ilm liq bi g q cd sill v=5
ilm liq q g cd sill v=6
ilm bi q g cd sill pl H2O v=4
ilm liq bi q g cd sill pl v=4
ilm liq cd g opx q v=6
ilm bi q g cd sill pl v=5
ilm bi q cd sill pl v=6
opx cd ilm liq q v=7
ilm bi q cd pl liq ksp v=5
ilm bi q cd pl liq v=6
Pressure (kbar)
Temperature (°C)
1. ilm bi q cd sill pl iq ksp
2. ilm liq q bi g cd pl ksp sill
3. ilm liq q bi g cd pl ksp
4. ilm liq q bi g cd ksp
5. ilm liq q bi g cd ksp sill
6. ilm liq bi g cd pl q opx
7. ilm liq bi g cd pl q
8. ilm liq bi cd g q opx
9. ilm liq g cd q
10. ilm liq q g sill
11. ilm liq bi q g sill
a
ilm bi q cd sill pl
ilm bi q cd sill pl liq
ilm bi q cd sill pl mt liq
ilm bi liq q cd pl ksp

Figure 8

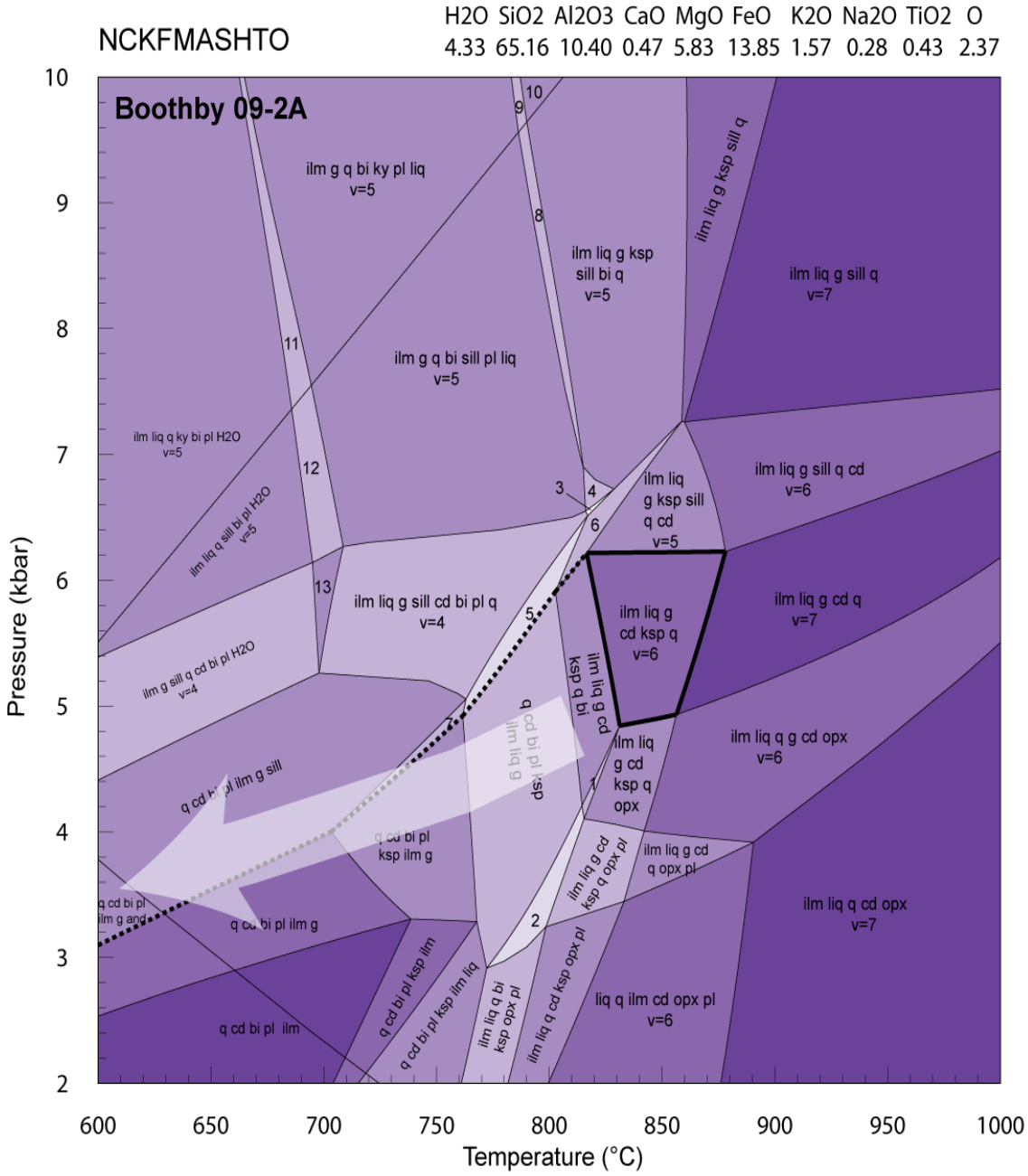

1. ilm liq g cd ksp q bi opx
2. ilm liq q cd bi ksp g opx pl
3. ilm liq g sill q cd bi
4. ilm liq g sill bi q
5. sill q cd bi pl ksp ilm liq q
6. ilm liq g ksp sill q cd bi
7. sill q cd bi pl ksp ilm g
8. ilm liq bi g pl sill q ksp
9. ilm liq bi g pl ky q ksp
10. ilm liq bi g ksp q ky
11. ilm q bi ky g pl liq H2O
12. ilm liq g sill q bi pl H2O
13. ilm liq g sill q cd bi pl H2O

Figure 9

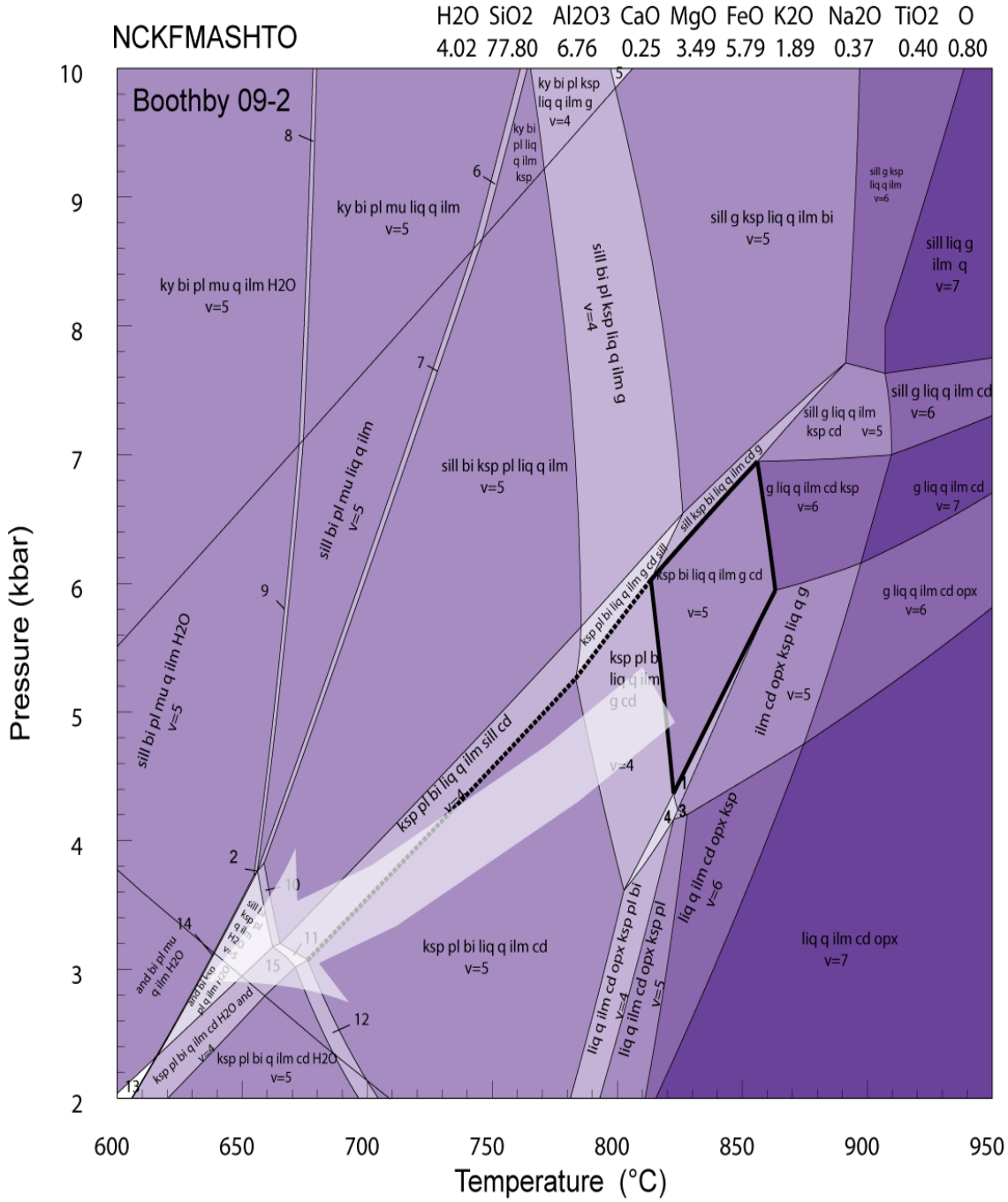

1. g liq q ilm cd opx ksp bi
2. sill bi pl mu liq q ilm ksp
3. liq q ilm cd ksp opx pl g
4. ksp pl bi liq q ilm g cd opx
5. sill bi pl ksp liq q ilm g
6. ky bi pl mu liq q ilm ksp
7. sill bi pl mu liq q ilm ksp
8. ky bi pl mu liq q ilm H2O
9. sill bi pl mu liq q ilm H2O
10. sill bi ksp pl liq q ilm H2O
11. sill bi ksp pl liq q ilm H2O cd
12. ksp pl bi liq q ilm cd H2O
13. and bi pl mu q ilm cd H2O
14. sill bi pl mu liq q ilm H2O
15. ksp pl bi q ilm cd H2O sill

Figure 10

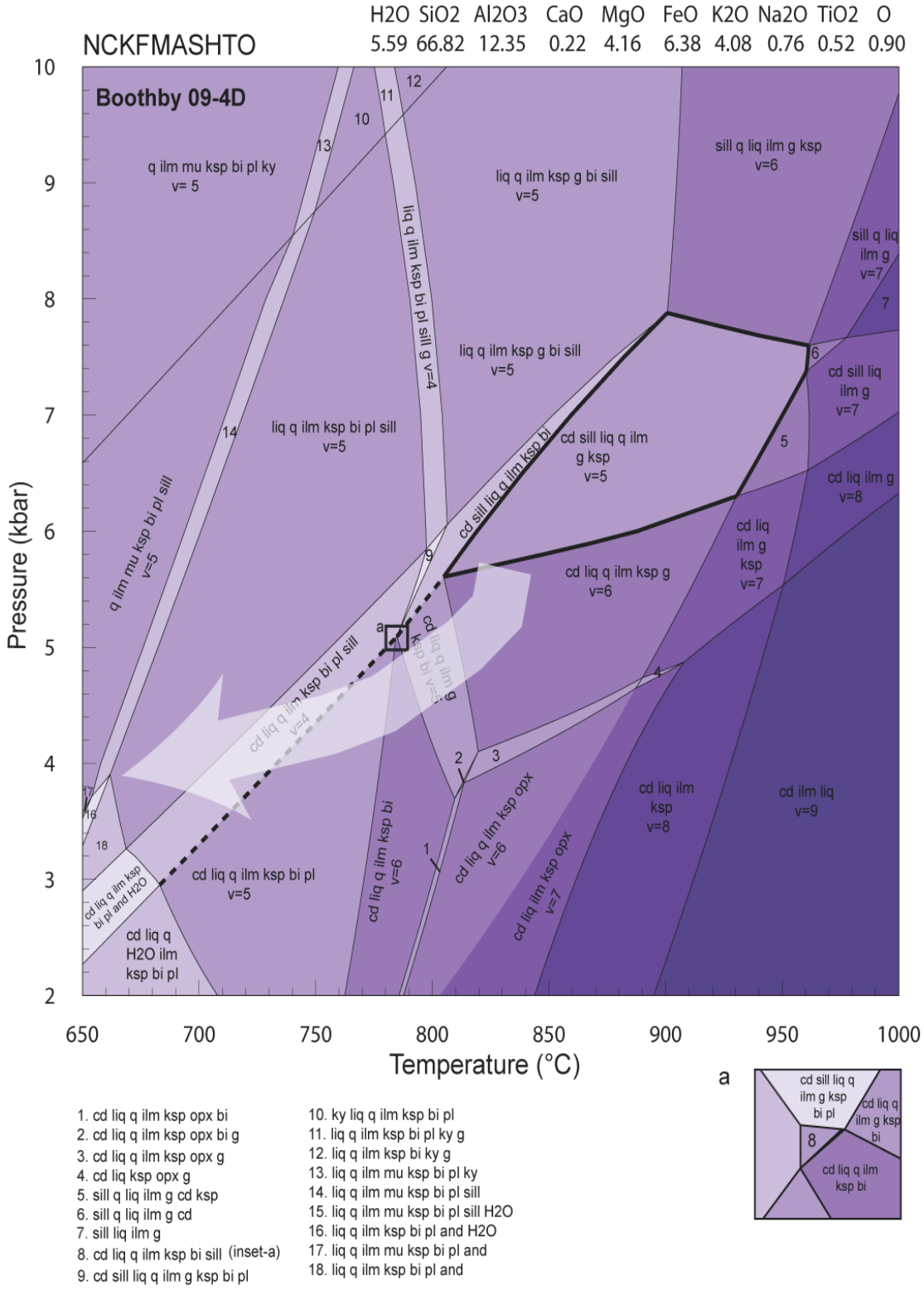

1. cd liq q ilm ksp opx bi
2. cd liq q ilm ksp opx bi g
3. cd liq q ilm ksp opx g
4. cd liq ksp opx g
5. sill q liq ilm g cd ksp
6. sill q liq ilm g cd
7. sill liq ilm g
8. cd liq q ilm ksp bi sill (inset-a)
9. cd sill liq q ilm g ksp bi pl
10. ky liq q ilm ksp bi pl
11. liq q ilm ksp bi pl ky g
12. liq q ilm ksp bi ky g
13. liq q ilm mu ksp bi pl ky
14. liq q ilm mu ksp bi pl sill
15. liq q ilm mu ksp bi pl sill H2O
16. liq q ilm ksp bi pl and H2O
17. liq q ilm mu ksp bi pl and
18. liq q ilm ksp bi pl and

Figure 11

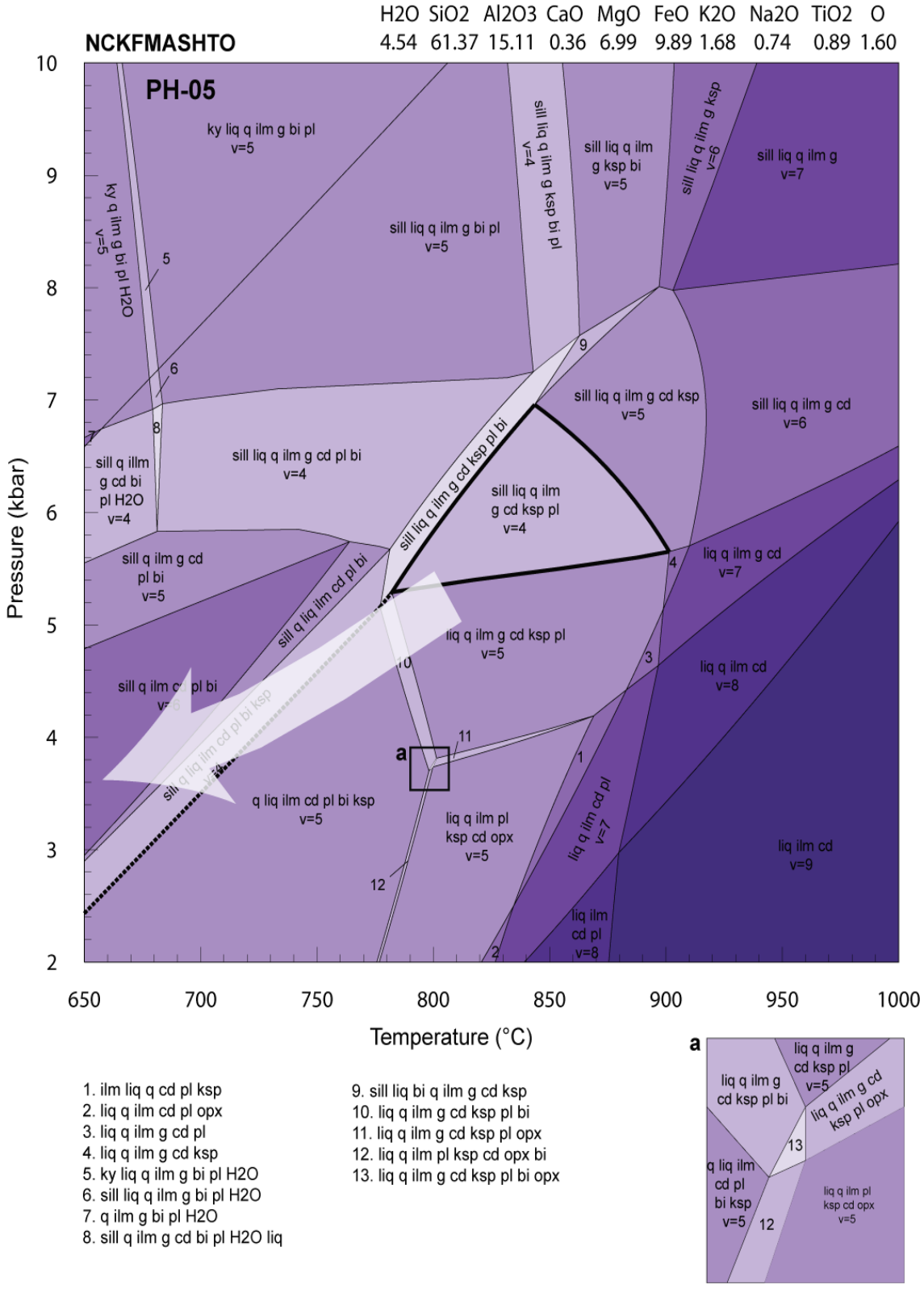
H2O SiO2 Al2O3 CaO MgO FeO K2O Na2O TiO2 O
NCKFMASHTO
4.54 61.37 15.11 0.36 6.99 9.89 1.68 0.74 0.89 1.60
PH-05
ky liq q ilm g bi pl v=5
sill liq q ilm g ksp bi pl v=4
sill liq q ilm g ksp v=6
sill liq q ilm g v=7
ky q ilm g bi pl H2O v=5
sill liq q ilm g bi pl v=5
sill liq q ilm g ksp bi v=5
sill liq q ilm g cd ksp v=5
sill liq q ilm g cd v=6
sill q illm g cd bi pl H2O v=4
sill liq q ilm g cd pl bi v=4
sill liq q ilm g cd ksp pl bi
sill liq q ilm g cd ksp pl v=4
sill q ilm g cd pl bi v=5
sill q liq ilm cd pl bi
liq q ilm g cd v=7
liq q ilm g cd ksp pl v=5
liq q ilm cd v=8
sill q ilm cd pl bi
sill q liq ilm cd pl bi ksp
a
q liq ilm cd pl bi ksp v=5
liq q ilm pl ksp cd opx v=5
liq q ilm cd pl v=7
liq ilm cd v=9
liq ilm cd pl v=8
Pressure (kbar)
Temperature (°C)
1. ilm liq q cd pl ksp
2. liq q ilm cd pl opx
3. liq q ilm g cd pl
4. liq q ilm g cd ksp
5. ky liq q ilm g bi pl H2O
6. sill liq q ilm g bi pl H2O
7. q ilm g bi pl H2O
8. sill q ilm g cd bi pl H2O liq
9. sill liq bi q ilm g cd ksp
10. liq q ilm g cd ksp pl bi
11. liq q ilm g cd ksp pl opx
12. liq q ilm pl ksp cd opx bi
13. liq q ilm g cd ksp pl bi opx
a
liq q ilm g cd ksp pl bi
liq q ilm g cd ksp pl v=5
liq q ilm g cd ksp pl opx
q liq ilm cd pl bi ksp v=5
liq q ilm pl ksp cd opx v=5

Figure 12

1. sill liq ilm ksp g
2. sill liq q ilm g
3. sill liq q ilm ksp g cd bi
4. bi sill pl liq q ilm ksp g cd
5. ksp liq q ilm cd sill
6. bi sill pl mu liq q ilm ksp
7. bi ky pl mu liq q ilm ksp
8. bi sill mu pl q ilm
9. bi sill mu pl q ilm H2O
10. sill bi pl mu H2O liq q ilm
11. bi ky pl liq q ilm g ksp

Figure 13

Sample RR04B

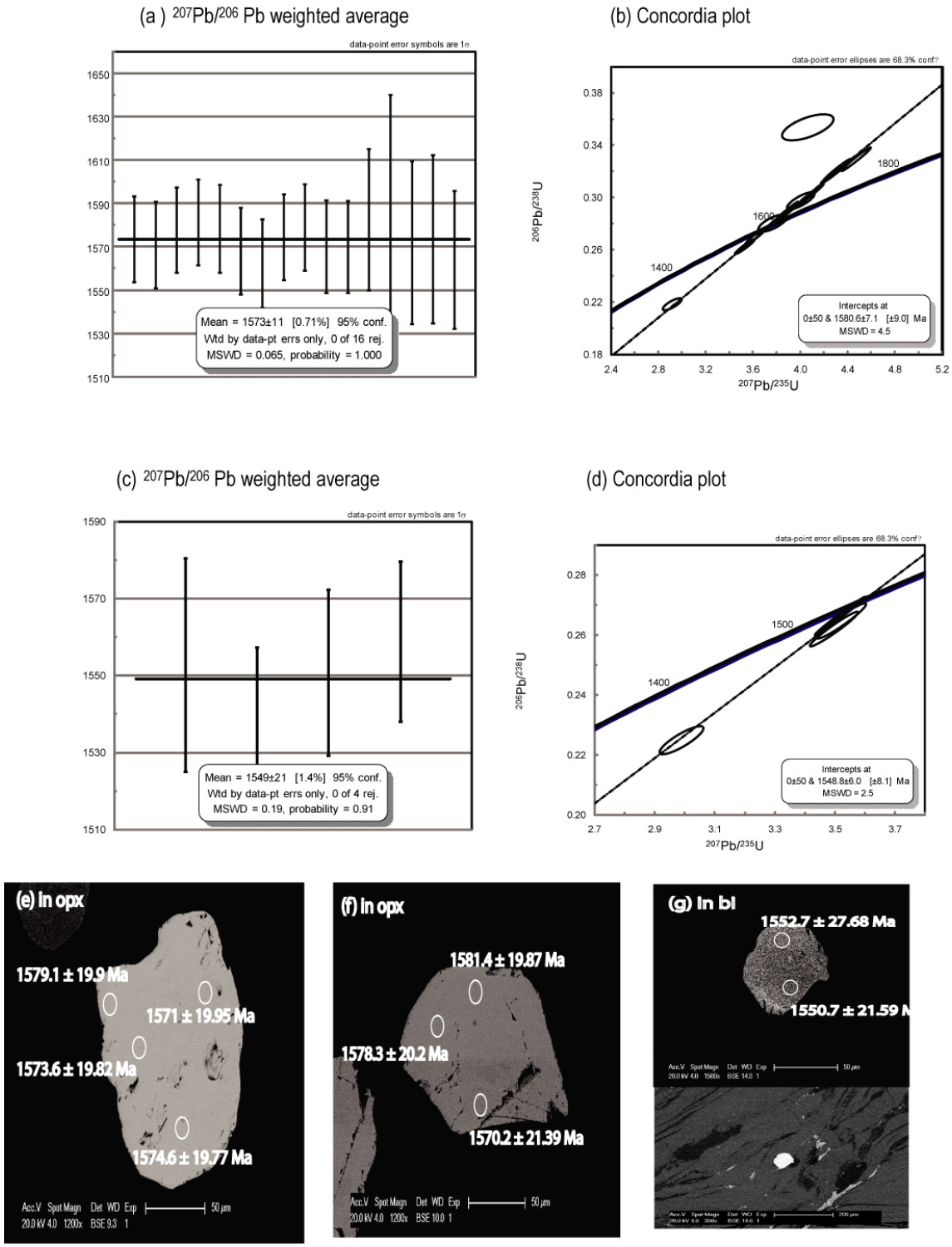

Figure 14

Sample RR051C

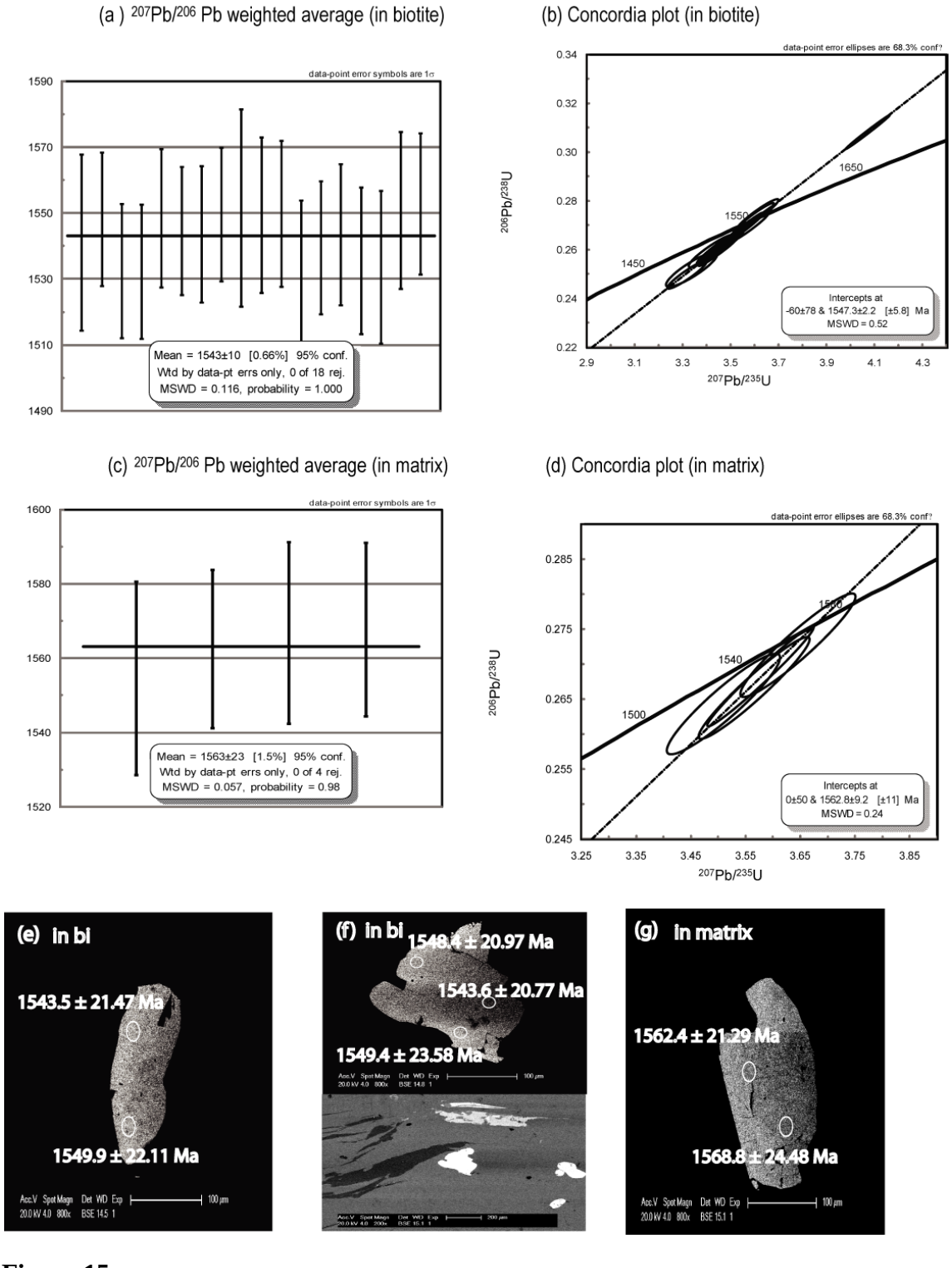

Figure 15

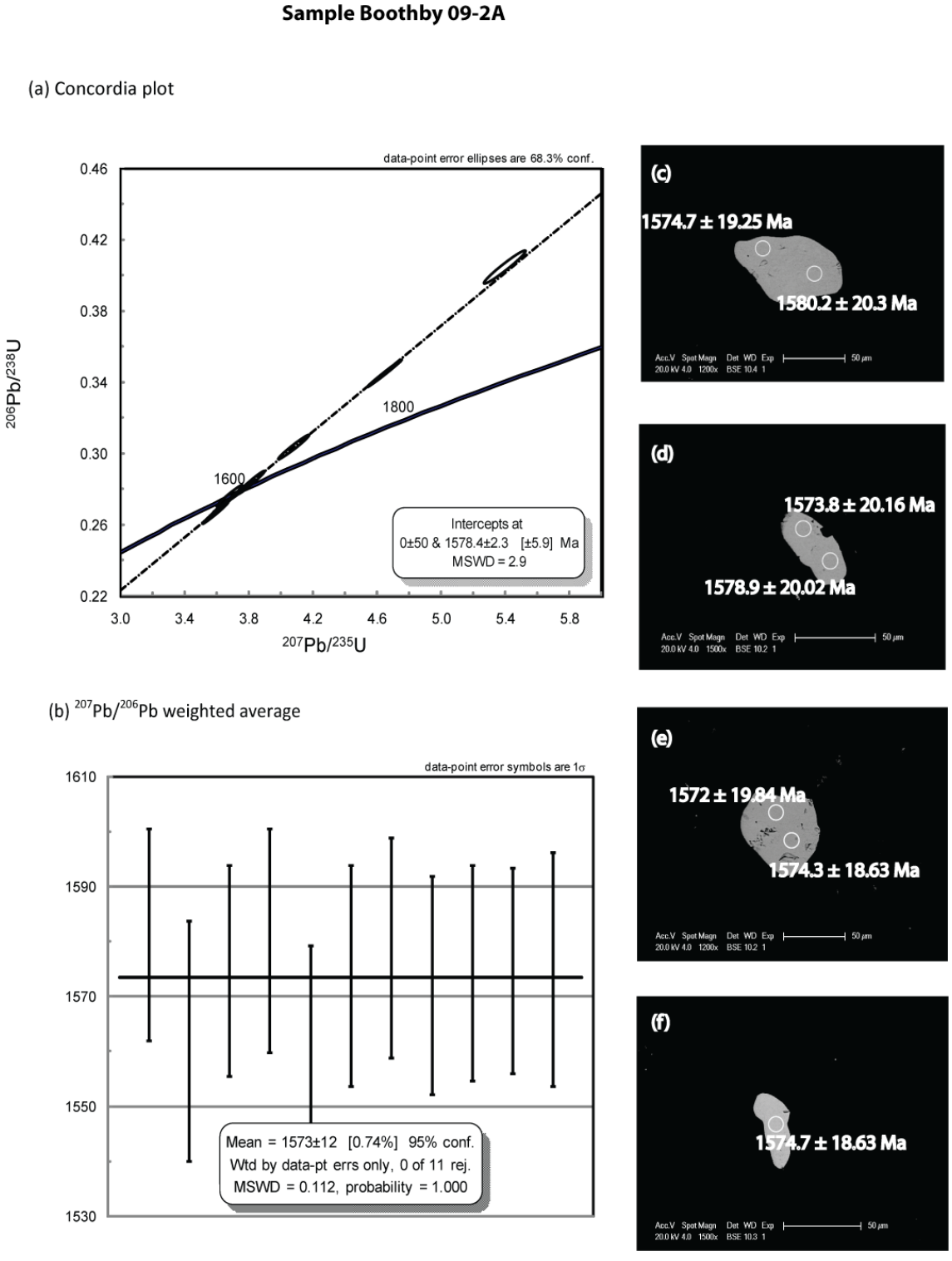
Sample Boothby 09-2A
(a) Concordia plot
data-point error ellipses are 68.3% conf.
0.46
0.42
0.38
0.34
0.30
0.26
0.22
206Pb/238U
1800
1600
Intercepts at
0±50 & 1578.4±2.3 [±5.9] Ma
MSWD = 2.9
3.0
3.4
3.8
4.2
4.6
5.0
5.4
5.8
207Pb/235U
(b) 207Pb/206Pb weighted average
data-point error symbols are 1σ
1610
1590
1570
1550
1530
Mean = 1573±12 [0.74%] 95% conf.
Wtd by data-pt errs only, 0 of 11 rej.
MSWD = 0.112, probability = 1.000
(c)
1574.7 ± 19.25 Ma
1580.2 ± 20.3 Ma
(d)
1573.8 ± 20.16 Ma
1578.9 ± 20.02 Ma
(e)
1572 ± 19.84 Ma
1574.3 ± 18.63 Ma
(f)
1574.7 ± 18.63 Ma

Figure 16

Sample Boothby 09-1

(a) $^{207}Pb/^{206}$ Pb weighted average (in biotite)

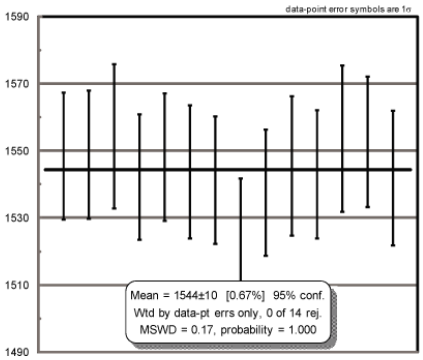

(b) Concordia plot (in biotite)

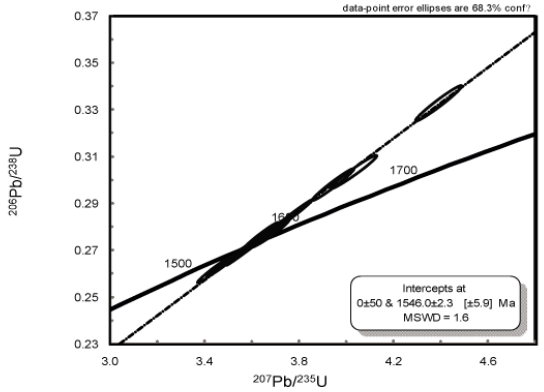

(c) $^{207}Pb/^{206}$ Pb weighted average (in garnet)

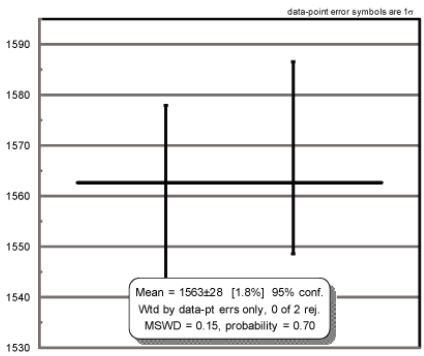

(d) Concordia plot (in garnet)

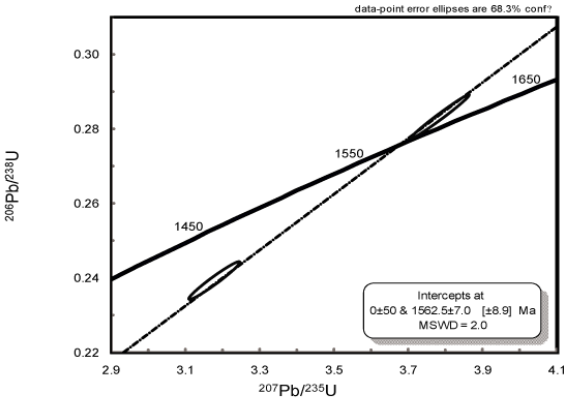

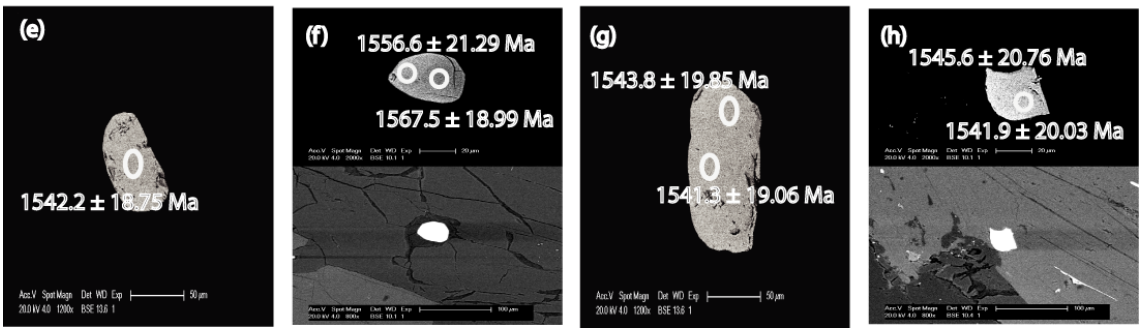

Figure 17

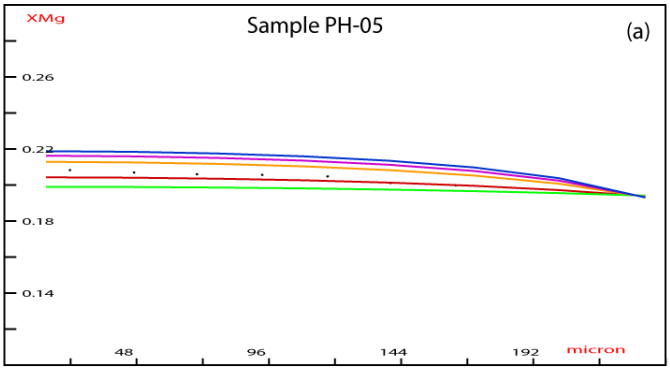
XMg
Sample PH-05
(a)
0.26
0.22
0.18
0.14
48
96
144
192
micron

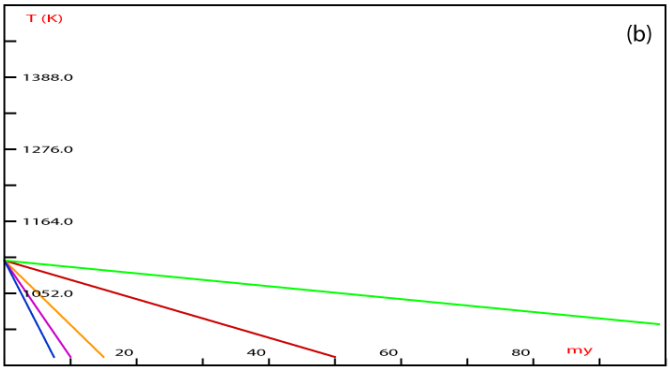
T (K)
(b)
1388.0
1276.0
1164.0
1052.0
20
40
60
80
my

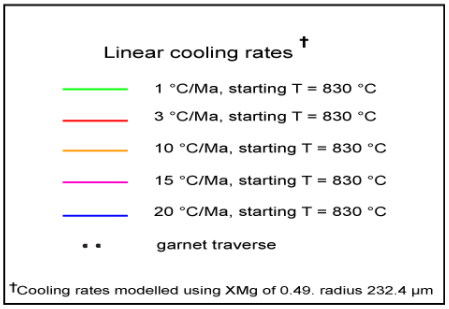
Linear cooling rates †
1 °C/Ma, starting T = 830 °C
3 °C/Ma, starting T = 830 °C
10 °C/Ma, starting T = 830 °C
15 °C/Ma, starting T = 830 °C
20 °C/Ma, starting T = 830 °C
garnet traverse
†Cooling rates modelled using XMg of 0.49. radius 232.4 µm

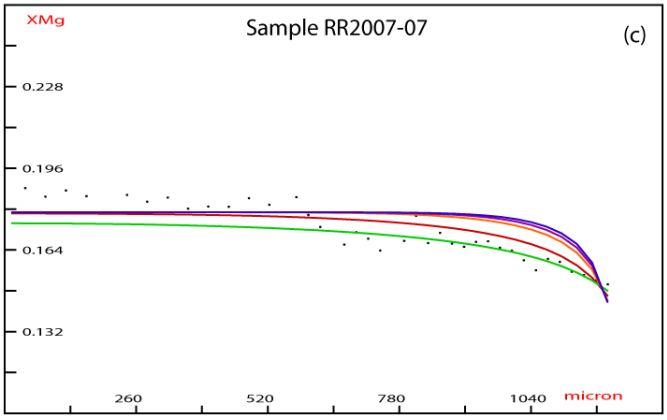
XMg
Sample RR2007-07
(c)
0.228
0.196
0.164
0.132
260
520
780
1040
micron

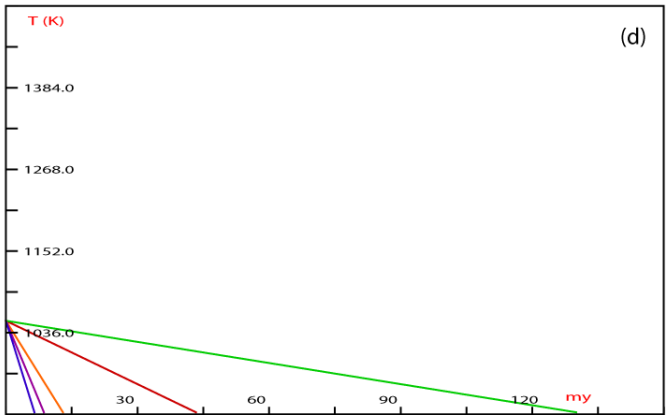
T (K)
(d)
1384.0
1268.0
1152.0
1036.0
30
60
90
120
my

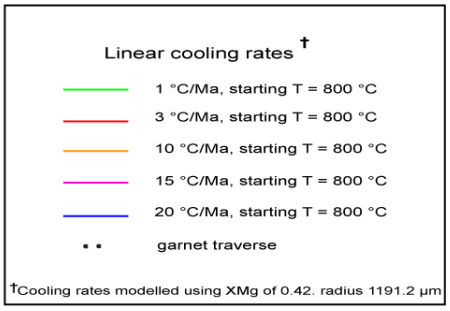
Linear cooling rates †
1 °C/Ma, starting T = 800 °C
3 °C/Ma, starting T = 800 °C
10 °C/Ma, starting T = 800 °C
15 °C/Ma, starting T = 800 °C
20 °C/Ma, starting T = 800 °C
garnet traverse
†Cooling rates modelled using XMg of 0.42. radius 1191.2 µm

Figure 18

12. APPENDICES

Appendix 1 Representative microprobe analysis of minerals from all samples.

	Sample Boothby 09-2A					
	grt rim	grt core	bi	and	mt	ilm (with inclusions)
SiO2	37.35	36.20	35.16	36.84	0.07	2.32
TiO2	0.00	0.00	3.18	0.02	0.11	32.18
Al2O3	20.89	20.43	16.27	58.84	0.38	10.72
Cr2O3	0.03	0.00	0.01	0.07	0.84	0.71
FeO	34.29	36.22	19.66	2.13	86.87	33.79
MnO	0.71	0.96	0.03	0.05	0.00	0.78
MgO	4.72	3.39	10.65	0.61	0.01	0.85
ZnO	0.04	0.05	0.11	0.03	0.00	0.00
CaO	1.47	1.41	0.05	0.05	0.03	0.13
Na2O	0.00	0.01	0.21	0.07	0.00	0.12
K2O	0.00	0.00	9.31	0.09	0.02	0.04
Total	99.49	98.67	94.64	98.81	88.40	81.69
Si	2.99	2.96	2.39	1.01	0.00	0.07
Ti	0.00	0.00	0.16	0.00	0.00	0.69
Al	1.97	1.97	1.30	1.90	0.02	0.36
Cr	0.00	0.00	0.00	0.00	0.03	0.02
Fe3+	-	-	-	0.00	1.94	0.12
Fe2+	2.25	2.35	1.12	0.05	1.00	0.68
Mn	0.05	0.07	0.00	0.00	0.00	0.02
Mg	0.56	0.41	1.08	0.03	0.00	0.04
Zn	0.00	0.00	0.01	0.00	0.00	0.00
Ca	0.13	0.12	0.00	0.00	0.00	0.00
Na	0.00	0.00	0.03	0.00	0.00	0.01
K	0.00	0.00	0.81	0.00	0.00	0.00
Total	7.95	7.88	6.90	3.02	3.00	2.00
XFe*	0.80	0.86	0.51	0.66	1.00	0.96
XFe	0.75	0.80	-	-	-	-
XMg	0.20	0.14	0.49	0.34	0.00	0.04

XFe* = Fe/(Fe+Mg)

XFe = Fe/(Fe+Mg+Ca+Mn)

XMg = Mg/(Fe+Mg)

	Sample Boothby 09-1		
	grt rim	grt core	bi
SiO2	37.22	35.94	35.16
TiO2	0.00	0.06	3.18
Al2O3	20.53	20.73	16.27
Cr2O3	0.04	0.00	0.01
FeO	34.30	34.87	19.66
MnO	0.71	0.70	0.03
MgO	4.85	4.73	10.65
ZnO	0.02	0.00	0.11
CaO	1.43	1.25	0.05
Na2O	0.00	0.01	0.21
K2O	0.00	0.00	9.31
Total	99.10	98.31	94.64
Si	3.00	2.94	2.71
Ti	0.00	0.00	0.18
Al	1.97	2.00	1.48
Cr	0.00	0.00	0.00
Fe2+	2.30	2.38	1.27
Mn2+	0.05	0.05	0.00
Mg	0.56	0.58	1.23
Zn	0.00	0.00	0.01
Ca	0.13	0.11	0.00
Na	0.00	0.00	0.03
K	0.00	0.00	0.92
Total	8.02	8.06	7.83
XFe*	0.80	0.81	0.51
XFe	0.76	0.76	-
XMg	0.20	0.19	0.49

XFe* = Fe/(Fe+Mg)

XFe = Fe/(Fe+Mg+Ca+Mn)

XMg = Mg/(Fe+Mg)

	Sample PH-05							
	grt rim	grt core	crd	sill	ilm	sp	bi	bi (apple green)
SiO2	36.04	36.83	48.34	35.27	0.19	0.00	35.10	35.13
TiO2	0.09	0.07	0.00	0.01	49.26	0.03	4.49	0.05
Al2O3	21.12	21.26	33.15	61.38	0.07	56.82	16.31	19.32
Cr2O3	0.00	0.00	0.03	0.05	0.01	0.61	0.07	0.00
FeO	34.03	34.17	6.36	0.50	44.17	26.80	15.64	17.11
MnO	0.50	0.63	0.01	0.02	0.13	0.04	0.00	0.03
MgO	5.56	5.70	10.24	0.00	0.37	4.28	12.96	12.89
ZnO	0.03	0.00	0.06	0.00	0.10	9.45	0.00	0.00
CaO	0.95	0.83	0.00	0.00	0.03	0.02	0.00	0.00
Na2O	0.01	0.03	0.14	0.00	0.05	0.33	0.12	0.19
K2O	0.01	0.00	0.00	0.00	0.00	0.00	9.63	9.57
Total	98.41	99.59	98.33	97.26	94.45	98.40	94.31	94.29
Si	2.93	2.95	4.94	0.98	0.01	0.00	2.67	2.68
Ti	0.01	0.00	0.00	0.00	0.99	0.00	0.26	0.00
Al	2.02	2.00	3.99	2.01	0.00	1.93	1.46	1.74
Cr	0.00	0.00	0.00	0.00	0.00	0.01	0.00	0.00
Fe3+	-	-	-	0.00	0.02	0.07	-	-
Fe2+	2.31	2.29	0.54	0.01	0.97	0.58	1.00	1.09
Mn	0.03	0.04	0.00	0.00	0.00	0.00	0.00	0.00
Mg	0.67	0.68	1.56	0.00	0.01	0.18	1.47	1.46
Zn	0.00	0.00	0.00	0.00	0.00	0.20	0.00	0.00
Ca	0.08	0.07	0.00	0.00	0.00	0.00	0.00	0.00
Na	0.00	0.00	0.03	0.00	0.00	0.02	0.02	0.03
K	0.00	0.00	0.00	0.00	0.00	0.00	0.93	0.93
Total	8.06	8.05	11.07	3.01	2.01	3.03	7.81	7.93
XFe*	0.77	0.77	0.26	0.98	0.99	0.78	0.40	0.43
XFe	0.75	0.74	-	-	-	-	–	-
XMg	0.23	0.23	0.74	0.02	0.01	0.22	0.60	0.57

XFe* = Fe/(Fe+Mg)

XFe = Fe/(Fe+Mg+Ca+Mn)

XMg = Mg/(Fe+Mg)

	Sample Boothby 09-4D				
	grt rim	grt core	bi	ksp	ilm
SiO2	37.61	37.25	33.41	62.87	0.03
TiO2	0.00	0.01	3.97	0.04	50.60
Al2O3	21.20	20.99	16.65	18.02	0.00
Cr2O3	0.04	0.05	0.08	0.08	0.06
FeO	35.21	35.52	23.11	0.03	45.37
MnO	0.54	0.49	0.01	0.00	0.17
MgO	4.04	3.78	8.05	0.03	0.47
ZnO	0.02	0.01	0.17	0.06	0.00
CaO	1.12	0.89	0.00	0.05	0.00
Na2O	0.00	0.02	0.11	1.74	0.00
K2O	0.01	0.00	9.40	14.34	0.02
Total	99.81	99.00	94.96	97.27	96.74
Si	3.01	3.01	2.63	2.98	0.00
Ti	0.00	0.00	0.23	0.00	1.00
Al	2.00	2.00	1.54	1.01	0.00
Cr	0.00	0.00	0.00	0.00	0.00
Fe3+	-	-	-	-	0.01
Fe2+	2.36	2.40	1.52	0.00	0.96
Mn	0.04	0.03	0.00	0.00	0.00
Mg	0.48	0.46	0.94	0.00	0.02
Zn	0.00	0.00	0.01	0.00	0.00
Ca	0.10	0.08	0.00	0.00	0.00
Na	0.00	0.00	0.02	0.16	0.01
K	0.00	0.00	0.94	0.87	0.00
Total	7.99	7.99	7.84	5.03	2.01
XFe*	0.83	0.84	0.62	0.37	0.98
XFe	0.80	0.81	-	-	-
XMg	0.17	0.16	0.38	0.63	0.02

XFe* = Fe/(Fe+Mg)

XFe = Fe/(Fe+Mg+Ca+Mn)

XMg = Mg/(Fe+Mg)

	Sample RR04B				
	grt rim	grt core	opx rim	opx core	pl
SiO2	37.10	37.08	45.54	45.84	58.92
TiO2	0.03	0.06	0.20	0.16	0.02
Al2O3	21.56	21.68	7.15	7.19	24.97
Cr2O3	0.01	0.00	0.00	0.00	0.02
FeO	30.21	31.02	25.75	26.62	0.01
MnO	0.45	0.46	0.08	0.18	0.01
MgO	8.47	8.27	19.11	18.33	0.00
ZnO	0.06	0.00	0.05	0.09	0.00
CaO	1.23	0.98	0.11	0.14	7.25
Na2O	0.03	0.01	0.03	0.01	7.53
K2O	0.00	0.00	0.02	0.00	0.15
Total	99.42	99.66	98.19	98.74	98.88
Si	2.93	2.92	1.74	1.75	2.66
Ti	0.00	0.00	0.01	0.00	0.00
Al	2.00	2.01	0.32	0.32	1.33
Cr	0.00	0.00	0.00	0.00	0.00
Fe3+	-	-	0.18	0.16	-
Fe2+	1.99	2.04	0.64	0.69	0.00
Mn	0.03	0.03	0.00	0.01	0.00
Mg	1.00	0.97	1.09	1.05	0.00
Zn	0.00	0.00	0.00	0.00	0.00
Ca	0.10	0.08	0.00	0.01	0.35
Na	0.00	0.00	0.00	0.00	0.66
K	0.00	0.00	0.00	0.00	0.01
Total	8.07	8.07	4.00	4.00	2.01
XFe*	0.67	0.68	0.43	0.45	0.93
XFe	0.61	0.63	-	-	-
XMg	0.33	0.32	0.57	0.55	0.07

XFe* = Fe/(Fe+Mg)

XFe = Fe/(Fe+Mg+Ca+Mn)

XMg = Mg/(Fe+Mg)

	Sample RR03				
	grt rim	grt core	bi	crd	mt
SiO2	36.43	37.47	34.48	48.05	0.04
TiO2	0.02	0.03	4.14	0.00	0.00
Al2O3	21.33	21.37	15.71	32.78	0.21
Cr2O3	0.02	0.00	0.01	0.00	0.30
FeO	31.58	31.68	14.52	4.65	88.51
MnO	0.35	0.38	0.00	0.03	0.04
MgO	7.28	7.03	14.13	11.23	0.00
ZnO	0.05	0.00	0.07	0.07	0.15
CaO	1.23	1.01	0.00	0.04	0.00
Na2O	0.01	0.03	0.16	0.00	0.03
K2O	0.01	0.00	9.69	0.00	0.04
Total	98.31	99.00	92.95	96.85	89.31
Si	2.92	2.97	2.66	4.95	0.00
Ti	0.00	0.00	0.24	0.00	0.00
Al	2.02	2.00	1.43	3.98	0.01
Cr	0.00	0.00	0.00	0.00	0.01
Fe3+	-	-	-	-	1.98
Fe2+	2.12	2.10	0.94	0.40	0.99
Mn	0.02	0.03	0.00	0.00	0.00
Mg	0.87	0.83	1.62	1.72	0.00
Zn	0.00	0.00	0.00	0.01	0.00
Ca	0.11	0.09	0.00	0.00	0.00
Na	0.00	0.01	0.02	0.00	0.00
K	0.00	0.00	0.95	0.00	0.00
Total	8.07	8.03	7.87	11.06	3.00
XFe*	0.71	0.72	0.37	0.19	1.00
XFe	0.66	0.68	-	-	-
XMg	0.29	0.28	0.63	0.81	0.00

XFe* = Fe/(Fe+Mg)

XFe = Fe/(Fe+Mg+Ca+Mn)

XMg = Mg/(Fe+Mg)

	Sample RR2007-07					
	grt rim	grt core	bi	crd	ilm	ksp
SiO2	35.98	35.66	34.00	47.54	0.00	62.56
TiO2	0.01	0.00	3.57	0.00	51.76	0.05
Al2O3	21.05	20.93	17.51	32.47	0.00	18.21
Cr2O3	0.02	0.00	0.07	0.00	0.04	0.00
FeO	36.40	36.27	19.56	9.37	45.31	0.03
MnO	0.32	0.30	0.00	0.02	0.09	0.00
MgO	4.00	4.24	9.01	7.97	0.21	0.00
ZnO	0.03	0.03	0.00	0.11	0.00	0.00
CaO	0.53	0.59	0.00	0.01	0.01	0.02
Na2O	0.04	0.03	0.08	0.01	0.04	0.97
K2O	0.01	0.00	9.66	0.03	0.00	15.44
Total	98.38	98.07	93.45	97.53	97.45	97.27
Si	2.95	2.93	2.66	4.97	0.00	2.98
Ti	0.00	0.00	0.21	0.00	1.30	0.00
Al	2.03	2.03	1.62	4.00	0.00	1.02
Cr	0.00	0.00	0.00	0.00	0.00	0.00
Fe3+	-	-	-	-	-0.01	-
Fe2+	2.49	2.49	1.28	0.82	0.64	0.00
Mn	0.02	0.02	0.00	0.00	0.00	0.00
Mg	0.49	0.52	1.05	1.24	0.01	0.00
Zn	0.00	0.00	0.00	0.01	0.00	0.00
Ca	0.05	0.05	0.00	0.00	0.00	0.00
Na	0.01	0.00	0.01	0.00	0.00	0.09
K	0.00	0.00	0.96	0.00	0.00	0.94
Total	8.04	8.06	7.80	11.04	1.93	5.03
XFe*	0.84	0.83	0.55	0.40	0.99	0.99
XFe	0.82	0.81	-	-	-	-
XMg	0.19	0.17	0.45	0.60	0.01	0.01

XFe* = Fe/(Fe+Mg)

XFe = Fe/(Fe+Mg+Ca+Mn)

XMg = Mg/(Fe+Mg)

	Sample Boothby 09-2					
	grt rim	grt core	bi	crd	ksp	and
SiO2	35.65	35.85	34.65	47.78	62.65	38.00
TiO2	0.06	0.02	4.29	0.02	0.00	0.03
Al2O3	20.90	20.94	16.09	32.37	21.30	63.17
Cr2O3	0.00	0.06	0.10	0.00	0.06	0.00
FeO	37.18	37.07	18.14	10.79	0.13	0.96
MnO	0.58	0.63	0.00	0.04	0.03	0.00
MgO	3.77	3.92	11.86	7.50	0.03	0.01
ZnO	0.00	0.00	0.00	0.05	0.01	0.00
CaO	1.05	1.01	0.01	0.03	2.98	0.01
Na2O	0.00	0.03	0.09	0.04	6.05	0.01
K2O	0.00	0.00	10.02	0.00	4.81	0.04
Total	99.20	99.57	95.27	98.61	98.09	102.22
Si	2.92	2.92	2.65	4.97	2.86	1.01
Ti	0.00	0.00	0.25	0.00	0.00	0.00
Al	2.01	2.01	1.45	3.97	1.15	1.97
Cr	0.00	0.00	0.01	0.00	0.00	0.00
Fe3+	-	-	-	-	-	0.00
Fe2+	2.54	2.53	1.16	0.94	0.01	0.00
Mn2+	0.04	0.04	0.00	0.00	0.00	0.00
Mg	0.46	0.48	1.35	1.16	0.00	0.00
Zn	0.00	0.00	0.00	0.00	0.00	0.00
Ca	0.09	0.09	0.00	0.00	0.15	0.00
Na	0.00	0.00	0.01	0.01	0.53	0.00
K	0.00	0.00	0.98	0.00	0.28	0.00
Total	8.07	8.07	7.87	11.05	4.97	3.01
XFe*	0.85	0.84	0.46	0.39	0.74	0.99
XFe	0.81	0.81	-	-	-	-
XMg	0.15	0.16	0.54	0.61	0.17	0.01

XFe* = Fe/(Fe+Mg)

XFe = Fe/(Fe+Mg+Ca+Mn)

XMg = Mg/(Fe+Mg)

Appendix 2 All garnet profiles

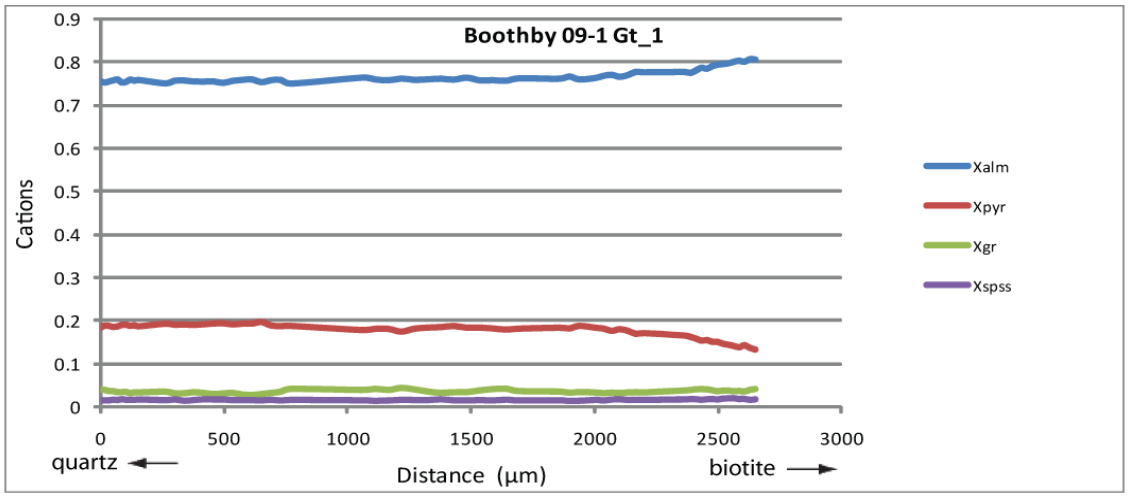

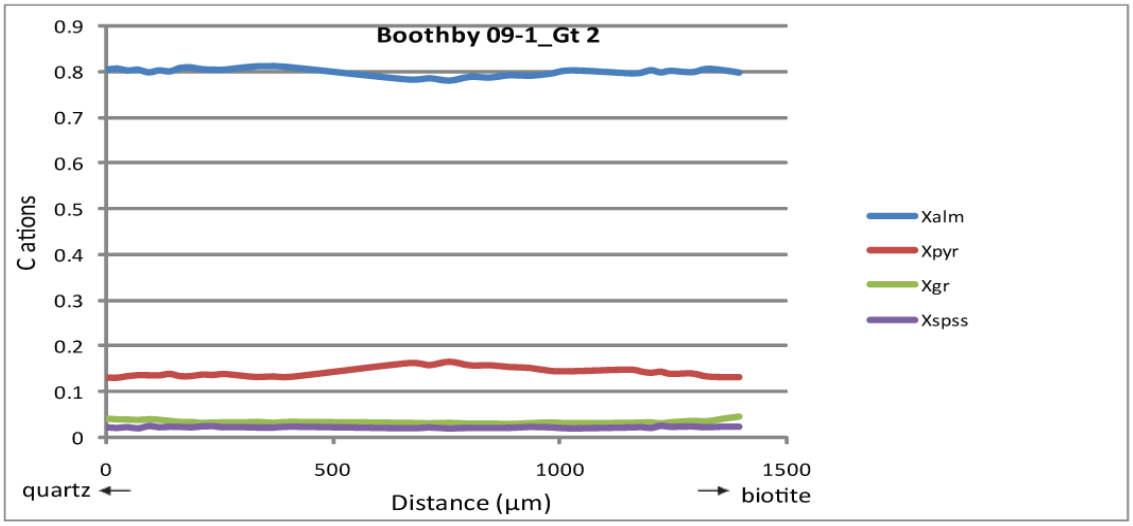

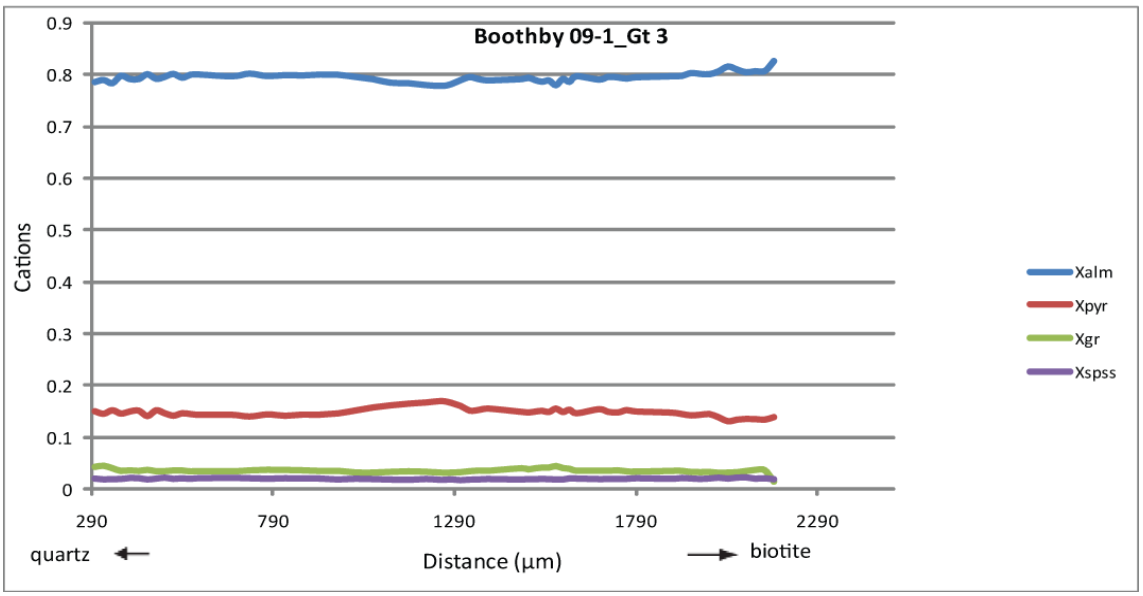

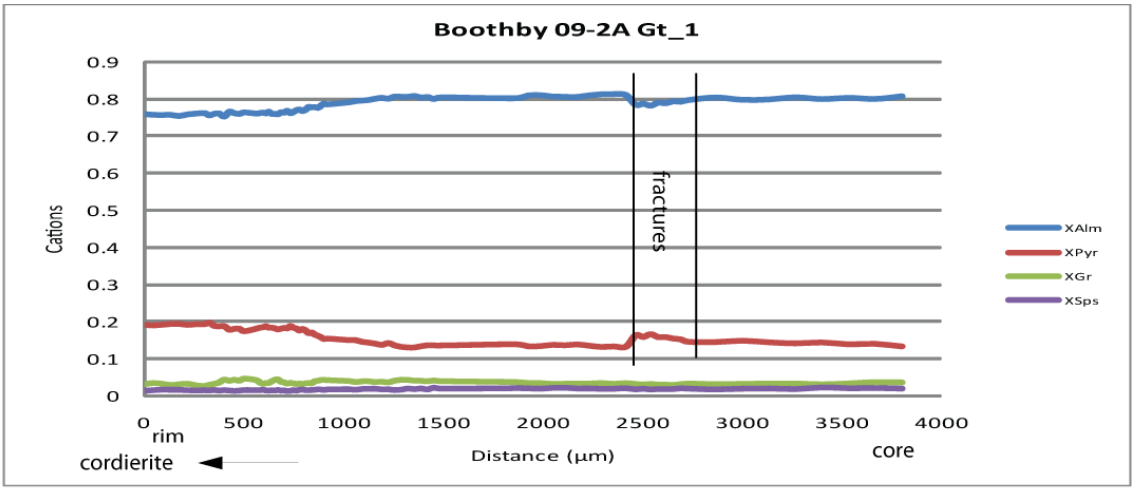
Boothby 09-2A Gt_1
Cations
fractures
XAlm
XPyr
XGr
XSps
0 rim
cordierite
Distance (µm)
core

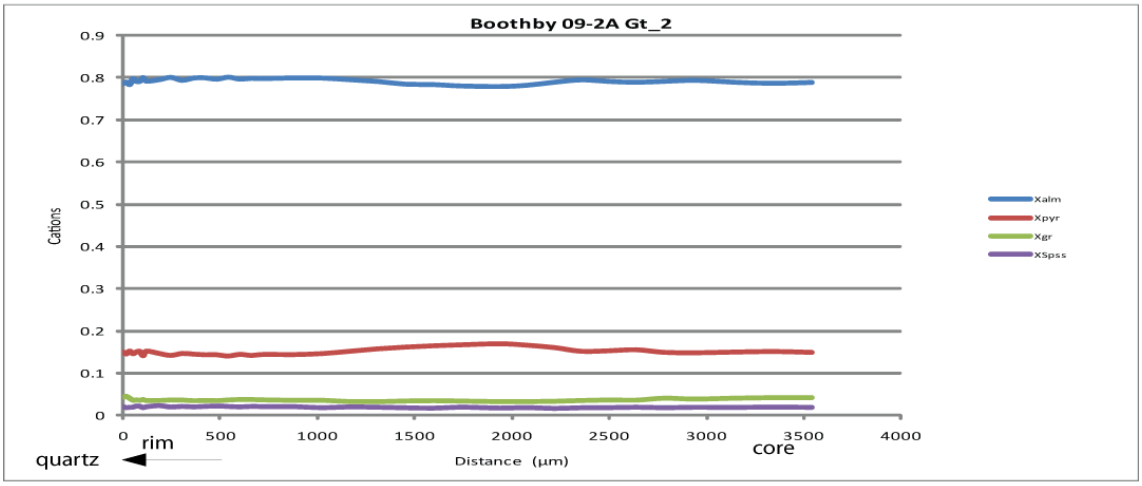
Boothby 09-2A Gt_2
Cations
Xalm
Xpyr
Xgr
XSpss
rim
quartz
Distance (µm)
core

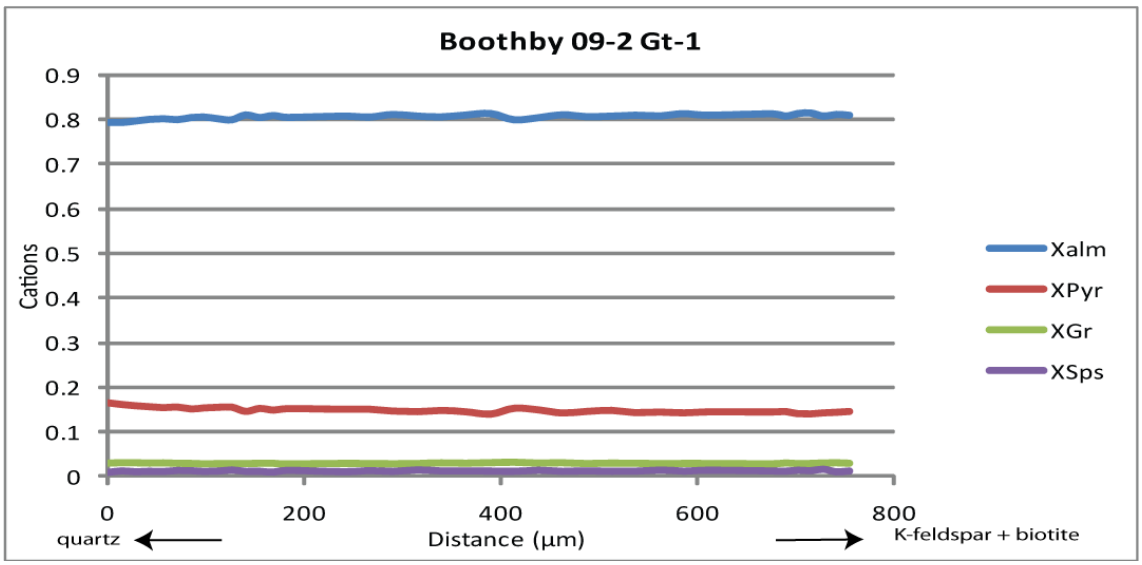
Boothby 09-2 Gt-1
Cations
Xalm
XPyr
XGr
XSps
quartz
Distance (µm)
K-feldspar + biotite

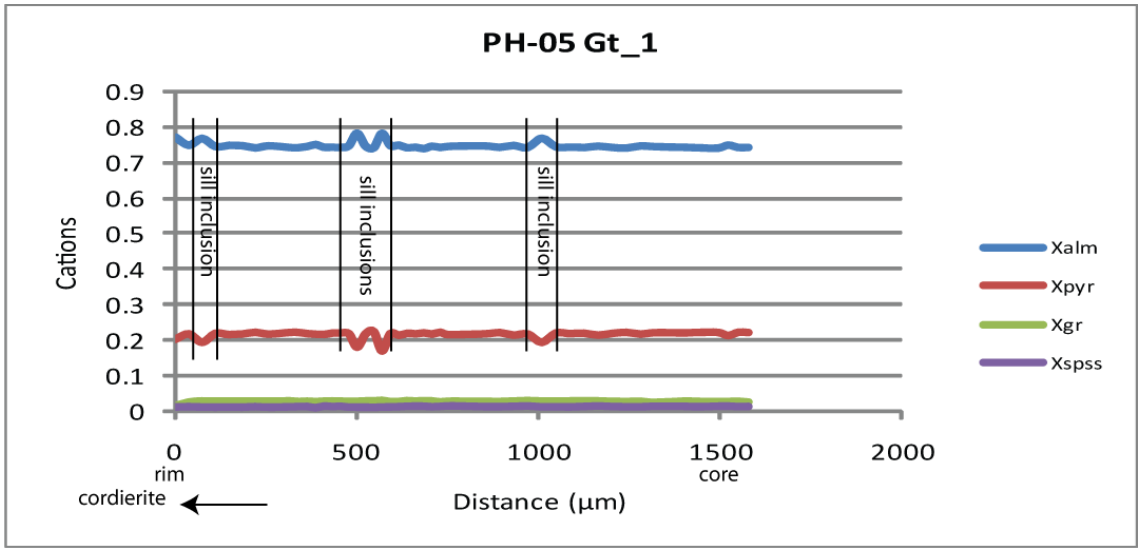
PH-05 Gt_1
Cations
0.9
0.8
0.7
0.6
0.5
0.4
0.3
0.2
0.1
0
sill inclusion
sill inclusions
sill inclusion
0
500
1000
1500
2000
rim
core
cordierite
Distance (µm)
Xalm
Xpyr
Xgr
Xspss

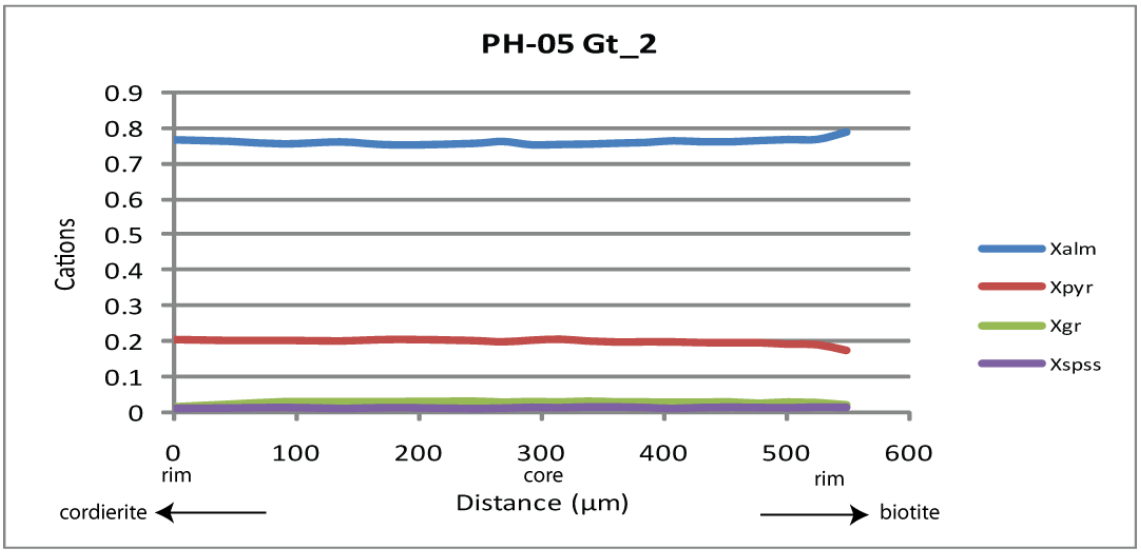
PH-05 Gt_2
Cations
0.9
0.8
0.7
0.6
0.5
0.4
0.3
0.2
0.1
0
0
100
200
300
400
500
600
rim
core
rim
cordierite
Distance (µm)
biotite
Xalm
Xpyr
Xgr
Xspss

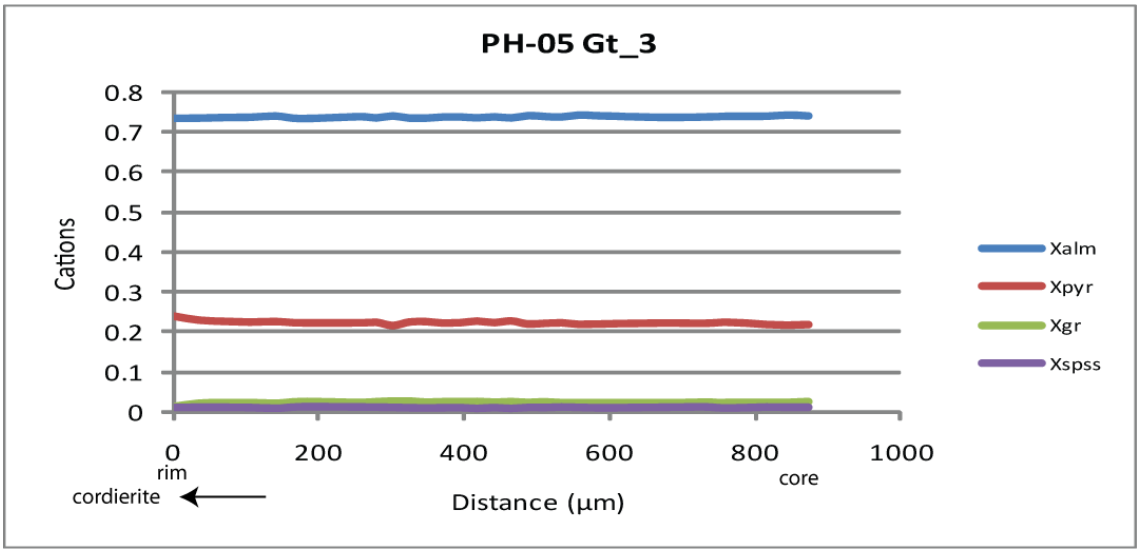
PH-05 Gt_3
Cations
0.8
0.7
0.6
0.5
0.4
0.3
0.2
0.1
0
0
200
400
600
800
1000
rim
core
cordierite
Distance (µm)
Xalm
Xpyr
Xgr
Xspss

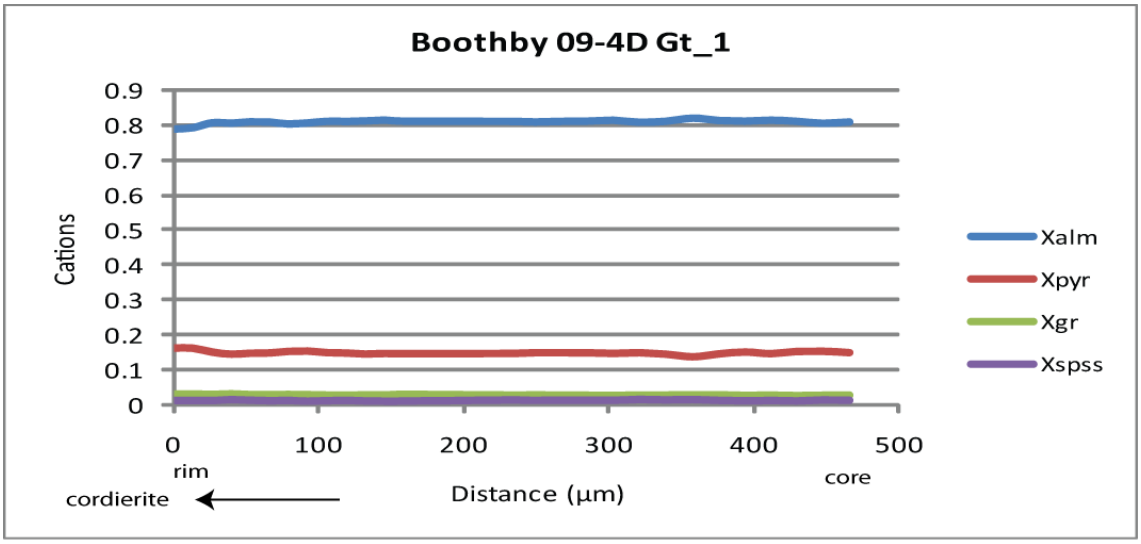
Boothby 09-4D Gt_1
Cations
0.9
0.8
0.7
0.6
0.5
0.4
0.3
0.2
0.1
0
0
100
200
300
400
500
rim
core
cordierite
Distance (µm)
Xalm
Xpyr
Xgr
Xspss

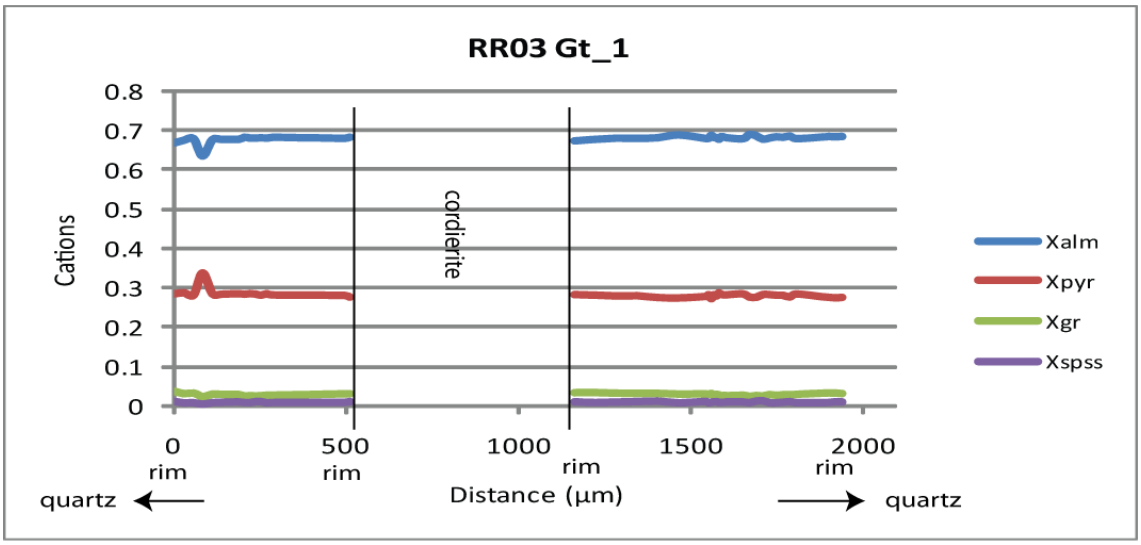
RR03 Gt_1
Cations
0.8
0.7
0.6
0.5
0.4
0.3
0.2
0.1
0
cordierite
0
500
1000
1500
2000
rim
rim
rim
rim
quartz
quartz
Distance (µm)
Xalm
Xpyr
Xgr
Xspss

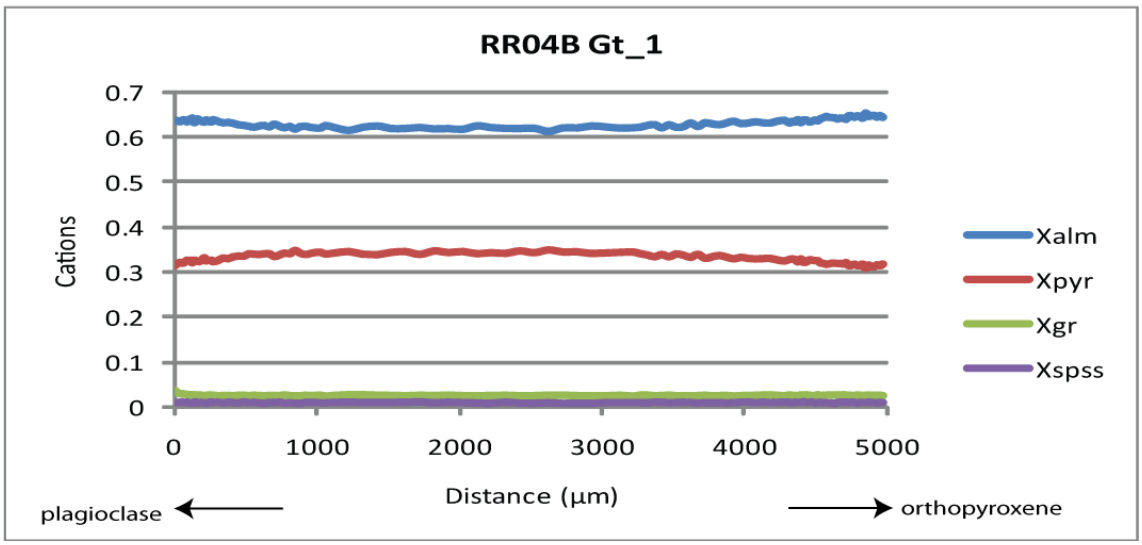
RR04B Gt_1
Cations
0.7
0.6
0.5
0.4
0.3
0.2
0.1
0
0
1000
2000
3000
4000
5000
plagioclase
orthopyroxene
Distance (µm)
Xalm
Xpyr
Xgr
Xspss

Appendix 3 Representative output file from *A-X*

Sample Boothby 09-1

```
Calculations for P = 5.5 kbar and T =  800°C
_____________________________________________________________________________

g untitled
  2-site mixing + Regular solution gammas
  Ferric from:  Cation Sum = 8 for 12 oxygens
  W: py.alm=2.5, gr.py=33, py.andr=73, alm.andr=60, spss.andr=60 kJ

oxide    wt % cations              activity         ±sd    ±%

 SiO2   34.65   2.894         py      0.0054     0.00222    41
 TiO2    0.01   0.001         gr    0.000084   0.0000463    55
Al2O3   19.94   1.963        alm        0.39       0.059    15
Cr2O3    0.00   0.000       spss    0.000012   0.0000066    57
Fe2O3    3.95   0.248       andr           -           -     -
  FeO   32.02   2.237
  MnO    0.99   0.070
  MgO    3.78   0.470
  CaO    1.30   0.117
 Na2O    0.00   0.001
  K2O    0.00   0.000

totals  96.64   8.000


_____________________________________________________________________________

bi untitled
  Al-M1 ordered, site-mixing model  + macroscopic RS gammas: (ann,
phl, east, obi)
  Ferric from:  Tet + Oct cation sum = 6.9 for 11 oxygens. Max Ratio =
0.15
  SF model parameters: Wpa=9, Wpe=10, Wpo=3, Wao=6, Wae=-1, Woe=10
(kJ)

oxide    wt % cations              activity         ±sd    ±%

 SiO2   35.13   2.723        phl       0.055      0.0127    23
 TiO2    3.16   0.184        ann       0.058      0.0131    23
Al2O3   16.30   1.490       east       0.032      0.0089    28
Cr2O3    0.05   0.003
Fe2O3    0.00   0.000
  FeO   19.15   1.241
  MnO    0.00   0.000
  MgO   10.58   1.222
  CaO    0.01   0.001
 Na2O    0.25   0.037
  K2O    9.37   0.927

totals  94.01   7.829
```

Sample Boothby 09-2

Calculations for P = 5.5 kbar and T = 800°C

---

g untitled
2-site mixing + Regular solution gammas
Ferric from: Cation Sum = 8 for 12 oxygens
W: py.alm=2.5, gr.py=33, py.andr=73, alm.andr=60, spss.andr=60 kJ

oxide	wt %	cations		activity	±sd	±%
SiO2	35.97	2.911	py	0.0060	0.00240	40
TiO2	0.05	0.003	gr	0.000042	0.0000233	56
Al2O3	20.90	1.994	alm	0.43	0.065	15
Cr2O3	0.02	0.001	spss	0.0000037	0.0000021	58
Fe2O3	2.91	0.177	andr	-	-	-
FeO	33.91	2.295				
MnO	0.69	0.047				
MgO	4.01	0.484				
CaO	1.01	0.088				
Na2O	0.00	0.000				
K2O	0.00	0.000				
totals	99.48	8.000				

---

bi untitled
Al-M1 ordered, site-mixing model + macroscopic RS gammas: (ann, phl, east, obi)
Ferric from: Tet + Oct cation sum = 6.9 for 11 oxygens. Max Ratio = 0.15
SF model parameters: Wpa=9, Wpe=10, Wpo=3, Wao=6, Wae=-1, Woe=10 (kJ)

oxide	wt %	cations		activity	±sd	±%
SiO2	34.65	2.653	phl	0.070	0.0145	21
TiO2	4.29	0.247	ann	0.048	0.0116	24
Al2O3	16.09	1.452	east	0.028	0.0081	29
Cr2O3	0.10	0.006				
Fe2O3	0.00	0.000				
FeO	18.14	1.161				
MnO	0.00	0.000				
MgO	11.86	1.353				
CaO	0.01	0.001				
Na2O	0.09	0.014				
K2O	10.02	0.980				
totals	95.26	7.867				

Sample Boothby 09-2A

Calculations for P = 5.5 kbar and T = 800°C

---

g untitled
2-site mixing + Regular solution gammas
Ferric from: Cation Sum = 8 for 12 oxygens
W: py.alm=2.5, gr.py=33, py.andr=73, alm.andr=60, spss.andr=60 kJ

oxide	wt %	cations		activity	±sd	±%
SiO2	35.73	2.944	py	0.0062	0.00247	40
TiO2	0.00	0.000	gr	0.000067	0.0000371	55
Al2O3	20.27	1.969	alm	0.41	0.062	15
Cr2O3	0.00	0.000	spss	0.0000063	0.0000036	58
Fe2O3	2.43	0.150	andr	-	-	-
FeO	32.93	2.269				
MnO	0.82	0.057				
MgO	4.05	0.497				
CaO	1.20	0.106				
Na2O	0.04	0.006				
K2O	0.01	0.001				
totals	97.47	8.000				

---

bi untitled
Al-M1 ordered, site-mixing model + macroscopic RS gammas: (ann, phl, east, obi)
Ferric from: Tet + Oct cation sum = 6.9 for 11 oxygens. Max Ratio = 0.15
SF model parameters: Wpa=9, Wpe=10, Wpo=3, Wao=6, Wae=-1, Woe=10 (kJ)

oxide	wt %	cations		activity	±sd	±%
SiO2	35.16	2.716	phl	0.054	0.0126	23
TiO2	3.18	0.184	ann	0.062	0.0136	22
Al2O3	16.27	1.481	east	0.030	0.0086	29
Cr2O3	0.01	0.001				
Fe2O3	0.00	0.000				
FeO	19.66	1.270				
MnO	0.03	0.002				
MgO	10.65	1.226				
CaO	0.05	0.004				
Na2O	0.21	0.031				
K2O	9.31	0.918				
totals	94.53	7.833				

Sample Boothby 09-4D

Calculations for P = 5.5 kbar and T = 800°C

---

bi untitled
Al-M1 ordered, site-mixing model + macroscopic RS gammas: (ann, phl, east, obi)
Ferric from: Tet + Oct cation sum = 6.9 for 11 oxygens. Max Ratio = 0.15
SF model parameters: Wpa=9, Wpe=10, Wpo=3, Wao=6, Wae=-1, Woe=10 (kJ)

oxide	wt %	cations		activity	±sd	±%
SiO2	34.19	2.638	phl	0.038	0.0101	26
TiO2	2.78	0.161	ann	0.076	0.0151	20
Al2O3	17.44	1.586	east	0.030	0.0086	28
Cr2O3	0.04	0.003				
Fe2O3	0.70	0.041				
FeO	21.36	1.378				
MnO	0.05	0.004				
MgO	9.48	1.090				
CaO	0.00	0.000				
Na2O	0.12	0.017				
K2O	9.70	0.956				
totals	95.86	7.873				

---

g untitled
2-site mixing + Regular solution gammas
Ferric from: Cation Sum = 8 for 12 oxygens
W: py.alm=2.5, gr.py=33, py.andr=73, alm.andr=60, spss.andr=60 kJ

oxide	wt %	cations		activity	±sd	±%
SiO2	37.67	3.011	py	0.0044	0.00186	42
TiO2	0.00	0.000	gr	0.000038	0.0000214	56
Al2O3	21.11	1.990	alm	0.51	0.077	15
Cr2O3	0.00	0.000	spss	0.0000019	0.00000113	59
Fe2O3	0.00	0.000	andr	-	-	-
FeO	36.16	2.417				
MnO	0.56	0.038				
MgO	3.77	0.449				
CaO	1.00	0.086				
Na2O	0.04	0.006				
K2O	0.01	0.001				
totals	100.32	7.997				

Sample PH-05

Calculations for P = 5.5 kbar and T = 800°C

---

g untitled
2-site mixing + Regular solution gammas
Ferric from: Cation Sum = 8 for 12 oxygens
W: py.alm=2.5, gr.py=33, py.andr=73, alm.andr=60, spss.andr=60 kJ

oxide	wt %	cations		activity	±sd	±%
SiO2	36.45	2.888	py	0.015	0.00504	34
TiO2	0.00	0.000	gr	0.000030	0.0000166	56
Al2O3	22.88	2.137	alm	0.34	0.051	15
Cr2O3	0.06	0.004	spss	0.0000022	0.00000128	58
Fe2O3	1.42	0.085	andr	-	-	-
FeO	31.90	2.113				
MnO	0.60	0.040				
MgO	5.57	0.658				
CaO	0.86	0.073				
Na2O	0.00	0.000				
K2O	0.02	0.002				
totals	99.76	8.000				

---

bi untitled
Al-M1 ordered, site-mixing model + macroscopic RS gammas: (ann, phl, east, obi)
Ferric from: Tet + Oct cation sum = 6.9 for 11 oxygens. Max Ratio = 0.15
SF model parameters: Wpa=9, Wpe=10, Wpo=3, Wao=6, Wae=-1, Woe=10 (kJ)

oxide	wt %	cations		activity	±sd	±%
SiO2	35.10	2.672	phl	0.088	0.0163	18
TiO2	4.49	0.257	ann	0.028	0.0082	29
Al2O3	16.31	1.463	east	0.039	0.0102	26
Cr2O3	0.07	0.004				
Fe2O3	0.00	0.000				
FeO	15.64	0.996				
MnO	0.00	0.000				
MgO	12.96	1.470				
CaO	0.00	0.000				
Na2O	0.12	0.017				
K2O	9.63	0.936				
totals	94.32	7.815				

Sample RR03

Calculations for P = 5.5 kbar and T = 800°C

---

g untitled
2-site mixing + Regular solution gammas
Ferric from: Cation Sum = 8 for 12 oxygens
W: py.alm=2.5, gr.py=33, py.andr=73, alm.andr=60, spss.andr=60 kJ

oxide	wt %	cations		activity	±sd	±%
SiO2	36.43	2.904	py	0.032	0.0089	28
TiO2	0.00	0.000	gr	0.000054	0.0000299	56
Al2O3	21.35	2.006	alm	0.26	0.039	15
Cr2O3	0.00	0.000	spss	-	-	-
Fe2O3	3.10	0.186	andr	-	-	-
FeO	28.98	1.932				
MnO	0.36	0.025				
MgO	7.28	0.865				
CaO	0.97	0.083				
Na2O	0.00	0.000				
K2O	0.00	0.000				
totals	98.47	8.000				

---

bi untitled
Al-M1 ordered, site-mixing model + macroscopic RS gammas: (ann, phl, east, obi)
Ferric from: Tet + Oct cation sum = 6.9 for 11 oxygens. Max Ratio = 0.15
SF model parameters: Wpa=9, Wpe=10, Wpo=3, Wao=6, Wae=-1, Woe=10 (kJ)

oxide	wt %	cations		activity	±sd	±%
SiO2	34.48	2.661	phl	0.123	0.0186	15
TiO2	4.14	0.240	ann	0.023	0.0072	31
Al2O3	15.71	1.429	east	0.035	0.0096	27
Cr2O3	0.01	0.001				
Fe2O3	0.00	0.000				
FeO	14.52	0.937				
MnO	0.00	0.000				
MgO	14.13	1.625				
CaO	0.00	0.000				
Na2O	0.16	0.024				
K2O	9.69	0.955				
totals	92.84	7.873				

Sample RR2007-07

Calculations for P = 5.5 kbar and T = 800°C

---

g untitled
2-site mixing + Regular solution gammas
Ferric from: Cation Sum = 8 for 12 oxygens
W: py.alm=2.5, gr.py=33, py.andr=73, alm.andr=60, spss.andr=60 kJ

oxide	wt %	cations		activity	±sd	±%
SiO2	36.45	2.933	py	0.0087	0.00329	38
TiO2	0.08	0.005	gr	0.0000080	0.0000046	58
Al2O3	21.21	2.012	alm	0.45	0.068	15
Cr2O3	0.00	0.000	spss	-	-	-
Fe2O3	1.85	0.112	andr	-	-	-
FeO	34.33	2.311				
MnO	0.26	0.018				
MgO	4.68	0.561				
CaO	0.56	0.049				
Na2O	0.00	0.000				
K2O	0.00	0.000				
totals	99.43	8.000				

---

bi untitled
Al-M1 ordered, site-mixing model + macroscopic RS gammas: (ann, phl, east, obi)
Ferric from: Tet + Oct cation sum = 6.9 for 11 oxygens. Max Ratio = 0.15
SF model parameters: Wpa=9, Wpe=10, Wpo=3, Wao=6, Wae=-1, Woe=10 (kJ)

oxide	wt %	cations		activity	±sd	±%
SiO2	34.00	2.663	phl	0.037	0.0098	27
TiO2	3.57	0.210	ann	0.061	0.0135	22
Al2O3	17.51	1.617	east	0.033	0.0091	28
Cr2O3	0.07	0.004				
Fe2O3	0.00	0.000				
FeO	19.56	1.281				
MnO	0.00	0.000				
MgO	9.01	1.052				
CaO	0.00	0.000				
Na2O	0.08	0.012				
K2O	9.66	0.966				
totals	93.46	7.805				

Sample RR04B

Calculations for P = 5.5 kbar and T = 800°C

---

opx untitled
M1-M2 site mixing. Projected into en-fs-mgts-di system for gammas
Ferric from: Cation Sum = 4 for 6 oxygens
W: fs.en=1.0, en.mgts=0,en.di=30, mgts.di=30, fs.mgts=1.0, fs.di=28 kJ

oxide	wt %	cations		activity	±sd	±%
SiO2	45.53	1.744	en	0.27	0.0275	10
TiO2	0.09	0.003	fs	0.12	0.0207	17
Al2O3	7.31	0.330	mgts	0.045	0.0111	25
Cr2O3	0.00	0.000				
Fe2O3	6.00	0.173				
FeO	21.59	0.692				
MnO	0.17	0.005				
MgO	18.38	1.049				
CaO	0.14	0.006				
Na2O	0.01	0.001				
K2O	0.00	0.000				
totals	99.22	4.002				

---

g untitled
2-site mixing + Regular solution gammas
Ferric from: Cation Sum = 8 for 12 oxygens
W: py.alm=2.5, gr.py=33, py.andr=73, alm.andr=60, spss.andr=60 kJ

oxide	wt %	cations		activity	±sd	±%
SiO2	36.93	2.889	py	0.045	0.0112	25
TiO2	0.01	0.000	gr	0.000061	0.0000336	55
Al2O3	21.53	1.985	alm	0.20	0.030	15
Cr2O3	0.00	0.000	spss	0.0000009	0.00000053	59
Fe2O3	4.07	0.240	andr	-	-	-
FeO	27.32	1.788				
MnO	0.46	0.030				
MgO	8.41	0.981				
CaO	1.00	0.084				
Na2O	0.02	0.003				
K2O	0.00	0.000				
totals	99.75	8.000				

Appendix 4 Pressure and Temperature estimates calculated from end-member reactions.

Sample Boothby 09-1

```
no of reactions = 1, no of intersections = 0
1)  py + ann = alm + phl
Thermodynamics of reactions (0 = a + bT + cP + RT ln K)
linearised at T = 650, P = 6.0
(a, b and c includes fluid fugacities; ln K includes x(CO2), x(H2O))
            a   sd(a)         b        c     ln_K sd(ln_K)
1      -53.70    0.96   0.02353   -0.292    4.116    0.794
Temperatures in the range 400 <-> 900°C;
uncertainties at or near 6.0 kbars
T°C     4.0  4.4  4.8  5.2  5.6  6.0  6.4  6.8  7.2  7.6  8.0  sdT  sdP

1       677  679  681  683  685  687  689  691  693  695  697  111   22
```

Sample Boothby 09-2

```
no of reactions = 1, no of intersections = 0
1)  py + ann = alm + phl
Thermodynamics of reactions (0 = a + bT + cP + RT ln K)
linearised at T = 600, P = 7.0
(a, b and c includes fluid fugacities; ln K includes x(CO2), x(H2O))
            a   sd(a)         b        c     ln_K sd(ln_K)
1      -53.79    0.96   0.02362   -0.289    3.754    0.549
Temperatures in the range 200 <-> 1000°C;
uncertainties at or near 7.0 kbars
T°C     5.0  5.4  5.8  6.2  6.6  7.0  7.4  7.8  8.2  8.6  9.0  sdT  sdP

1       735  737  739  741  743  745  748  750  752  754  756   87   16
```

Sample Boothby 09-2A

```
no of reactions = 1, no of intersections = 0
1)  py + ann = alm + phl
Thermodynamics of reactions (0 = a + bT + cP + RT ln K)
linearised at T = 600, P = 7.0
(a, b and c includes fluid fugacities; ln K includes x(CO2), x(H2O))
           a   sd(a)         b        c     ln_K sd(ln_K)
1      -53.79    0.96   0.02362   -0.289    4.319    0.544
Temperatures in the range 200 <-> 1000°C;
uncertainties at or near 7.0 kbars
T°C     5.0  5.4  5.8  6.2  6.6  7.0  7.4  7.8  8.2  8.6  9.0  sdT  sdP

1       655  657  659  661  663  665  667  669  671  673  675   73   15
```

Sample Boothby 09-4D

```
no of reactions = 1, no of intersections = 0
1)  phl + alm = ann + py
Thermodynamics of reactions (0 = a + bT + cP + RT ln K)
linearised at T = 600, P = 7.0
(a, b and c includes fluid fugacities; ln K includes x(CO2), x(H2O))
            a   sd(a)         b        c     ln_K sd(ln_K)
1       53.79    0.96  -0.02362    0.289   -3.403    0.568
Temperatures in the range 200 <-> 1000°C;
uncertainties at or near 7.0 kbars
T°C     5.0  5.4  5.8  6.2  6.6  7.0  7.4  7.8  8.2  8.6  9.0  sdT  sdP

1       792  794  796  799  801  803  805  808  810  812  815  101   17
```

Sample PH-05

```
no of reactions = 1, no of intersections = 0
1)  py + ann = alm + phl
Thermodynamics of reactions (0 = a + bT + cP + RT ln K)
linearised at T = 600, P = 7.0
(a, b and c includes fluid fugacities; ln K includes x(CO2), x(H2O))
            a   sd(a)         b        c     ln_K sd(ln_K)
1      -53.79    0.96   0.02362   -0.289    4.410    0.504
Temperatures in the range 200 <-> 1000°C;
uncertainties at or near 7.0 kbars
T°C     5.0  5.4  5.8  6.2  6.6  7.0  7.4  7.8  8.2  8.6  9.0  sdT  sdP

1       643  645  647  649  651  653  655  657  659  661  663   66   14
```

Sample RR03

```
no of reactions = 1, no of intersections = 0
1)  py + ann = alm + phl
Thermodynamics of reactions (0 = a + bT + cP + RT ln K)
linearised at T = 600, P = 7.0
(a, b and c includes fluid fugacities; ln K includes x(CO2), x(H2O))
            a   sd(a)         b        c     ln_K sd(ln_K)
1      -53.79    0.96   0.02362   -0.289    3.710    0.462
Temperatures in the range 200 <-> 1000°C;
uncertainties at or near 7.0 kbars
T°C     5.0  5.4  5.8  6.2  6.6  7.0  7.4  7.8  8.2  8.6  9.0  sdT  sdP

1       741  744  746  748  750  752  755  757  759  761  763   75   14
```

Sample RR04B

```
no of reactions = 1, no of intersections = 0
1)  3en + 2alm = 3fs + 2py
Thermodynamics of reactions (0 = a + bT + cP + RT ln K)
linearised at T = 700, P = 6.5
(a, b and c includes fluid fugacities; ln K includes x(CO2), x(H2O))
            a   sd(a)         b        c     ln_K sd(ln_K)
1       58.03    1.47  -0.01958    0.736   -5.458    1.200
Temperatures in the range 500 <-> 900°C;
uncertainties at or near 6.5 kbars
T°C     4.0  4.5  5.0  5.5  6.0  6.5  7.0  7.5  8.0  8.5  9.0  sdT  sdP

1       666  672  677  683  688  694  700  705  711  717  722  150   13
```

Sample RR2007-07

```
no of reactions = 1, no of intersections = 0
1)  py + ann = alm + phl
Thermodynamics of reactions (0 = a + bT + cP + RT ln K)
linearised at T = 600, P = 7.0
(a, b and c includes fluid fugacities; ln K includes x(CO2), x(H2O))
            a   sd(a)         b        c     ln_K sd(ln_K)
1      -53.79    0.96   0.02362   -0.289    3.389    0.532
Temperatures in the range 200 <-> 1000°C;
uncertainties at or near 7.0 kbars
T°C     5.0  5.4  5.8  6.2  6.6  7.0  7.4  7.8  8.2  8.6  9.0  sdT  sdP
1       794  796  799  801  803  806  808  810  813  815  817
```

Appendix 5 Raw data from Gamma Ray Spectrometer analyses.

Assay#	rock type	K	Th	U
131	sill-bearing leucogneiss	1.40	29.20	9.90
132	sill-bearing leucogneiss	2.90	37.10	5.10
149	crd-bearing pelite	2.30	27.30	7.30
157	crd-bearing pelite (calc-silicate assoc)	3.40	61.90	5.90
158	crd-bearing pelite (calc-silicate assoc)	3.50	26.30	5.40
159	crd melt restite patch	1.10	71.10	20.80
160	crd-bearing pelite (calc-silicate assoc)	3.90	30.80	5.10
161	crd-bearing pelite (calc-silicate assoc)	3.50	32.00	6.80
162	crd-bearing pelite (calc-silicate assoc)	2.90	86.10	10.20
163	bi replacement of crd melt restite	5.20	225.80	22.80
164	crd-oa-sp pod in pelite	0.70	27.00	7.50
165	crd-oa-sp pod in pelite	0.50	33.10	7.30
166	crd-oa-sp pod in pelite	0.50	34.30	7.70
167	crd-bearing pelite (calc-silicate assoc)	2.50	36.50	4.70
168	crd-bearing pelite (calc-silicate assoc)	3.80	31.40	6.40
169	crd melt restite patch	1.00	272.80	31.60
170	crd melt restite patch	1.10	140.50	15.90
171	crd melt restite patch	1.70	93.10	13.00
172	crd-bearing pelite (calc-silicate assoc)	3.00	36.80	7.00
173	crd-bearing pelite (calc-silicate assoc)	2.90	28.80	5.70
174	crd-bearing pelite (calc-silicate assoc)	3.90	30.80	6.40
184	sill-bearing leucogneiss	1.90	30.80	6.10
185	sill-bearing leucogneiss	2.10	27.40	11.90
186	bedded crd-sill gneiss	3.20	27.80	6.20
187	Crd-sill bedded pelite	2.80	28.60	6.20
188	Crd-sill bedded pelite(slightly more psammitic)	2.70	30.90	9.20
189	Pegmatite- bi+qtz+plag	4.40	38.90	6.40
190	Crd-sill bedded pelite	2.60	25.60	6.20
191	sill leucogneiss	2.10	24.60	4.50
192	sill leucogneiss	1.30	11.20	6.40
193	sill leucogneiss	1.60	14.00	7.10
194	sill leucogneiss	2.00	21.90	9.30
195	crd-sill rich pelite	5.50	49.10	11.00
196	crd-sill rich pelite	3.30	30.60	8.20
197	crd-sill rich pelite	3.30	28.50	5.40
198	crd-sill rich pelite (on the margin of shear zone)	1.90	23.80	6.80
199	crd-sill rich pelite (outside shear zone)	3.40	32.20	7.10
200	crd-sill rich (outside shear zone)	2.40	28.10	5.50
201	musc+bi schist (shear zone)	3.00	29.20	7.90
202	musc+bi schist (shear zone)	3.40	29.50	6.00
203	musc+bi schist (shear zone)	2.90	38.20	7.20
204	crd-sill rich pelite	2.80	23.30	5.80
205	musc+bi schist (shear zone)	2.80	35.20	9.30
206	musc+bi schist (shear zone)	5.00	33.40	8.80
207	crd-sill bedded pelite	3.00	34.30	11.10
208	crd-sill bedded pelite (potentially more migmatisation and/or melt retention	2.80	32.60	12.00

209	crd-sill bedded pelite (migmatite- change in rocks from shear zone- more structurally altered)	4.30	31.30	5.10
210	crd-sill migmatised pelite	3.20	24.30	6.30
211	porphyroclastic crd gneiss(no sill)	2.20	25.20	5.80
212	impure quartzite with weathered out kspar + bi	0.70	17.70	5.50
213	musc+bi schist (edge of shear zone)	1.50	22.80	6.50
223	retrogressed musc pelite gneiss	5.40	35.00	6.80
224	pelitic gneiss +kspar clasts (quite magnetic)	5.50	182.50	23.10
225	retrogressed migmatitic pelite	2.50	23.80	6.50
226	musc+bi schist	2.10	27.50	7.70
228	crd-sill migmatite gneiss	2.80	36.80	8.70
230	crd-sill migmatite gneiss	2.50	27.90	8.90
231	crd-sill migmatite gneiss	2.30	31.00	14.20
232	psammite qtz rich crd bearing	1.70	33.70	15.40
240	sill-cordierite pelite	3.00	35.30	6.20
241	sill-cordierite pelite	3.60	35.30	5.90
242	sill-cordierite-garnet pelite	3.00	32.20	6.80
243	sill-cordierite-garnet pelite	3.60	26.40	7.00
244	sill-cordierite-garnet pelite	3.00	33.70	8.40
245	sill-cordierite-garnet pelite	2.10	22.20	5.40
246	sill leucogneiss with crd +/- gt segs	4.60	14.00	7.80
247	sill leucogneiss with crd +/- gt segs	4.90	26.70	18.60
248	sill leucogneiss with crd +/- gt segs	4.60	23.20	9.40
249	sill leucogneiss with crd +/- gt segs	4.50	22.30	14.20
250	sill leucogneiss with crd +/- gt segs	5.30	29.20	15.50
267	sill-cordierite pelite	4.10	34.10	8.80
268	sill-cordierite pelite	3.40	32.20	6.60
269	sill-cordierite pelite	3.40	31.70	5.80
321	pssammitic diatexite	4.30	92.30	13.00
325	felsic diatexite	2.30	12.80	7.70
326	pssammatic gneiss	1.80	47.70	11.60
327	pssammatic gneiss	3.00	16.60	11.10
319	pssammitic migmatite	4.20	38.50	8.70
328	sillimanite leucogneiss	3.60	21.00	8.30
329	sillimanite leucogneiss	3.80	23.80	9.20
330	sillimanite leucogneiss	1.70	35.90	14.00
331	sillimanite leucogneiss	0.90	41.80	10.80
332	sillimanite leucogneiss	1.00	36.50	10.90
333	sillimanite leucogneiss	1.20	40.10	10.50
334	sill-bi bearing felsic gneiss	3.60	19.50	6.00
335	sill-bi bearing felsic gneiss	2.80	28.90	13.20
336	sill-bi bearing felsic gneiss	3.20	19.90	8.40
337	sill-bi bearing felsic gneiss	3.90	21.00	9.20
338	sill-bearing pssammitic gneiss	2.00	25.70	5.70
339	sill-bearing pssammitic gneiss	2.00	25.80	4.00
340	sill pssammitic diatextite	2.80	30.70	7.90
341	sill pssammitic diatextite	3.30	21.60	7.30
342	luecogneiss	1.70	19.00	4.00
343	sill-bearing felsic gneiss	2.50	24.60	8.00
429	psammite	1.52	26.64	4.57
430	calc-silicate	0.06	6.28	4.35
431	calc-silicate	0.18	5.33	1.67

432	metapelite (gt-bearing)	1.12	19.10	2.24
438	mu-qz mylonite	4.12	21.96	5.16
442	qz-fsp +/- tourmaline pool	3.76	55.71	6.97
444	qz-amphibole gneiss	0.40	14.74	3.71
445	leucogneiss/pegmatite	1.34	6.13	1.74
446	high-strain leucogneiss	0.82	31.56	3.95
447	leucogneiss	0.93	38.69	4.14
448	qz-tourmaline pod in qz-pl pegmatite	0.91	30.79	3.53
449	migmatitic psammite	1.18	38.34	5.07
450	bi-ksp-qz +/- cd leucosome	2.66	46.81	4.50
453	leucogneiss	1.88	26.70	9.13
454	leucogneiss	2.85	21.48	5.34
455	Crd-sill bedded pelite	2.50	27.93	4.07
456	Crd-sill bedded pelite(slightly more psammitic)	2.97	29.89	5.17
457	Pegmatite- bi+qtz+plag	4.36	34.84	4.48
458	Crd-sill bedded pelite	2.13	26.11	4.72
459	crd rich rock+sill+spinel+kspar	0.94	22.41	3.75
460	sill leucogneiss	1.54	23.14	3.11
461	sill leucogneiss	0.95	11.33	5.03
462	sill leucogneiss	1.33	13.39	5.35
463	sill leucogneiss	1.54	20.20	6.50
464	crd-sill rich pelite	4.54	42.14	9.64
465	crd-sill rich pelite	3.14	27.54	6.30
466	crd-sill rich pelite	2.71	25.90	4.13
467	crd-sill rich pelite (on the margin of shear zone)	1.73	23.04	4.58
468	crd-sill rich pelite (outside shear zone)	3.06	29.71	5.66
469	crd-sill rich (outside shear zone)	2.33	24.21	3.85
470	musc+bi schist (shear zone)	2.55	25.91	6.76
471	musc+bi schist (shear zone)	2.99	26.68	4.08
472	musc+bi schist (shear zone)	2.81	40.07	4.68
473	crd-sill rich pelite	2.25	21.05	4.94
474	musc+bi schist (shear zone)	2.88	32.63	5.94
475	musc+bi schist (shear zone)	4.42	33.03	6.31
476	crd-sill bedded pelite	3.08	30.26	8.56
477	crd-sill bedded pelite (potentially more migmatisation and/or melt retention	2.25	33.17	8.54
478	crd-sill bedded pelite (migmatite- change in rocks from shear zone- more structurally altered)	3.80	27.43	4.04
479	crd-sill migmatised pelite	2.98	25.59	3.15
480	porphyroclastic crd gneiss(no sill)	1.84	22.08	3.36
481	impure quartzite with weathered out kspar + bi	0.47	15.12	3.23
482	musc+bi schist (edge of shear zone)	1.25	18.23	4.63
492	retrogressed musc pelite gneiss	4.81	23.26	5.70
493	pelitic gneiss +kspar clasts (quite magnetic)	5.60	180.72	21.45
494	retrogressed migmatitic pelite	2.41	21.02	4.43
495	musc+bi schist	1.55	24.60	6.32
497	crd-sill migmatite gneiss	2.25	35.68	5.96
499	crd-sill migmatite gneiss	2.28	26.36	6.26
500	crd-sill migmatite gneiss	2.28	32.12	12.40
501	psammite qtz rich crd bearing	1.55	30.82	13.66
512	leucocratic gneiss with gt segregation +crd+qtz (blobs of gt & crd)	4.20	18.65	9.92
513	leucocratic gneiss with gt segregation +crd+qtz +a bit of biotite (blobs of gt & crd)	4.05	24.15	17.76

514	leucocratic gneiss with gt segregation +crd+qtz (blobs of gt & crd)	4.41	8.91	2.94
515	leucogneiss with large crd crystals in shear zone	3.95	36.07	6.14
516	leucogneiss with large crd crystals in shear zone	3.90	29.08	9.56
517	leucogneiss with large crd crystals in shear zone	3.66	23.76	8.82
526	leucogneiss	4.21	26.53	13.44
527	sill-crd leucogneiss with blobs	4.30	23.09	14.08
528	crd-sill metapelite (+kspar)	3.04	26.55	4.40
529	crd-sill metapelite (+kspar)	3.41	32.91	5.03
530	sill felsic gneiss	4.79	27.96	8.01
538	melt supported pelite (migmatitic)	3.70	102.35	14.26
539	quartzite	0.09	2.40	3.15
540	crd-sill pelite (migmatitic)	2.84	42.29	8.02
541	crd-sill pelite (migmatitic)	2.37	40.94	15.48
542	crd-sill pelite (migmatitic)	2.26	25.16	8.20
543	musc+bi schist +/- kyanite(?) too wet too id	2.71	38.18	6.35
544	poorly layered migmatite	2.33	25.27	7.24
547	bi, sill, qtz schist (crenulated)	0.89	16.24	4.03
548	sill leucogneiss (very sill rich)	1.14	23.26	9.83
549	crd-kspar-qtz-bi leucogneiss (perhaps sodic alkali feldspar)	2.02	24.64	5.75
550	crd-kspar-qtz-bi leucogneiss (perhaps sodic alkali feldspar)	0.72	20.73	2.43
551	sill-rich leucogneiss with plag(?)	0.63	15.78	2.99
552	sill+crd leucogneiss with blobs (as seen near boothby)	3.31	24.49	4.83
553	crd leucogneiss	0.83	25.39	6.03
554	sill+crd leucogneiss with blobs (as seen near boothby)	3.49	18.70	5.11
555	sill+crd leucogneiss with blobs (as seen near boothby)	3.77	15.30	6.35
556	crd+ksp+qtz+bi leucogneiss (no sill) - has a strong fabric but not a strong layering	2.17	16.66	4.22
557	crd-sill pelite	3.13	32.09	4.68
558	crd-sill pelite well layered	2.58	35.26	9.21
559	crd+qtz+kspar with very little bi - very fine grained - gneissic	2.32	46.39	9.05
565	psammite	2.58	27.64	5.56
580	crd rich migmatite	2.12	42.59	6.17
133	migmatised augen gneiss	3.90	42.70	15.10
134	migmatised augen gneiss	4.20	42.20	16.80
135	sill-bearing leucogneiss	2.80	33.80	7.80
136	migmatised augen gneiss	2.30	37.40	9.50
137	sill-bearing leucogneiss	1.10	24.20	4.60
138	migmatised augen gneiss	5.80	70.20	19.40
139	migmatised augen gneiss	4.30	66.60	18.40
140	migmatised augen gneiss	6.10	89.00	18.30
141	migmatised augen gneiss	5.10	71.20	15.80
142	migmatised augen gneiss	5.00	61.60	14.80
143	migmatised augen gneiss	4.40	62.40	22.30
144	migmatised augen gneiss	4.50	62.00	23.50
145	migmatised augen gneiss	3.50	67.60	19.70
146	sill-bearing leucogneiss	1.50	41.00	5.60
147	sill-bearing leucogneiss	1.90	40.80	10.10
148	sill-bearing leucogneiss	1.90	33.20	6.70
150	migmatised augen gneiss	4.50	58.70	8.30
151	migmatised augen gneiss	5.20	65.90	10.80
152	migmatised augen gneiss	4.20	69.00	11.00
153	migmatised augen gneiss	4.40	63.10	11.20

154	gt-sill augen gneiss	4.50	39.10	9.30
155	gt-sill augen gneiss	4.90	38.90	9.70
156	gt-sill augen gneiss	5.60	40.30	10.60
175	granitic gneiss east of pelite with Cs-Si	4.00	27.80	15.40
176	granitic gneiss east of pelite with Cs-Si	4.20	29.60	13.60
177	granitic gneiss east of pelite with Cs-Si	4.10	26.70	10.20
178	granitic gneiss east of pelite with Cs-Si	4.50	36.40	9.30
179	granitic gneiss east of pelite with Cs-Si	4.50	31.50	16.30
180	granitic gneiss east of pelite with Cs-Si	4.30	33.50	15.00
214	foliated migmatised granite	4.00	142.20	21.60
215	foliated migmatised granite	3.90	150.60	16.80
216	foliated migmatised granite	4.90	147.40	18.00
217	foliated migmatised granite	3.90	152.60	25.70
229	borderline dirty granite	2.80	38.70	12.00
233	granite(close to valley on SW side of Repeater Station	4.50	57.30	16.60
234	granite	5.40	48.00	13.60
227	dirty granite	1.90	27.50	6.00
251	augen granitic gneiss	4.00	32.80	9.70
252	augen granitic gneiss	4.60	40.30	8.80
253	augen granitic gneiss	4.80	44.80	8.20
255	augen granitic gneiss	4.80	37.40	12.60
256	augen granitic gneiss	5.10	57.50	4.90
272	augen granitic gneiss	5.00	78.80	16.60
273	augen granitic gneiss	6.10	96.60	19.00
274	augen granitic gneiss	6.10	57.90	10.50
280	augen granitic gneiss	1.70	50.00	2.30
281	augen granitic gneiss	4.60	50.60	13.40
282	augen granitic gneiss	5.30	36.80	23.70
283	augen granitic gneiss	4.70	54.50	14.20
284	augen granitic gneiss	4.80	58.30	18.60
285	augen granitic gneiss	4.90	59.30	25.10
286	augen granitic gneiss	4.80	44.20	10.30
287	augen granitic gneiss	4.50	53.50	22.10
288	augen granitic gneiss	4.50	56.10	17.60
289	augen granitic gneiss	4.70	60.70	24.20
290	augen granitic gneiss	4.40	58.30	16.30
291	augen granitic gneiss	4.40	53.20	12.60
292	augen granitic gneiss	4.50	57.40	15.00
293	augen granitic gneiss	4.70	57.50	21.30
294	augen granitic gneiss	4.40	56.20	19.40
295	augen granitic gneiss	5.00	61.50	25.50
296	augen granitic gneiss	4.40	56.40	20.00
297	augen granitic gneiss	4.90	59.70	20.50
298	augen granitic gneiss	4.70	61.80	20.80
299	augen granitic gneiss	4.60	59.90	15.50
300	augen granitic gneiss	4.70	71.20	20.40
301	augen granitic gneiss	5.10	61.60	32.00
302	augen granitic gneiss	4.40	58.00	19.60
303	augen granitic gneiss	4.50	57.20	21.00
304	augen granitic gneiss	4.70	60.50	16.70
305	augen granitic gneiss	4.70	59.60	24.60
306	augen granitic gneiss	4.70	62.80	20.50

307	augen granitic gneiss	4.20	59.80	20.90
308	augen granitic gneiss	4.50	60.40	19.80
309	augen granitic gneiss	4.20	56.70	21.60
310	augen granitic gneiss	4.60	61.30	21.30
311	augen granitic gneiss	4.50	68.20	21.40
312	augen granitic gneiss	4.70	56.40	23.00
313	augen granitic gneiss	4.00	51.10	15.70
314	augen granitic gneiss	4.20	51.90	16.00
315	augen granitic gneiss	4.30	52.80	25.60
316	augen granitic gneiss	4.70	55.50	19.90
317	late stage microgranite	3.40	105.50	23.20
318	late stage microgranite	4.00	104.50	28.60
320	late stage microgranite	2.80	85.60	16.20
322	augen granitic gneiss	2.30	74.40	16.80
323	diatextitic granitic gneiss	4.60	59.70	10.60
324	diatextitic granitic gneiss	3.80	63.10	9.20
344	fine-grained granitic gneiss	3.80	46.30	43.90
345	fine-grained granitic gneiss	2.90	59.60	21.20
346	fine-grained granitic gneiss	3.80	48.10	15.70
347	fine-grained granitic gneiss	4.60	53.30	34.20
348	augen granitic gneiss	4.30	50.50	13.90
349	augen granitic gneiss	4.70	47.70	33.70
350	augen granitic gneiss	4.30	57.20	17.40
351	augen granitic gneiss	4.60	61.20	13.90
352	augen granitic gneiss	4.50	57.50	14.80
353	augen granitic gneiss	5.40	78.80	13.50
427	high strain qz-fsp granite	3.35	26.76	8.15
428	high-strain qz-ksp-bi granite	3.17	22.21	7.19
433	gneissic granite	3.36	24.52	10.86
434	gneissic granite	3.64	22.61	7.85
435	gneissic granite	3.92	23.74	16.68
436	gneissic granite	3.62	22.51	8.88
437	mu-altered gneissic granite	3.91	29.57	10.19
439	augen gneiss	6.27	37.76	7.66
440	augen gneiss	4.42	37.83	7.03
441	augen gneiss	3.99	61.92	9.89
443	granite gneiss (borderline augen gneiss)	5.31	82.40	11.43
483	foliated migmatised granite	4.13	146.41	16.56
484	foliated migmatised granite	4.20	140.62	15.10
485	foliated migmatised granite	4.08	140.45	14.24
486	foliated migmatised granite	4.63	156.78	21.92
496	dirty granite	1.71	22.60	3.82
498	borderline dirty granite	2.55	44.60	11.62
502	granite(close to valley on SW side of Repeater Station	3.97	57.75	15.73
503	granite	4.56	42.78	11.30
518	augen gneiss (heterogeneous)	4.15	33.29	6.51
519	augen gneiss (heterogeneous)	4.00	29.10	9.34
520	augen gneiss (heterogeneous)	4.83	39.41	8.46
521	leucogneiss (in shear zone)	3.89	25.11	8.34
522	mylonite augen gneiss	4.59	38.54	9.41
523	augen gneiss (heterogeneous)	4.98	27.57	5.08
531	augen gneiss (heterogeneous)	4.49	38.72	8.17

535	augen gneiss (homogeneous)	4.42	58.78	13.13
536	augen gneiss (heterogeneous)	4.34	49.49	6.96
537	sheared augen gneiss	5.69	245.29	16.13
545	dirty granite with quartzite rafts	1.76	29.86	8.54
546	dirty granite (slightly less granite with melt rich pelite bands)	1.15	28.28	8.07
560	granitic gneiss	3.78	52.37	15.59
561	granitic gneiss	3.80	54.11	18.92
562	granitic gneiss	2.98	55.65	14.60
563	granitic gneiss	4.15	58.19	23.40
564	granitic gneiss	4.24	55.39	24.27
566	granitic gneiss	4.48	58.05	12.59
567	augen gneiss (heterogeneous)	4.85	70.78	20.38
568	augen gneiss (homogeneous)	5.17	77.59	22.75
569	augen gneiss (homogeneous)	6.00	24.46	7.08
570	augen gneiss (homogeneous)	4.49	56.62	19.03
571	augen gneiss (heterogeneous)	3.98	55.80	16.24
572	granitic gneiss	1.31	63.10	11.98
573	coarse grained pegmatite in augen gneiss	6.09	98.68	21.45
574	granitic gneiss	6.60	77.36	31.80
575	granitic gneiss	2.76	70.19	16.17
576	augen gneiss (heterogeneous)	4.14	66.00	18.46
577	augen gneiss (homogeneous)	5.33	75.24	21.04
578	sheared augen gneiss	4.64	65.92	20.46
579	biotite bearing pegmatite	2.43	227.06	20.68
581	augen gneiss (heterogeneous)	4.43	57.99	10.72
582	pegmatite in shear zone next to augen gneiss	4.47	444.46	31.73
583	ultra mylonitic augen gneiss	4.81	206.27	15.67
584	mylonitic augen gneiss	5.22	276.46	14.63
585	slightly sheared augen gneiss (heterogenous)	4.90	69.47	17.71
586	augen gneiss (heterogeneous)- slightly sheared	5.10	79.03	26.66
587	augen gneiss (heterogeneous)	4.12	63.43	9.89
588	augen gneiss (heterogeneous)	4.51	60.25	10.09
236	felsic component of mafic-felsic gneiss	2.20	7.30	3.10
237	felsic component of mafic-felsic gneiss	4.00	27.90	15.50
238	felsic gneiss	4.50	26.40	15.90
239	felsic gneiss	5.80	31.10	16.60
275	felsic gneiss	2.10	29.20	6.70
277	composite felsic/mafic gneiss	4.10	20.50	3.60
278	composite felsic/mafic gneiss	2.90	9.40	2.70
279	composite felsic/mafic gneiss	4.10	8.40	2.10
254	felsic gneiss	5.00	26.30	8.50
257	felsic component of mafic-felsic gneiss	3.70	68.80	24.00
258	felsic gneiss +/- crd segs	4.30	25.50	17.10
259	felsic gneiss +/- crd segs	5.20	29.10	24.40
260	felsic gneiss +/- crd segs	4.90	26.00	18.70
262	felsic gneiss +/- crd segs	4.70	22.60	26.00
263	felsic gneiss +/- crd segs	4.50	28.60	18.10
264	felsic gneiss +/- crd segs	4.80	27.10	12.40
265	felsic gneiss +/- crd segs	5.20	24.70	20.40
266	felsic gneiss +/- crd segs	3.90	20.30	11.60
270	felsic gneiss +/- crd segs	3.80	28.90	20.00
271	felsic gneiss	4.20	27.30	11.30

357	composite felsic/mafic gneiss	3.40	18.90	3.40
358	composite felsic/mafic gneiss	3.80	12.10	2.60
359	composite felsic/mafic gneiss	1.80	8.50	2.50
360	composite felsic/mafic gneiss	2.10	8.20	2.60
361	composite felsic/mafic gneiss	2.10	13.10	4.20
354	composite felsic/mafic gneiss	3.00	6.80	2.80
355	composite felsic/mafic gneiss	1.60	4.40	2.50
356	composite felsic/mafic gneiss	2.20	4.50	2.70
524	black & white stripey gneiss	2.14	28.80	3.58
525	black & white stripey gneiss	3.45	64.32	19.11
532	black & white stripey gneiss	1.71	9.06	1.26
533	black & white stripey gneiss	1.56	3.78	1.06
534	black & white stripey gneiss (more felsic layers)	4.72	10.95	1.86